













Statens vegvesen

Ferry free E39 –Fjord crossings Bjørnafjorden

304624

Rev.	Publish date	Description	Made by	Checked by	Project appro.	Client appro.
0	15.08.2019	Final issue	MST	RML	SEJ	
Client						
 Statens vegvesen						
Contractor			Contract no.:			
        			18/91094			

Document name:

Preferred solution, K12 – Appendix F
Global analyses – Modelling and assumptions

Document no.:

SBJ-33-C5-AMC-90-RE-106

Rev.:

0

Pages:

114

CONCEPT DEVELOPMENT, FLOATING BRIDGE E39 BJØRNAFJORDEN

Preferred solution, K12

Appendix F – Global analyses - Modelling and assumptions

CLIENT

Statens vegvesen

DATE: / REVISION: 15.08.2019 / 0

DOCUMENT CODE: SBJ-33-C5-AMC-90-RE-106



 **AAS-JAKOBSEN**  **COWI**  **Multiconsult**



 **Aker Solutions**

 entail

 NGI

 **DISSING+WEITLING**
architecture a|s

 **mossmaritime**

REPORT

PROJECT	Concept development, floating bridge E39 Bjørnafjorden	DOCUMENT CODE	SBJ-33-C5-AMC-90-RE-106
SUBJECT	Appendix F – Global analyses - Modelling and assumptions – K12	ACCESSIBILITY	Restricted
CLIENT	Statens vegvesen	PROJECT MANAGER	Svein Erik Jakobsen
CONTACT	Øyvind Kongsvik Nedrebø	PREPARED BY	Martin Storheim
		RESPONSIBLE UNIT	AMC

SUMMARY

This report describes modelling and assumptions for the global models established in the concept development work of a floating bridge over Bjørnafjorden. Cable stay tension is evaluated. A benchmark between key softwares for global simulation is shown. Sensitivity to key assumptions and input parameters are checked.

REV.	DATE	DESCRIPTION	PREPARED BY	CHECKED BY	APPROVED BY
0	15.08.2019	Final issue	M. Storheim	R. M. Larsen	S. E. Jakobsen

TABLE OF CONTENTS

1	Introduction.....	6
2	Modelling and assumptions	7
2.1	Overall description of bridge concept.....	7
2.2	Overall description of modelling approach.....	10
2.2.1	Road alignment.....	10
2.2.2	Parametric input file	11
2.2.3	Model generation	11
2.3	Coordinate systems	12
2.4	Static model – RM-Bridge	14
2.5	Dynamic model – Orcaflex.....	17
2.5.1	General	17
2.5.2	Bridge girder	17
2.5.3	Pontoons.....	17
2.5.4	Tower.....	18
2.5.5	Cable stays.....	19
2.5.6	Columns	19
2.5.7	Mooring lines	19
2.5.8	Summary of methodology for wind and wave analysis	20
2.5.9	Static equilibrium of pontoons and the cable-stayed bridge	21
2.6	Dynamic model – Novaframe	21
2.6.1	General model	21
2.6.2	Numbering system	21
2.6.3	Modelling of pontoons.....	21
2.6.4	Damping.....	23
2.6.5	Model geometry	23
2.6.6	Wind loading.....	24
2.7	Dynamic model – LS-DYNA	25
3	Tensioning of cable-stayed bridge.....	26
4	Pontoon design.....	30
4.1	Mass estimates	30
4.2	Pontoon geometry	30
4.3	Pontoon hydrodynamics.....	32
4.3.1	Added mass.....	32
4.3.2	Potential flow damping.....	33
4.3.3	Wave excitation forces	34
4.3.4	Force divided by damping.....	35
4.4	Viscous damping	36
5	Description of the aerodynamic buffeting analysis.....	38
5.1.1	Wind field simulation.....	38
5.1.2	Linear quasi-static wind theory.....	38
5.1.3	Comparison between linear and nonlinear buffeting response	40
5.1.4	Wind load simulation	41
6	Global damping and modal analysis	42
6.1	Decay tests.....	42
6.2	Modal analysis	44
6.2.1	Modal analysis: solving the frequency-dependent eigenvalue problem	44
6.2.2	Modal analysis of the Bjørnafjord Bridge concept K12	46
7	Benchmark between softwares.....	50
7.1	Eigenmodes	50
7.2	Comparison of static response	52
7.2.1	Permanent loads.....	53
7.2.2	Transverse load	56
7.2.3	Torsional load	58
7.2.4	Temperature load	60
7.3	Comparison of wind response	62
7.3.1	Input parameters	62
7.3.2	Static wind response.....	63

7.3.3	Dynamic wind results.....	66
7.3.4	Discussion	67
8	Numerical modelling aspects	68
8.1	Method	68
8.2	Conclusion	68
8.3	Time duration	69
8.3.1	Axial force	70
8.3.2	Weak axis bending moment	71
8.3.3	Strong axis bending moment	73
8.3.4	Torsional moment.....	74
8.4	Ramping.....	76
8.5	Time step	80
8.6	Wave spectrum discretization	81
8.6.1	Conclusion.....	81
8.6.2	Analysis	81
8.7	Wave direction discretization	85
8.8	Seed variability.....	87
8.9	Number of wave components in frequency domain analysis	89
8.10	Frequency vs time domain analysis	91
9	References.....	94
10	Enclosures	95

1 Introduction

This report describes modelling and assumptions for the global models established in the concept development work of a floating bridge over Bjørnafjorden.

Four different simulation softwares have been used for global response assessments during design development with various strengths and weaknesses:

- RM-Bridge for permanent and traffic loads
- Orcaflex for wave loading in frequency and time domain, and wind loading in time domain
- Novaframe for dynamic wind response in frequency domain and for generation of input to modal analysis and dynamic instability assessments
- LS-DYNA for local and global ship collision simulations

In addition, a range of softwares were utilized for input generation and special studies, such as Wamit, Wasim, Rhino and Windsim. A full list of the different softwares used and their respective versions are given in [1].

A common modelling approach was needed to coordinate the different global models during the rapid design development process, and the selected approach is described herein. Benchmark studies were then utilized to verify the model behavior in the different softwares to ensure consistent results.

In the initial round four concepts were evaluated:

- K11 : End-anchored arch-type floating bridge
- K12 : End-anchored arch-type floating bridge with side moorings
- K13 : Straight floating bridge with side moorings
- K14 : Curved floating bridge with side moorings

K12 was selected as the preferred concept and is the focus of this report. For details on modelling and assumptions regarding the other concepts, see [2].

For details regarding concept development and design considerations, see [3].

2 Modelling and assumptions

2.1 Overall description of bridge concept

The K12 bridge concept features an arch-type bridge with three mooring clusters. Mooring lines contributes to resistance against transverse loads, increase the buckling capacity and provides damping for various excitation modes. The latest iteration number for the concept was 7, and the iteration was termed K12_07.

The Southern end of the bridge starts with a straight cable-stayed bridge. A free span of about 380 m yields a navigational channel width of more than 250 m. The bridge girder is supported into the tower in vertical and sideways direction. Back span columns are rigidly connected to the bridge girder. Towards the Northern end the bridge girder strength is gradually increased in the last 40 m towards the abutment. The bridge girder is fixed to ground at both abutments. See Appendix L [4] for more details on the cable-stayed bridge and abutments.

A *circtangular* shape of the pontoon was selected, with a pontoon spacing of 125 m. A draught of 5 meters is defined for pontoons without mooring lines, and an additional draught of 2.5 m is required to support the vertical load component of moorings (line weight and pretension). Full mooring lines were included in the simulations, in which the various segments of chain and wire were modelled explicitly. Soil stiffness was not accounted for in the global simulations. See section 4 for details. Mooring lines and anchor locations are shown in Appendix M [5].

Aerodynamic parameters are differentiated between the high-bridge and low-bridge coefficients. Aerodynamic parameters are defined in Appendix E [6], and the applied values assume the presence of a wind nose to improve the drag coefficient. Figure 2-1 shows the applied aerodynamic coefficients for the bridge girder. The transition between high and low bridge is defined as axis A12. Drag factors for cables are defined as 1.2 and 0.8 below and above 20 m/s wind. For simplicity a factor of 1.0 is used for all wind speeds; overestimating the extremes but underestimating the milder conditions. All columns between the bridge and the pontoon are modelled with a drag coefficient of 1.5. Aerodynamic loads on the pontoons is simplified to use the same drag and lift coefficients as for viscous drag and the relevant exposed area and air density, but with a mean wind load and direction only. Aerodynamic damping is included by using buffeting theory with relative wind velocities for all elements except the pontoon.

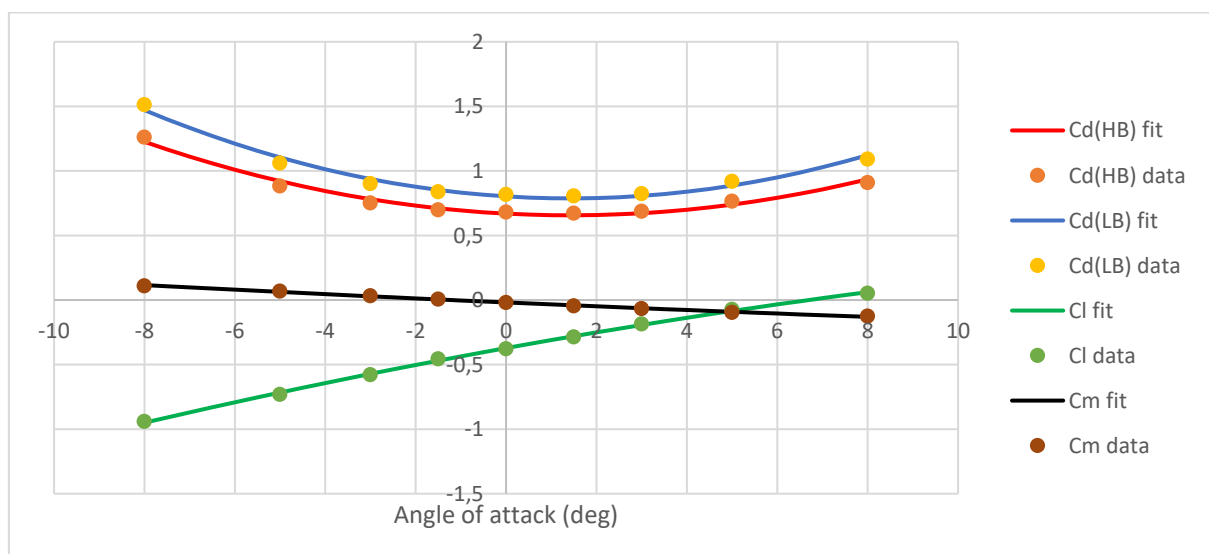


Figure 2-1 Aerodynamic coefficients for bridge girder as applied in the simulations for high bridge (HB) and low-bridge (LB) respectively.

Figure 2-2 shows the bridge geometry. The mooring clusters were placed in pontoons A13, A20 and A27, and the combined effect of the moorings is to provide sufficient stiffness and damping to the relevant deformational modes. The mooring cluster stiffness varies somewhat between each cluster as a line pretension was targeted rather than a specific mooring cluster stiffness. Full documentation of the mooring system can be found in [5].

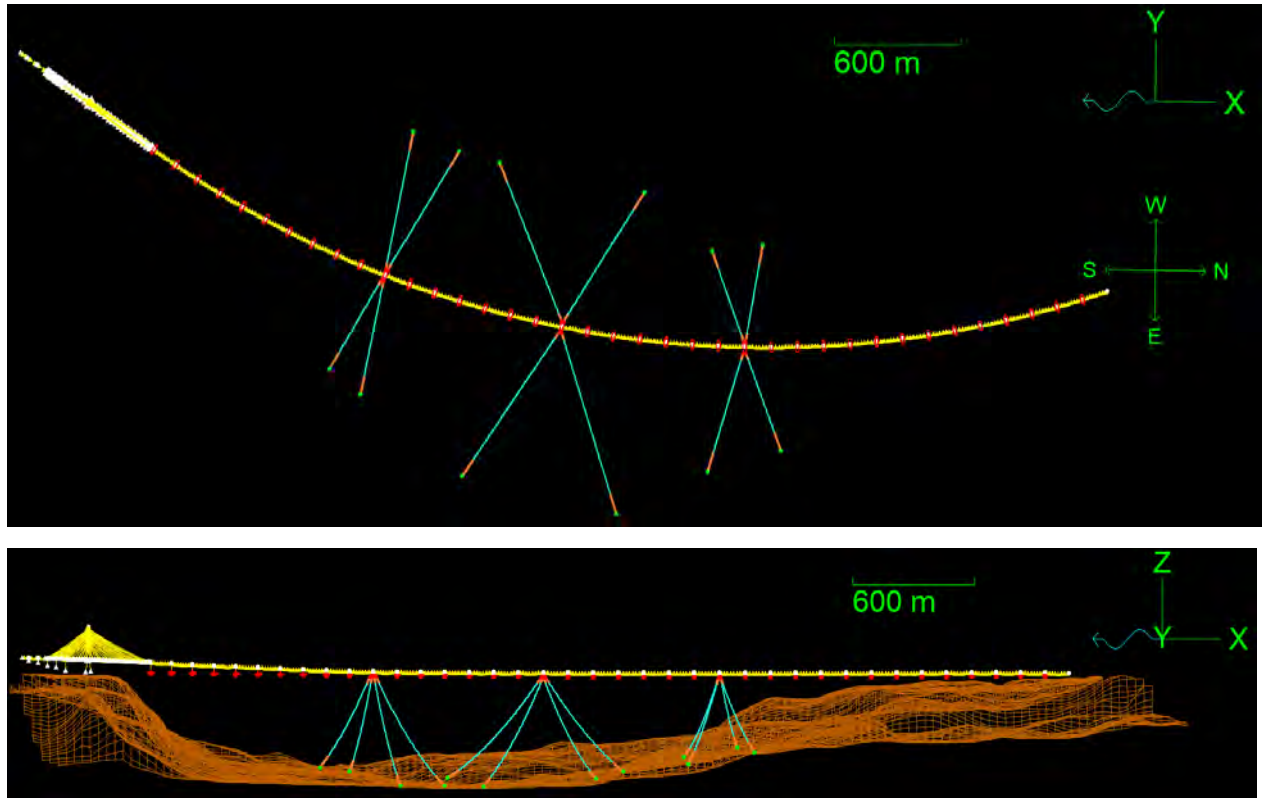


Figure 2-2 Plan and side view of bridge concept K12_07.

Figure 2-3 shows the discretization of cross-sectional property types along the bridge girder and Table 2-1 lists the key properties for each property type, where

M – Unit mass pr. meter

I_y – Second area moment about weak axis

I_z – Second area moment about strong axis

J – Torsional constant

A_x – Cross-sectional area

L_y – Width of segment in transverse direction

L_z – Height of segment

VCGt – Distance from top of segment to center of gravity.

The values for weak-axis moment in Table 2-1 are corrected for shear lag in a serviceability limit state, see Enclosure 1 and [7] for more info. The listed unit mass includes structural mass + five ton/m added mass that accounts for asphalt and railings. For the steel girder a constant structural mass of 14 ton/m is considered. The actual mass varies somewhat along the girder, see Appendix K for details.

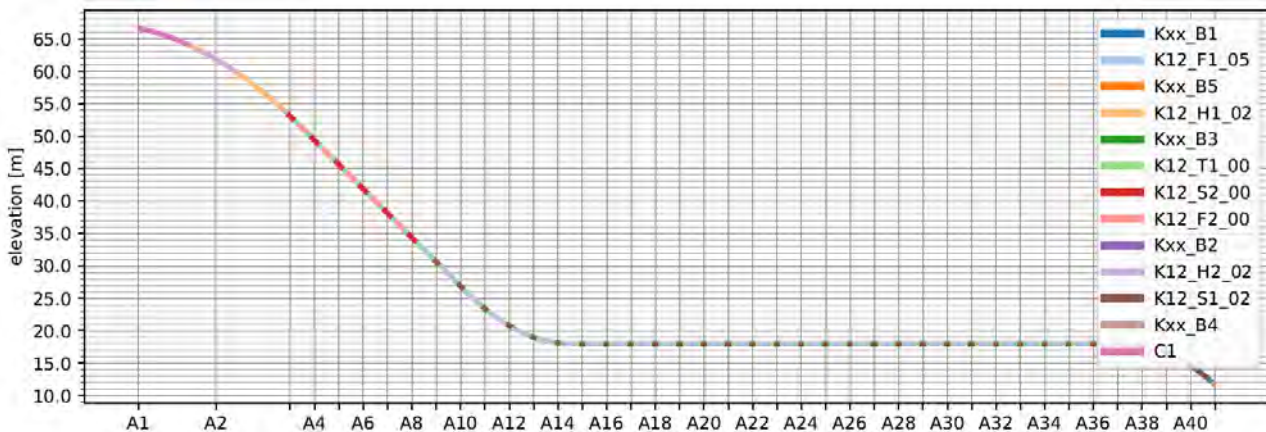


Figure 2-3 Sectional property definition for K12_07.

Table 2-1 Key sectional properties for K12_07.

	M	ly	lz	J	Ax	Ly	Lz	VCGt
	[tonne/m]	[m^4]	[m^4]	[m^4]	[m^2]	[m]	[m]	[m]
K12_S1_02	19	3.668	110.4	11.349	1.779	27	4	1.989
K12_S2_00	19	3.785	121.83	12.01	1.8829	27	4	2.041
K12_T1_00	19	3.311	98.583	10.105	1.521	27	4	1.878
K12_F2_00	19	2.781	89.597	9.4228	1.331	27	4	1.763
K12_F1_05	19	2.569	84.698	8.6111	1.2699	27	4	1.682
K12_H1_02	19	2.534	89.531	6.629	1.297	27	3.5	1.463
K12_H2_02	19	3.64	123.34	9.663	1.797	27	3.5	1.633
C1	79.1	40.5	2138	135.4	27.951	29	3.5	1.463
Kxx_B1	19	5.32	170	18.2	2.09	27	4	1.989
Kxx_B2	20.52	5.95	226	20	2.28	27	4	1.989
Kxx_B3	25.16	7.7	314	24.3	2.86	27	4	1.989
Kxx_B4	29	9.74	423	28.5	3.34	27	4	1.989
Kxx_B5	30.12	10.06	461	29.7	3.48	27	4	1.989

More details on the concept development and choices are found in [3, 8].

2.2 Overall description of modelling approach

A common modelling approach was needed to coordinate the different global models during the rapid design development process. Hence, the model description was created independent of the different softwares and used as a common basis to establish models for each software. The detailed modeling approach varies somewhat due to varying methods and limitations in the individual softwares, but the common basis ensures consistent models and enables more rapid design iterations. Figure 2-4 illustrates the main methodology.

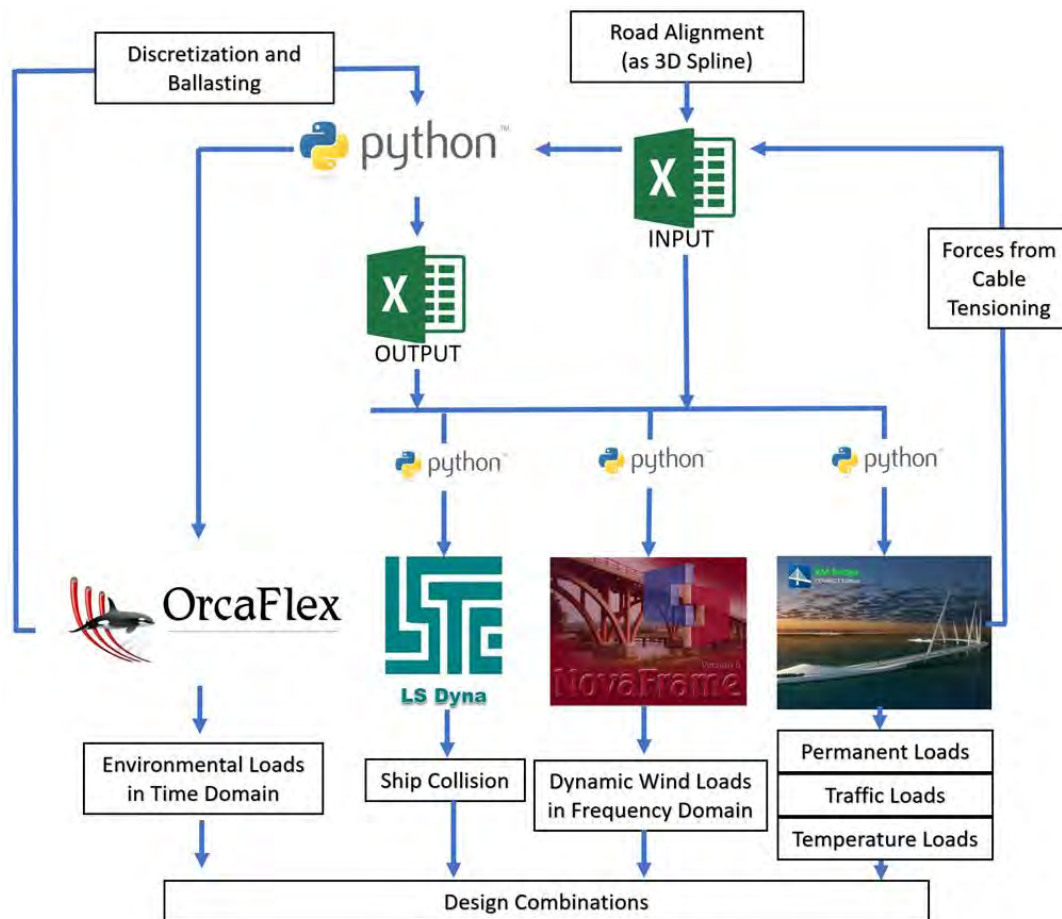


Figure 2-4 Illustration of information flow in the modelling and simulation system.

2.2.1 Road alignment

The road alignment is converted to a cubic 3D spline based on the original road coordinates. Coordinates and curvature of the road alignment are thus represented by the spline and can be obtained during model generation at all positions along the curve. For simplicity, the road line is assumed to be in the elastic neutral axis of the bridge girder, resulting in around 2m horizontal offset of the simulated bridge compared to the actual road line. The practical consequence of this assumption is negligible, but it should be improved for detailed design.

The road alignment 16851 (rev. 03) (ref. [9]) was used for the K12_07 concept.

2.2.2 Parametric input file

An excel file is used to input all relevant information on how the bridge model should be generated from the road alignment, including:

- Axis position
- Bridge girder (boundary conditions, segmentation and section properties)
- Columns (boundary conditions, segmentation and section properties)
- pontoons (position, orientation and pontoon type)
- Mooring system
- Tower (segmentation and section properties)
- Stay cables (position, stiffness and tension)

The parametric description simplifies the model generation as the manual modelling time consumption is decreased substantially. See Enclosure 1 for the parametric input files for the K12_07 concept.

2.2.3 Model generation

The OrcaFlex model is automatically generated based on the input file. During the OrcaFlex model generation, all relevant input to the other software packages are exported to an excel output file, including:

- Bridge
 - Arclength and profile number
 - Nodes and elements
 - Section properties
- Tower
 - Nodes and elements
 - Section properties
- Columns
- Cables
- pontoons
- Mooring

Section parameters are given in the unit per meter in the bridge's longitudinal direction as Mass, Inertia about XYZ, 2. area moments XYZ, Torsion constant, Cross-sectional area, Shear areas, width and height, center of gravity, Youngs modulus, Rayleigh damping ratio, Rayleigh damping lower period, Rayleigh damping upper period, Drag coefficient, Lift coefficient, Moment coefficient, Wind angle uncertainty

Pontoon parameters are given as Mass, Inertia about X, Inertia about Y, Inertia about Z, Buoyancy, Vertical center of buoyancy and gravity, ballast amount and center of gravity, 2. area moment about X, Inertia about Y, Freeboard

Each stay cable is connected to the tower in one end and the bridge deck in the other. The offsets for the connection point relative to the center of the bridge and tower is defined for the nodes. Element parameters are defined for each element. For the cable elements the effective Youngs modulus is given based on Ernst’s formula (below) for use in the softwares that don’t include cable sag in the element formulation and discretization.

$$E_{\text{eff}} = E_0 \frac{1}{1 + \frac{\gamma^2 L_h^2 E_0}{12 \sigma^3}} \tag{2.6}$$

where:

E_{eff} = the effective elastic modulus in [N/mm²]

E_0 = the elastic modulus of the stay cable material in the absence of the sag effect [N/mm²]

γ = the specific weight of the stay cable material in [N/mm³]

L_h = the projected stay cable length in plan in [mm]

σ = the axial stress of the cable in [N/mm²]

2.3 Coordinate systems

The various softwares have different definitions of the local and global coordinate system. The following figures outline the different systems. As far as practical, a common bridge coordinate system was used as an interface between the systems.

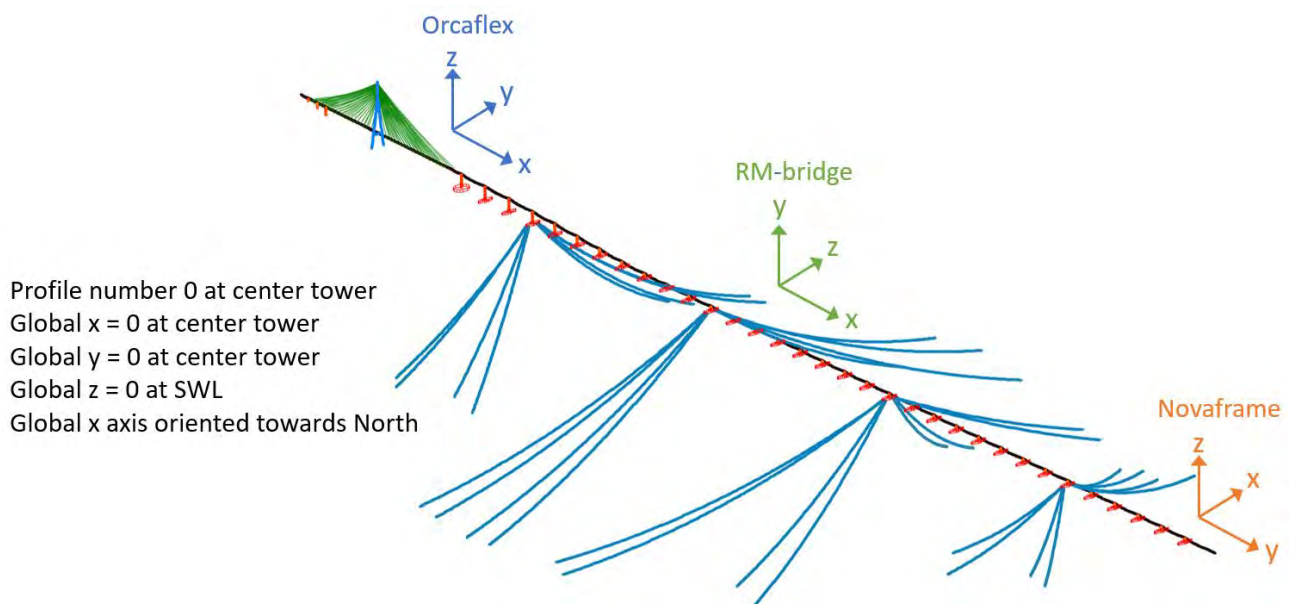


Figure 2-5 Global bridge coordinate system

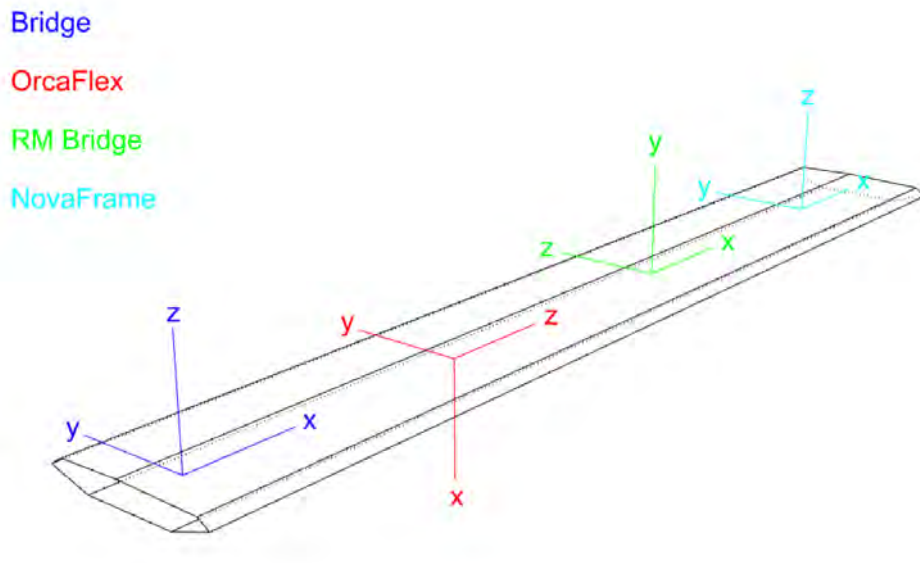


Figure 2-6 Local coordinate system bridge girder

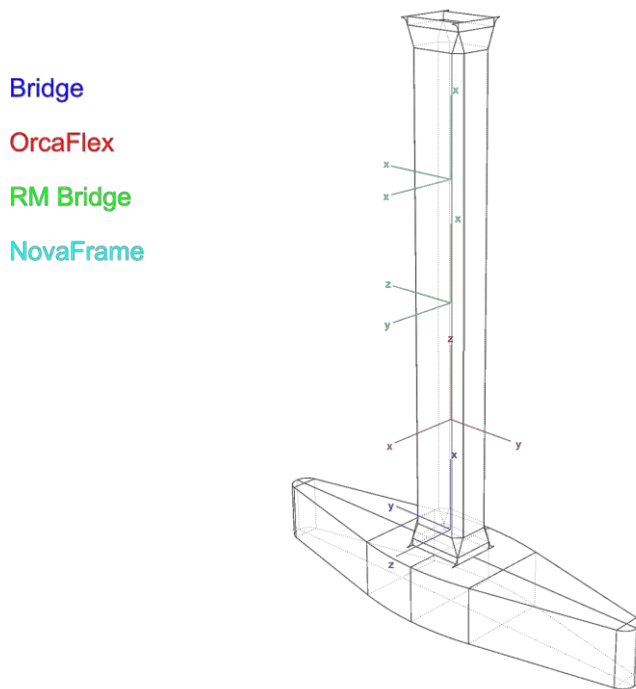


Figure 2-7 Local coordinate system columns (and tower)

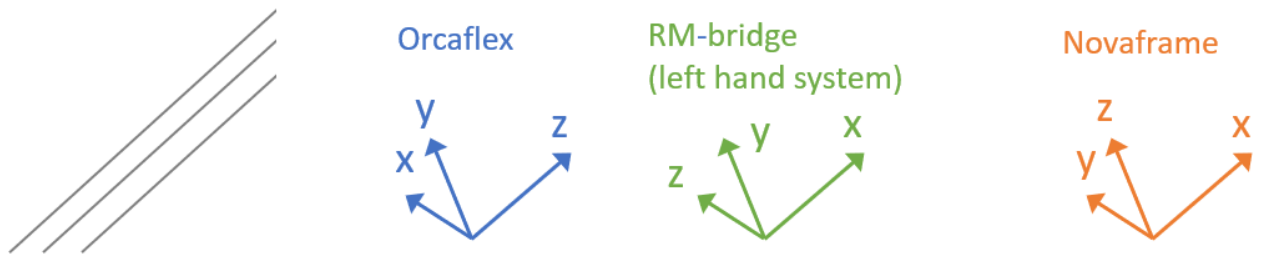


Figure 2-8 Local coordinate system stay cables

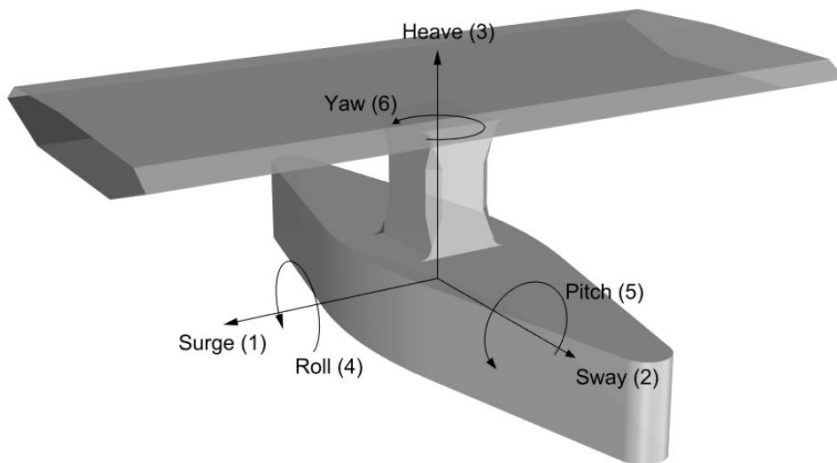


Figure 2-9 Local coordinate system pontoons

2.4 Static model – RM-Bridge

Two types of models were developed in RM-bridge during the project phase; a simplified model for calculation of static loads from permanent loads, temperature and traffic and a more comprehensive nonlinear model suitable for dynamic simulations with larger deformations. The former was used for the main global analyses and is described herein, the latter was used as a verification model for the global dynamic analyses and is described separately in Appendix U [10].

The RM Bridge model is established by a Python script reading the model data from the Excel files described in section 2.2.2 to TCL text files formatted to read by the RM Bridge software. All beam and cable properties as well as the permanent loads are transferred to the RM Bridge model by the Python script. Benchmarks have been performed and documented in section 7.

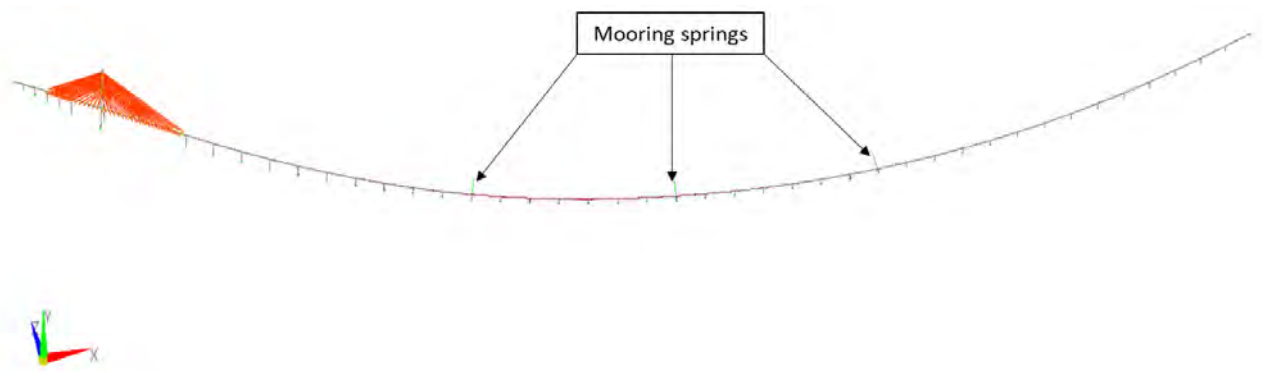


Figure 2-10 Structural model K12_07

Table 2-2 Element numbering of beam, cable and spring elements.

	Beam elements			Spring elements	
	Start Elem	End Elem	Step	Support	
Bridge girder					
- High bridge	101	192	1	13100	(Abutment, start)
- (Concrete)	101	138	1		
- (Steel)	139	192	1		
- Floating bridge	251	858	1	13200	(Abutment, end)
Pier, viaduct					
- Pier A1-A	2101	2104	1	12100	(Foundation - Pier A1-A)
- Pier A1-B	2201	2204	1	12200	(Foundation - Pier A1-B)
- Pier A1-C	2301	2304	1	12300	(Foundation - Pier A1-C)
- Pier A1-D	2401	2404	1	12400	(Foundation - Pier A1-D)
- Pier A1-E	2501	2504	1	12500	(Foundation - Pier A1-E)
Pier, floating bridge					
- Pier A3	4031	4034	1		
- Pier A4	4041	4044	1		
- Pier A5	4051	4054	1		
- Pier A6	4061	4064	1		
- Pier A7	4071	4074	1		
- Pier A8	4081	4084	1		
- Pier A9	4091	4094	1		
- Pier A10	4101	4102	1		
- Pier A11	4111	4112	1		
- Pier A12	4121	4122	1		
- Pier A13	4131	4132	1		
- Pier A14	4141	4142	1		
- Pier A15	4151	4152	1		
- Pier A16	4161	4162	1		
- Pier A17	4171	4172	1		
- Pier A18	4181	4182	1		
- Pier A19	4191	4192	1		
- Pier A20	4201	4202	1		
- Pier A21	4211	4212	1		
- Pier A22	4221	4222	1		
- Pier A23	4231	4232	1		
- Pier A24	4241	4242	1		
- Pier A25	4251	4252	1		
- Pier A26	4261	4262	1		
- Pier A27	4271	4272	1		
- Pier A28	4281	4282	1		
- Pier A29	4291	4292	1		
- Pier A30	4301	4302	1		
- Pier A31	4311	4312	1		
- Pier A32	4321	4322	1		
- Pier A33	4331	4332	1		
- Pier A34	4341	4342	1		
- Pier A35	4351	4352	1		
- Pier A36	4361	4362	1		
- Pier A37	4371	4372	1		
- Pier A38	4381	4382	1		
- Pier A39	4391	4392	1		
- Pier A40	4401	4402	1		

	Beam elements			Spring elements		
	Start Elem	End Elem	Step	Support		
Pontoon, floating bridge				Vertical	Roll	Water plane
- Pontoon A3	5031	5034	1	50103	50203	30030
- Pontoon A4	5041	5044	1	50104	50204	30040
- Pontoon A5	5051	5054	1	50105	50205	30050
- Pontoon A6	5061	5064	1	50106	50206	30060
- Pontoon A7	5071	5074	1	50107	50207	30070
- Pontoon A8	5081	5084	1	50108	50208	30080
- Pontoon A9	5091	5094	1	50109	50209	30090
- Pontoon A10	5101	5104	1	50110	50210	30100
- Pontoon A11	5111	5114	1	50111	50211	30110
- Pontoon A12	5121	5124	1	50112	50212	30120
- Pontoon A13	5131	5134	1	50113	50213	30130
- Pontoon A14	5141	5144	1	50114	50214	30140
- Pontoon A15	5151	5154	1	50115	50215	30150
- Pontoon A16	5161	5164	1	50116	50216	30160
- Pontoon A17	5171	5174	1	50117	50217	30170
- Pontoon A18	5181	5184	1	50118	50218	30180
- Pontoon A19	5191	5194	1	50119	50219	30190
- Pontoon A20	5201	5204	1	50120	50220	30200
- Pontoon A21	5211	5214	1	50121	50221	30210
- Pontoon A22	5221	5224	1	50122	50222	30220
- Pontoon A23	5231	5234	1	50123	50223	30230
- Pontoon A24	5241	5244	1	50124	50224	30240
- Pontoon A25	5251	5254	1	50125	50225	30250
- Pontoon A26	5261	5264	1	50126	50226	30260
- Pontoon A27	5271	5274	1	50127	50227	30270
- Pontoon A28	5281	5284	1	50128	50228	30280
- Pontoon A29	5291	5294	1	50129	50229	30290
- Pontoon A30	5301	5304	1	50130	50230	30300
- Pontoon A31	5311	5314	1	50131	50231	30310
- Pontoon A32	5321	5324	1	50132	50232	30320
- Pontoon A33	5331	5334	1	50133	50233	30330
- Pontoon A34	5341	5344	1	50134	50234	30340
- Pontoon A35	5351	5354	1	50135	50235	30350
- Pontoon A36	5361	5364	1	50136	50236	30360
- Pontoon A37	5371	5374	1	50137	50237	30370
- Pontoon A38	5381	5384	1	50138	50238	30380
- Pontoon A39	5391	5394	1	50139	50239	30390
- Pontoon A40	5401	5404	1	50140	50240	30400
Pylon, A2						
- Lower Leg, right	3101	3108	1	32010	(Foundation, right pylon leg)	
- Upper Leg, right	3110	3125	1	32020	(Foundation, left pylon leg)	
- Lower Leg, left	3201	3208	1	32011	(Right vertical support of MG on Pylon)	
- Upper Leg, Left	3210	3225	1	32012	(Left vertical support of MG on Pylon)	
- Spire	3301	3308	1	32111	(Horizontal support of MG on Pylon)	
- Cross-beam	3401	3402	1			
Stay Cables						
- Back span, right	21011	21181	10			
- Back span, left	22011	22181	10			
- Main span, right	23011	23181	10			
- Main span, left	24011	24181	10			
Mooring cluster						
- Mooring cluster A13				40131		
- Mooring cluster A20				40201		
- Mooring cluster A27				40271		

Boundary conditions are extracted from the Excel files shown in Figure 2.1 and assigned to the foundation springs and water plane springs shown in Table 2-2. The Roll water plane stiffness is modified by the GM effect. These conditions are valid for linear analyses only and is used for the variable static loads.

However, for permanent load the water plane springs are not active. These springs are substituted by the stiff vertical and roll spring shown in Table 2-2. This simplification is valid for ONLY the case of static permanent load.

The static permanent loads (not stay cable forces) are read as masses from the parametric input file and transformed to loads by $g=9.81\text{m/s}^2$. The stay cable tensioning force procedure is described in section 3.

2.5 Dynamic model – Orcaflex

The dynamic wind and wave analysis are performed with the time/frequency domain software OrcaFlex. Each part of the bridge model is shortly described in the following. The model is shown in Figure 2-2.

2.5.1 General

The dynamic simulation is performed with an implicit solver with time step 0.2 s as default. Dynamic environmental loads are ramped up during the first 300 seconds of the simulation to avoid impulses. Result data from the ramping stage is not extracted for post-processing. Sensitivity studies of the time step and duration of the ramp-up stage are included in section 8.

2.5.2 Bridge girder

The bridge girder is modelled using line objects. Each line object is divided into a finite number of elements. The number of elements should be large enough to capture all important modal shapes of the bridge girder. The line between two adjacent pontoons is modelled with 16 elements. The structural properties of the bridge girder are applied to the line objects. The structural mass (translation and rotation), stiffness (axial, bending and torsion), structural Rayleigh damping coefficient and aerodynamic load coefficients are given as input.

2.5.3 Pontoons

The pontoons are modelled using vessel objects. The properties of a vessel object are typically

- Mass matrix:
Given as input based on a weight estimate.
- Hydrodynamic data:
Wave excitation force, wave drift damping, added mass and damping are calculated in Wamit based on linear potential theory. The wave excitation forces are the wave loads on a fixed structure. Added mass and damping forces are the acceleration and velocity proportional forces on an oscillating body in still water. The wave drift forces depend on the first order motion of the body. In the present work the wave drift forces are calculated assuming fixed body, which is considered a conservative modelling choice, since all wave energy will be reflected by the body.
- Hydrostatics:
The buoyancy force is the weight of the displaced volume of the body. The hydrostatic (roll)

stiffness is a function of geometry and mass and is calculated as

$$C_{44} = \underbrace{\rho g \nabla z_b + \rho g I_{44}}_{\text{pontoon geometry}} - \underbrace{m_0 g z_{g,0}}_{\text{pontoon mass}} + \sum_{i=1}^N \underbrace{m_i g z_{g,i}}_{\text{connected masses}}$$

Only the contribution from pontoon geometry and pontoon mass shall be included in vessel hydrostatic stiffness as the connected masses will be included in OrcaFlex during static and dynamic calculation. The same applies for pitch stiffness. Heave stiffness is $C_{33} = \rho g A_w$, where A_w is the waterplane area.

- Wind and current coefficients:
Directional dependent wind and current coefficients contribute to static and low frequency loads.

The complete model will be ballasted by requiring zero vertical pontoon displacement in permanent condition. The ballast mass is connected to the pontoon objects.

2.5.4 Tower

The tower is modelled using line objects connected through constraint objects (essentially 6 DOF connection objects with possibility to fixate individual DOFs as desired). The line objects can capture axial force, bending moment and torque. The tower with lines and constraints are shown in Figure 2-11. The bearing between the tower and the bridge is modelled using constraint objects. The cable stays are connected to the relevant tower line objects at the correct height.

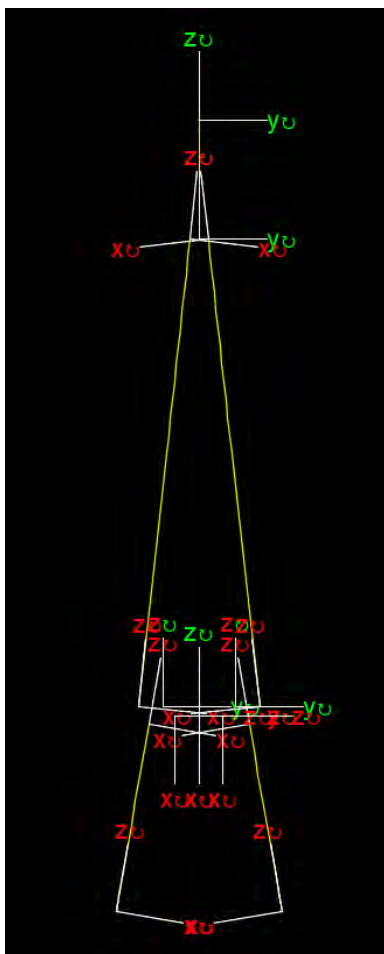


Figure 2-11 Illustration of tower model in orcaflex with bearings (green) and constraints (red)

2.5.5 Cable stays

The cable stay tensioning is performed in RM-Bridge using a form finding method (ref. section 3). The resulting cable tensions are used to decide the unstressed cable lengths in OrcaFlex as

$$L_0 = \frac{L}{1 + \frac{F}{EA}}$$

Where L is the system length, F is the cable tension and EA is the cable axial stiffness. The resulting cable tensions from RM-Bridge and OrcaFlex are plotted in Figure 2-12. The largest difference can be observed in the cables with bridge connection closest to the tower and arise because the elongation of the bridge girder in OrcaFlex is not corrected for the compression due to the cable-stay tension. The difference is not of importance for the overall bridge girder response.

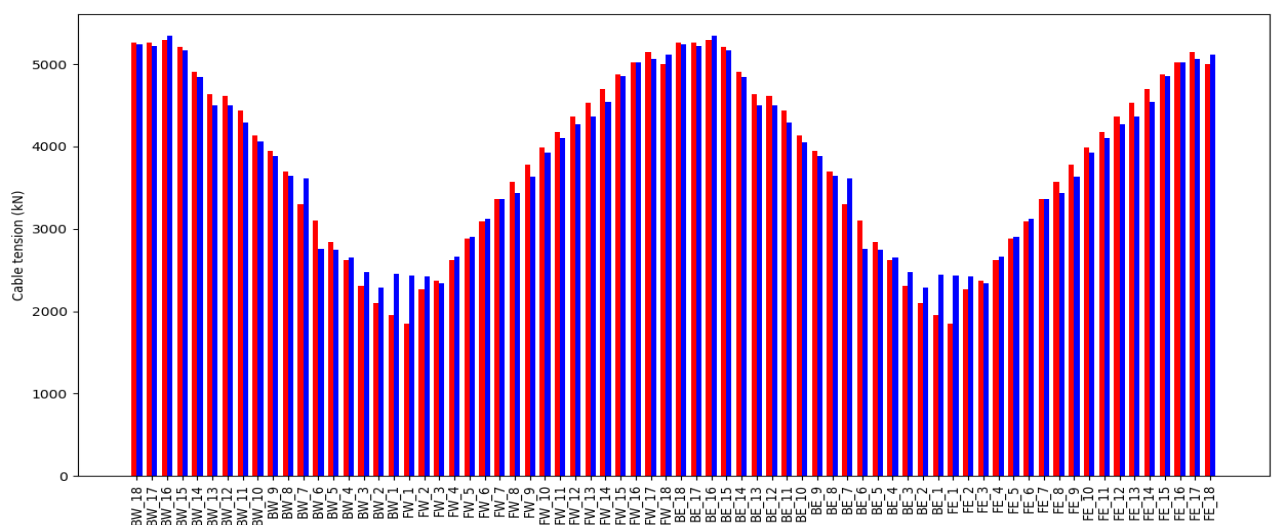


Figure 2-12 Cable tension, OrcaFlex (blue) and RM-Bridge (red)

2.5.6 Columns

The columns are modelled as line objects from the pontoons to the bridge girder. The columns in the back span of the cable stayed bridge are connected rigidly to the ground and to the bridge girder.

2.5.7 Mooring lines

Two methods of mooring line modelling were used in the current simulation work; a full mooring line system with FE-formulation of mooring lines and viscous damping and a simplified mooring system with a horizontal linear spring and a quadratic damping calibrated to match the full viscous mooring line damping. The latter is described in [11].

The full mooring system is modelled using line objects. The desired horizontal stiffness of the mooring system is obtained by adjusting the pretension level in each line. The pretension is typically a function of submerged mooring line weight, axial stiffness and length. The dynamic effects of the mooring line also depend on the added mass coefficient and the drag coefficient. The mooring system is described in detail in ref. [5].

2.5.8 Summary of methodology for wind and wave analysis

The wave analyses are performed based on hydrodynamic input generated by Wamit and coupled non-linear response analysis simulated by Orcaflex.

- The hydrodynamic analysis account for linear wave loads, added mass, radiation damping, mean drift loads and second order wave loads by Newman's approximation. The coefficients that are used to generate the loads are calculated in Wamit by establishing a BEM-model of the pontoons and solving the Laplace equation.
- In Orcaflex a stochastic wave field is computed accounting for the wave spreading spectrum and the defined JONSWAP-spectrum. The hydrodynamic loads are applied in the instantaneous position of the pontoons by transforming the wave elevation to loads using the calculated load coefficients in Wamit. The frequency dependent added mass and damping is accounted for by a convolution integral of the velocity / position and the impulse response function.

The wind analyses are performed based on aerodynamic buffeting theory in the time domain using Windsim for generating the wind velocity field and Orcaflex for response analysis.

- In Windsim a stochastic wind field is computed accounting for the spatial co-variation and the defined one-point wind spectrum, based on the static bridge offset due to the mean loads from wind, current and waves. No interpolation in the wind field due to dynamic bridge motion is accounted for. For the low frequencies with high wind energy the variation in the wind field due to dynamic bridge motion is low, whereas higher frequencies may be more sensitive to the dynamic bridge motion. However, the wind has limited energy for these higher frequencies, and neglecting dynamic motion of the bridge when evaluating the wind field is thus considered appropriate.
- An external function iterating with Orcaflex is used for the aerodynamic analysis. The aerodynamic analysis considers both the static wind loads and the turbulent buffeting loads. Orcaflex simulates the response of the structure to the aerodynamic loads computed by the routine (see also Section 5 for further details).
 - All loads are given in three degrees of freedom, drag, lift and moment about the cross-section, and are applied in the neutral axis.
 - The static wind loads are calculated iteratively based on the deformed geometry (resulting after applying static wind loads and permanent loads).
 - The buffeting loads take into account a linearization of the turbulent wind load component, the linear damping terms and the stiffness load term.

In the combined wind and wave analysis these two stochastic load models are applied simultaneously.

The wind is applied to the center of gravity of the bridge girder in orcaflex, whereas the aerodynamic coefficients are found around the center of the bridge girder. However, the orcaflex model does not include an offset of the neutral axis/center of girder compared to the center of gravity of the girder, and the aerodynamic load is thus adequately represented. For K12_07 the difference between the CoG and the central axis is between 12 and 18 cm for the various section types, 6-9%. Hence, the road line is slightly to high in the orcaflex model, but this does not affect the response.

2.5.9 Static equilibrium of pontoons and the cable-stayed bridge

The floating bridge is ballasted, and the cantilever deflection is compensated for before connecting the floating bridge to the cable stayed bridge, ensuring a moment free transition.

For the pontoons, a unit load methodology is used to reach equilibrium between vertical forces by adding ballast mass at each pontoon. The mass balance is within 99% for all pontoons after ballasting.

For the stay-cables the calculated cable strain ϵ in RM-Bridge are used to calculate the unstressed cable lengths l_0 in OrcaFlex based on system cable lengths l .

$$l_0 = \frac{l}{1 + \epsilon}$$

2.6 Dynamic model – Novaframe

2.6.1 General model

The Novaframe model is comprised of beam elements, springs and master-slave connections. The master-slave connections are used to ensure the eccentricity of the connection between the cable and bridge elements, cable and tower elements as well as the eccentricity between the center of the bridge and top of the columns. The water stiffness is modelled using spring elements. Each element has a full set of element properties including mass, stiffness about all axes, modulus of elasticity and wind areas.

2.6.2 Numbering system

Element IDs are defined in the common excel-spread sheets. The element numbering system can be seen in Table 2-3.

Table 2-3 Element numbering system used for Novaframe

	Difference from common element system
Bridge element	+1
Column	+1000
Tower	+2000
Cables	+3000
Pontoons	Numbered as elements a 4000-series

2.6.3 Modelling of pontoons

The pontoon is modelled with beam elements with a large stiffness and 0 mass. The first element connects the top of the pontoon to the main pontoon node located in the water surface. From this, a connection element to the top of the pontoon connects the pontoon to the column. Further connection elements are used to the center of mass of the pontoon and a node representing the center of mass for the ballast. The final element is a spring element connected to a directional node. The spring element is a multidirectional spring which includes the water plane stiffness in heave, roll and pitch. Frequency dependent added mass is added to the water surface node.

As the Novaframe model is linear the update of the pontoon stability due to roll and pitch is not captured directly. To account for this, the stiffness in roll and pitch is corrected so that the stability of the pontoon connected to the bridge is adequately represented.

The buoyancy force is the weight of the displaced volume of the body. The hydrostatic (roll) stiffness is found by calculating GM which is the vertical distance the distance between the center of gravity G and the metacenter M. The metacenter is defined as the intersection between an imaginary line drawn vertically through the center of buoyancy B of an object and a corresponding line of the same object when the object is tilted. For small angles, the righting arm is approximated as

$$GZ = GM \cdot \sin\theta \cong GM \cdot \theta$$

And the righting moment is thus equal to:

$$MR = \rho g \nabla \cdot GM \cdot \theta = C44 \cdot \theta$$

The restoring coefficient is adjusted by estimating the distance GM multiplied with the restoring buoyancy force.

$$C44 = (BM - ZB - ZG) \cdot \rho g \nabla$$

where:

$BM = \frac{I_{44}}{\nabla}$: Vertical distance between center of buoyancy and metacenter

ZB: Vertical distance between water plane and center of buoyancy

ZG: Vertical distance between water plane and center of gravity

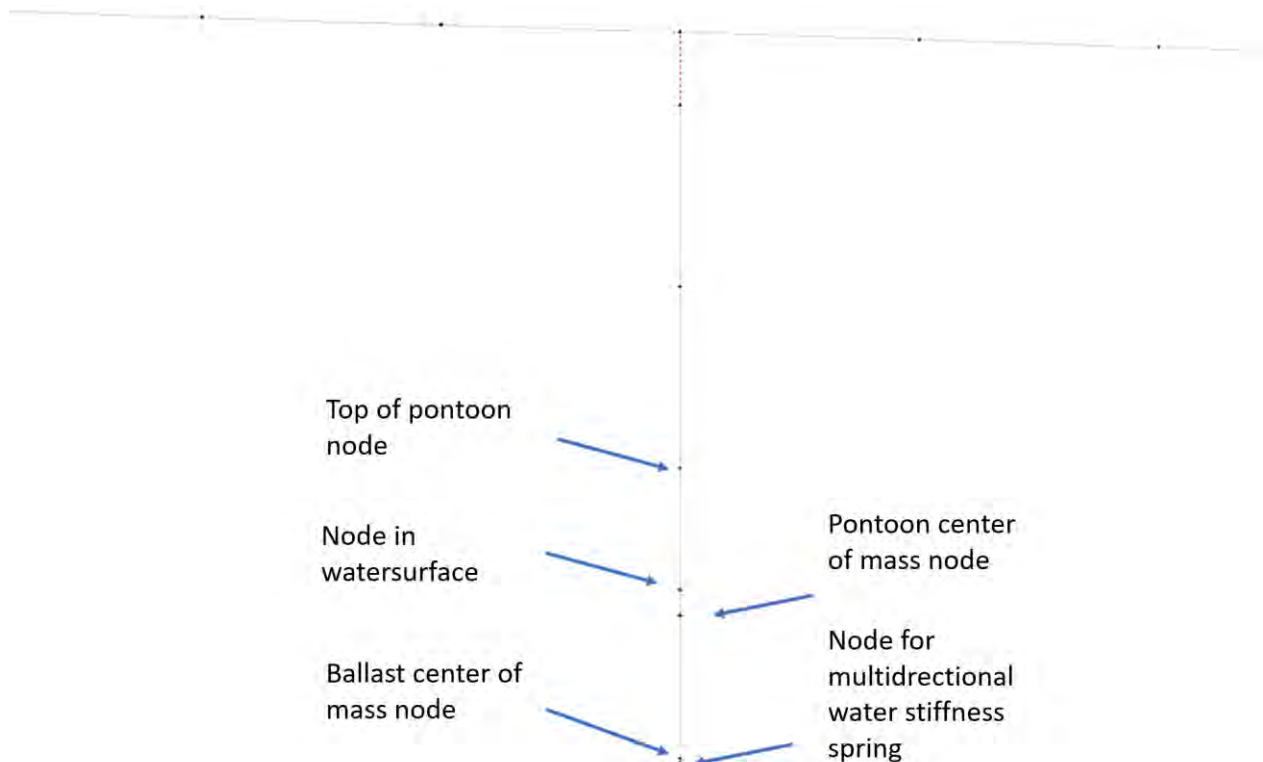


Figure 2-13 Generic representation of how the pontoons are modelled. The “node in water surface” is node 1 for all 4 elements in the pontoon.

In Figure 2-13 the pontoon and column elements are given as

1. Element from water surface node to the top of pontoon
2. Element from water surface node to pontoon centre of mass node
3. Element from water surface node to centre of ballast node
4. Spring element from water surface node to water stiffness spring node

2.6.4 Damping

Four damping components are included in the Novaframe models.

1. Structural damping
2. Aerodynamic damping
3. Pontoon potential damping
4. Pontoon viscous damping

Damping is added in terms of critical damping ratio. The structural damping is given for the section type and taken as 0.005. Aerodynamic damping is automatically calculated for the dynamic wind analysis. The pontoon potential damping is calculated for each mode with the generalized damping for each pontoon calculated with the pontoons' frequency dependent damping coefficient B and the modal response ϕ .

$$\bar{B} = B\phi^2$$

The viscous damping coefficient for the pontoons are calculated using the amplitude of the harmonic response of a wind state as shown in the formula below. The generalized damping is then calculated as previously shown. The generalized viscous is adjusted for different wind speeds and wind directions.

$$B = \frac{8}{3\pi} \omega W_{max} C_D A \rho$$

Viscous mooring damping not included in the current models.

2.6.5 Model geometry

The geometry and boundary conditions are described in the following. Mooring location and stiffness are indicated with arrows and text where the number indicates the axis number the mooring is connected to. Currently, all the boundary conditions are fixed. The boundary conditions can be seen in green. The columns without any indicated boundary conditions are resting on a pontoon. The red lines in the model represent master-slave connections.

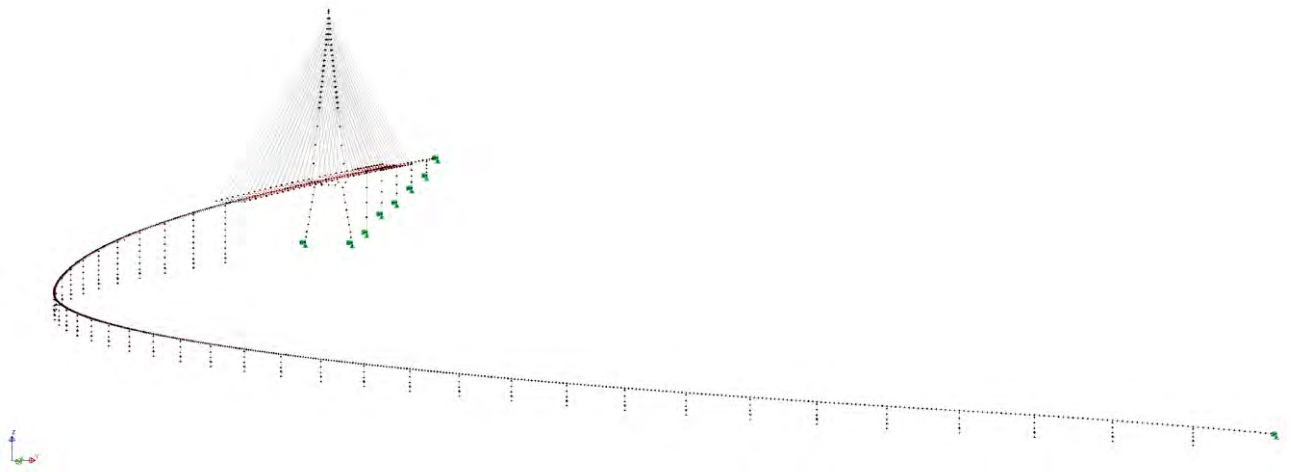


Figure 2-14 Isometric view of K12_07

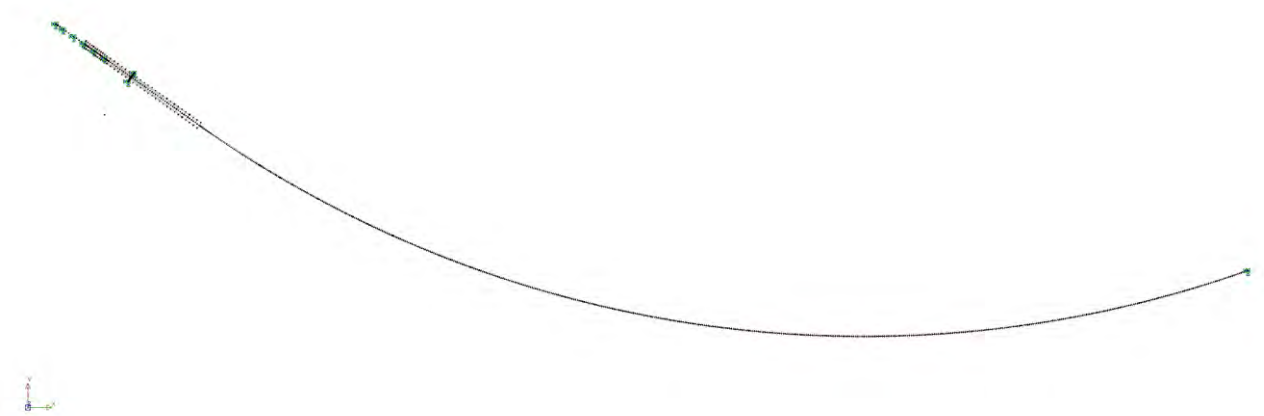


Figure 2-15 Top down view of K12_07

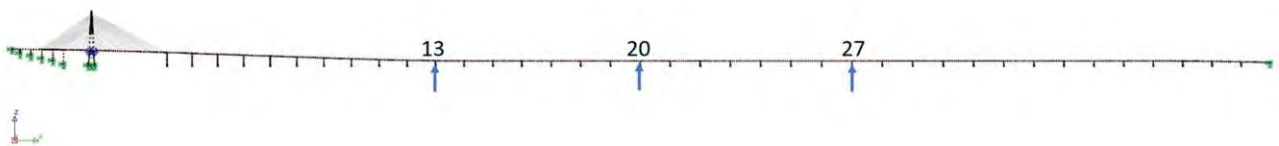


Figure 2-16 Side view of K12_07 with moorings

2.6.6 Wind loading

Wind factors are properties of all elements in Novaframe. Novaframe is used to calculate both static and dynamic wind response. Wind length scales, turbulence intensity and coherence factors are defined for each wind analysis. The wind direction is transformed to the local Novaframe coordinate system which is oriented counter clockwise with the wind direction given as the direction the wind is blowing towards. The windspeed is an input given in m/s. Static wind response is outputted as nodal displacements and elemental forces.

The dynamic analysis is performed for 110 modes for a wind state of 10 minutes duration where maximum expected forces and moments are outputted for each mode. The 1-hour wind speeds from the metocean design basis [12] were used as input for the simulation. Maximum, acceleration, displacement peak factor and standard deviation is outputted for every mode. Note that only the standard deviation from the simulation is used; the 10 minutes expected maxima are not processed further.

The standard deviation of the forces and moments are calculated by dividing the expected maximum forces and moments by the peak factor. The amplitude of the harmonically varying forces and moments are then calculated by multiplying $\sqrt{2}$. The modal harmonic response of the forces and moments are used to generate a force response time series for fatigue calculations.

$$F_{Amplitude} = \frac{F_{expected\ max}}{PeakFactor} \sqrt{2}$$

Nodal response for each mode is similarly scaled with the standard deviation found from the dynamic wind analysis. The amplitude of each nodal harmonic response is found by multiplying the harmonic modal response with the standard deviation of maximum nodal response and $\sqrt{2}$. The modal harmonic displacements of the nodes are used to generate a time series for car comfort calculations.

$$u_{node} = \frac{u_{expected\ max}}{PeakFactor} \phi_{node} \sqrt{2}$$

2.7 Dynamic model – LS-DYNA

LS-DYNA models were generated based on the same set of input data. For details of the modelling approach and assumptions, see [13].

3 Tensioning of cable-stayed bridge

The cable tensioning optimization is performed in the RM Bridge Enterprise software. A separate analysis schedule for the optimization labelled as "FormFinding" is established within the model. Only the main bridge is activated where the interface to the floating bridge part is 370m from the center of the Pylon in axis A2 (10m after the last cable stay pair in the front span).

Note that the tensioning was performed for an earlier iteration of each bridge concept, but as the modelled weight of the bridge has not changed the tensioning maintained in the new iterations.

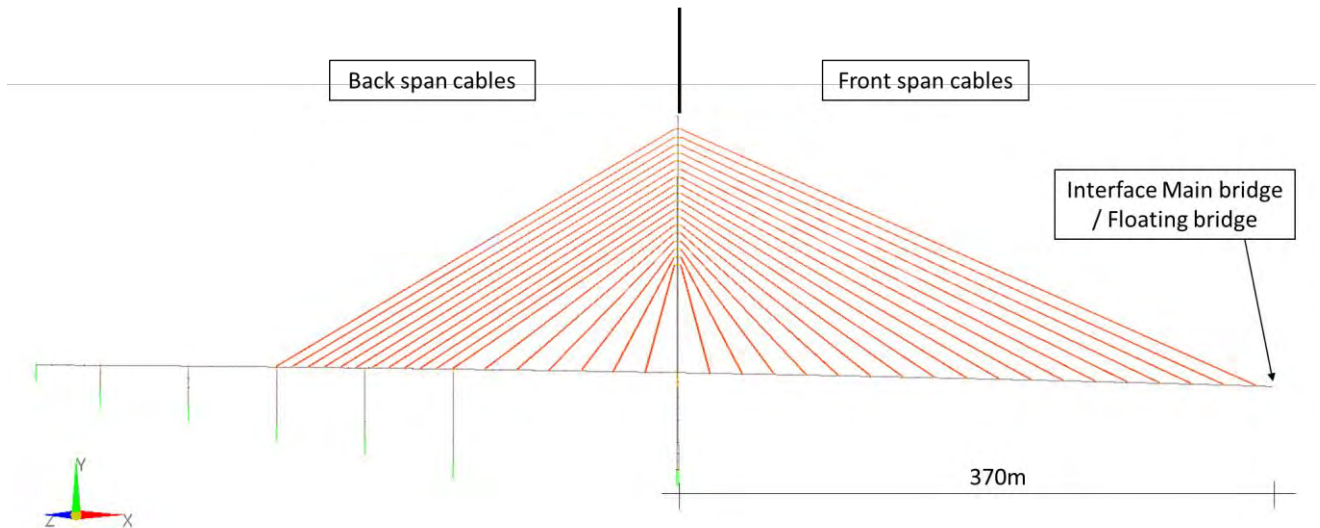


Figure 3-1: Definition of the stay cables.

Table 3-1: Cable stay element numbering system in RM Bridge.

Back span - cable elements			Front span - cable elements		
Cable #	East side	West side	Cable #	East side	West side
cable_1	21011	22011	cable_1	23011	24011
cable_2	21021	22021	cable_2	23021	25021
cable_3	21031	22031	cable_3	23031	25031
cable_4	21041	22041	cable_4	23041	25041
cable_5	21051	22051	cable_5	23051	25051
cable_6	21061	22061	cable_6	23061	25061
cable_7	21071	22071	cable_7	23071	25071
cable_8	21081	22081	cable_8	23081	25081
cable_9	21091	22091	cable_9	23091	25091
cable_10	21101	22101	cable_10	23101	25101
cable_11	21111	22111	cable_11	23111	25111
cable_12	21121	22121	cable_12	23121	25121
cable_13	21131	22131	cable_13	23131	25131
cable_14	21141	22141	cable_14	23141	25141
cable_15	21151	22151	cable_15	23151	25151
cable_16	21161	22161	cable_16	23161	25161
cable_17	21171	22171	cable_17	23171	25171
cable_18	21181	22181	cable_18	23181	25181

In the static model in RM Bridge, the cable formulation is chosen to be linear. To include the sagging effect an effective E-modulus is estimated based on the permanent load situation according to Ernst formula (section 2.2.3).

All permanent loads are applied to this static system:

- Dead and Super Dead load weight of main girder
- Dead load weight of Cable Stays.
- Pylon dead weight
- Pier dead load below the approach bridge

The above permanent loads are organized in so-called LoadSets in the RM system. These LoadSets are explained in [14]. To obtain a reasonable cable force distribution the ADDCON function in RM is used. To use this function, it is necessary to establish simple unit correction LoadSets and corresponding LoadCases taking into account corrections of the cable forces and corrections due to compression strains in the main girder and in the pylon legs and pylon crone elements. The correction load cases together with the permanent load case, and corresponding adequate conditions in RM's ADDCON function will create a reasonable solution of the cable forces measured on the jack at time of tensioning the cables. Based on the initial permanent loads, unit correction loads and the adequate conditions, ADDCON will calculate factors for the unit correction loads. These "factor x unitLoadSet" are stored together with the permanent LoadSets in the LoadCase "g-w-add1", see [14].

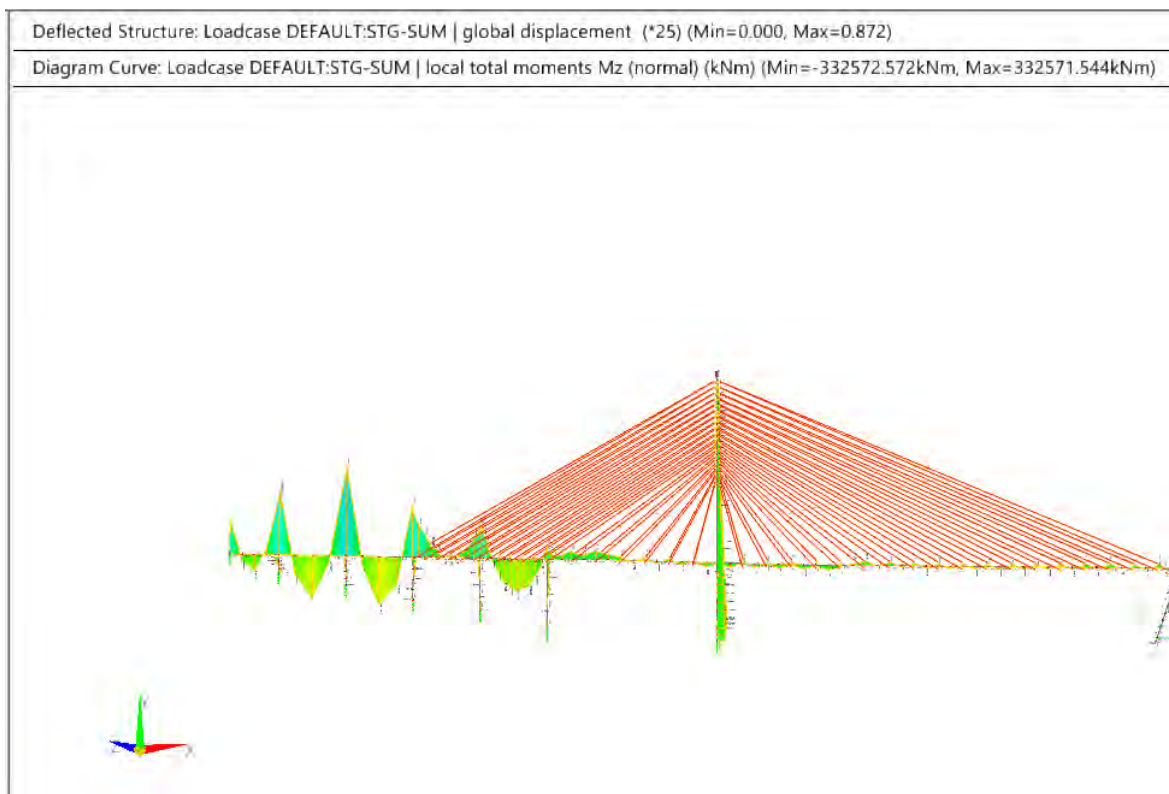


Figure 3-2: Deformation and moment distribution after cable tensioning optimization.

The Figure 3-2 shows the overall displacement and lateral moment in the main bridge after cable tensioning optimization. The vertical deformation in the front span has a variation of approximately +/- 1mm.

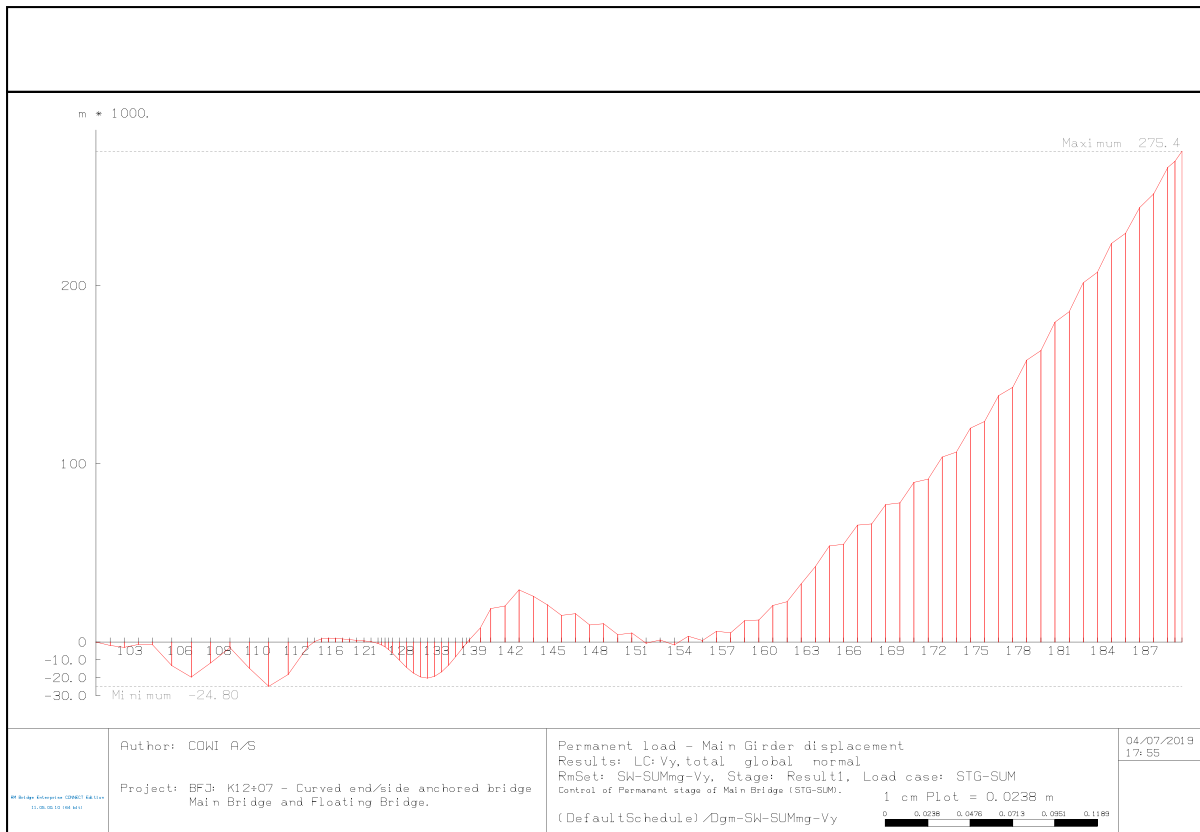


Figure 3-3: Vertical deformation of the Main girder (Cable stay bridge only).

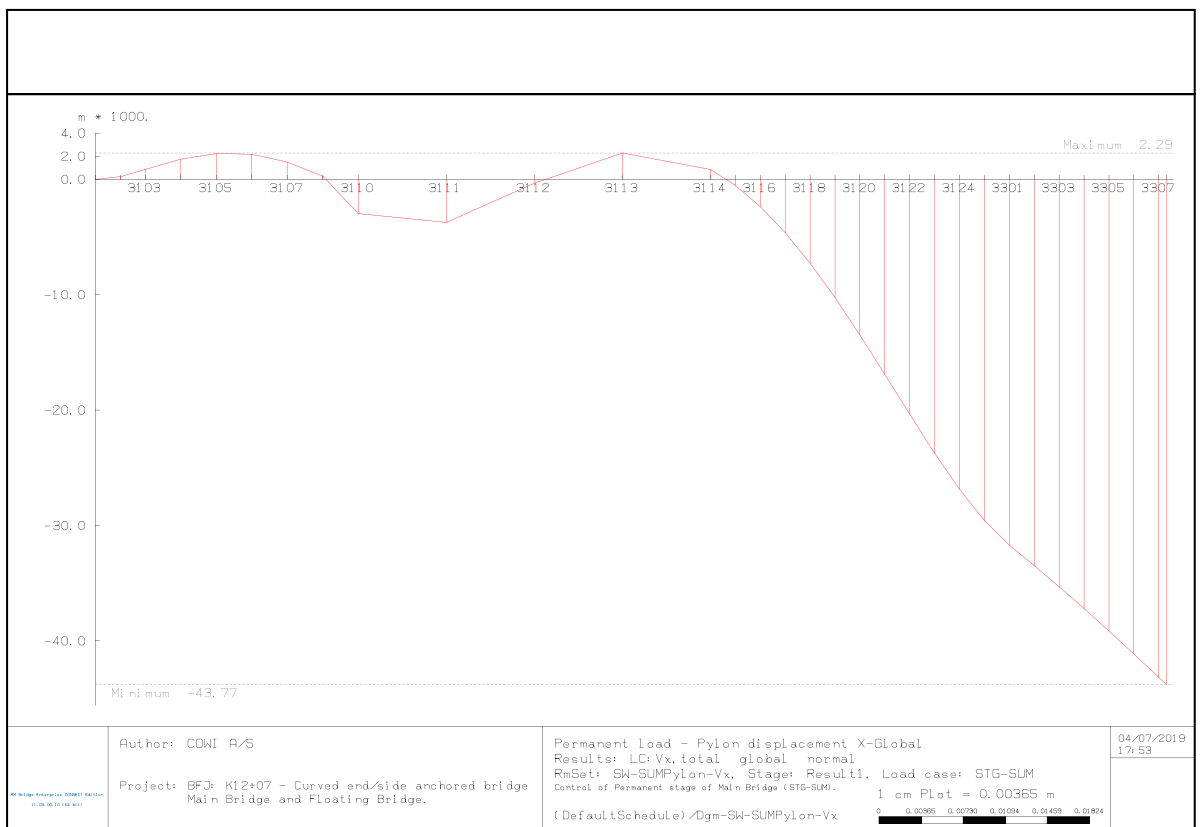


Figure 3-4: Longitudinal deformation of the Pylon (left side is the Pylon foot, right side is the top). The minus (-) sign means bending against the approach bridge.

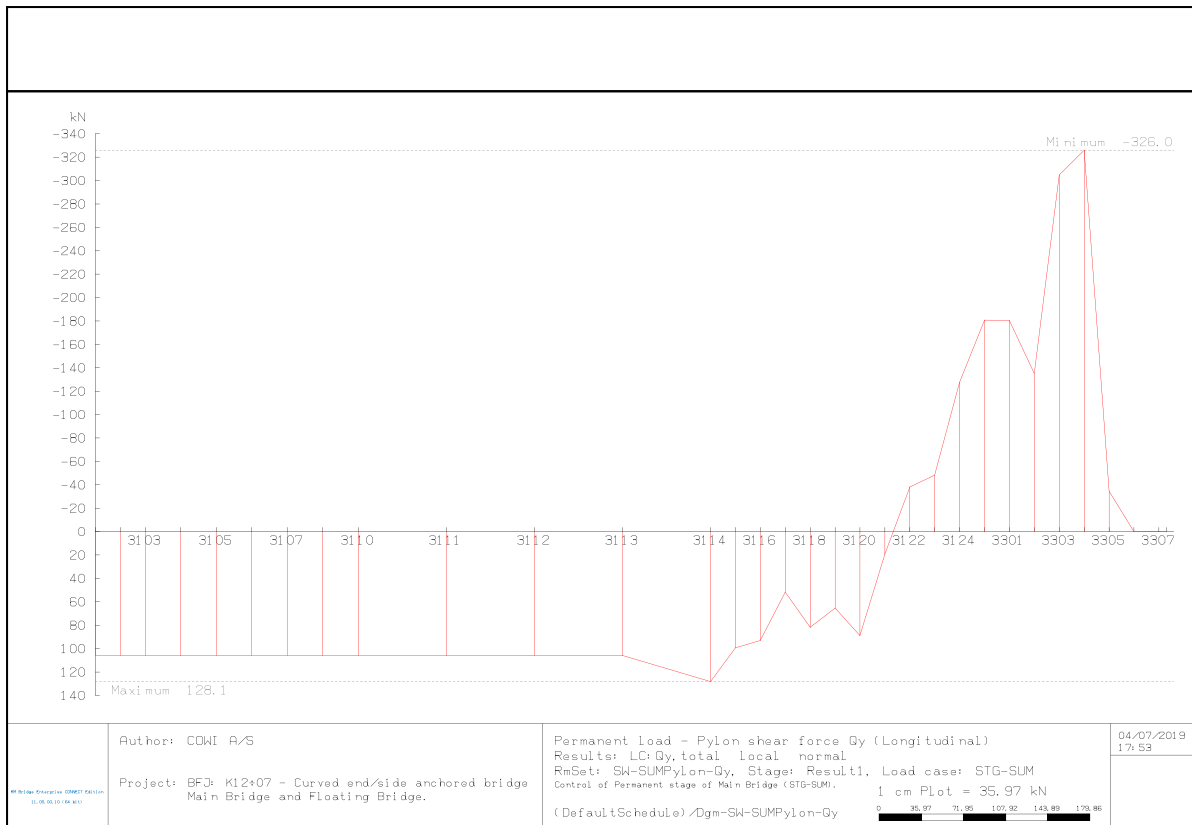


Figure 3-5: Shear force [kN] distribution of one Pylon Leg and the Pylon crane.



Figure 3-6: Cable forces measured on the jack – back and front stay cables.

The cable forces shown in Figure 3-6 are used as input to the Orcaflex and Novaframe models. The cable forces are reported at the cable end connected to the pylon.

4 Pontoon design

This section gives a short overview of the properties of the pontoons used in the studies of the bridge concepts.

4.1 Mass estimates

The buoyancy of the pontoon shall carry the total weight of the bridge structure as stated in the following equation.

$$m_0 + m_p + m_c = \rho \nabla$$

Where m_0 is the weight of the bridge deck including asphalt, columns and marine growth, m_p is the weight of the pontoon and m_c is the contingency, ρ is the density of water and ∇ is the displacement of the pontoon.

Based on previous experiences for pontoons with 3.5m freeboard, the pontoon weight is assumed to be 27% of the displacement.

$$m_p = 0.27\rho\nabla$$

Further the contingency is assumed to be 5% at present stage.

$$m_c = (m_0 + m_p) 0.05$$

Rewriting the equation on top leads to an estimate on the displacement,

$$\nabla = \frac{m_0}{\rho \left(\frac{1}{1.05} - 0.27 \right)}$$

The bridge girder weight used for pontoon design is taken as 14 ton/m for a bridge girder with 125 m span length.

Table 4-1 Pontoon displacements

Span length [m]	125
Weight of bridge girder [ton/m]	14
Weight of asphalt [ton/m]	5
Total weight of girder and asphalt [ton]	2375
Weight of columns [ton]	75
Marine growth [ton]	65
Pontoon weight (27% of displacement) [ton]	995
Contingency 5% [ton]	176
Total displacement [m ³]	3683
Chosen displacement [m ³]	3710

The chosen displacement is somewhat higher than the calculated displacement due to uncertainty in the parameters.

4.2 Pontoon geometry

The geometry of the pontoon has been the topic of investigations in previous phases, where a kayak type pontoon was found to have better response characteristics in the 100-year extreme wind wave conditions. Since, the metocean conditions for Bjørnafjorden have been updated with less severe extreme wind waves and it is not certain if the wind waves are governing for the design. In addition,

it is considered more cost-effective to construct a circrtangle shape pontoon. Therefore, a circrtangle shaped pontoon is chosen as base case for the present study, see illustration in Figure 4-1. For instance, if fatigue is found to be dimensioning, the response characteristics of the pontoon to typical fatigue environmental conditions should be optimized. If a higher viscous drag is needed due to e.g. parametric excitation the pontoons can be altered to provoke earlier vortex shedding.

The assumed structural weight of the pontoon is higher than the calculated mass of the pontoon (705 and 934 ton, see Appendix K), leaving a significant margin for weight increase without affecting the global dynamic response.

Table 4-2 Circrtangle properties

Pontoon type	Moored	Conventional
Length [m]	53	53
Width [m]	14.9	14.9
Draft [m]	7.5	5.0
Mass [ton]	1540	985
Displaced volume [m ³]	5566	3710
C33 [kN/m]	7460	7459
C44 [kNm/rad] (only contribution from water plan area)	1,56 E6	1,56 E6
Ixx [ton m ²]	415 E3	252 E3
Iyy [ton m ²]	63,8 E3	33,1 E3
Izz [ton m ²]	430 E3	252 E3
Center of gravity [m]	-2.0	-0.75

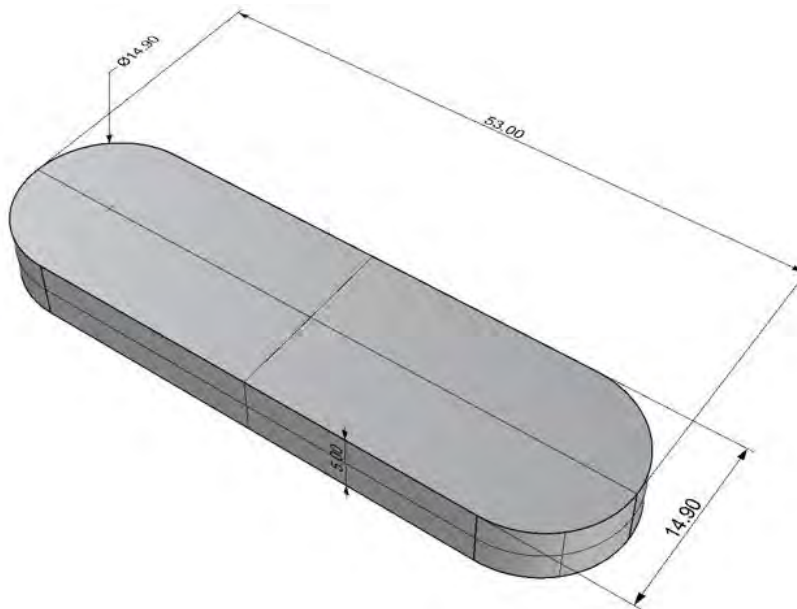


Figure 4-1 Underwater part of the circrtangle geometry selected for bridge with for 125m span width

4.3 Pontoon hydrodynamics

In the following the added mass, potential flow damping and wave excitation forces are given for the pontoon with dimensions given in Table 4-2.

The analysis results are believed to be converged with regards to mesh size. The effect of irregular frequencies has also been checked and found not to influence the results.

4.3.1 Added mass

Circtangle 53m x 14.9m x 5.0m

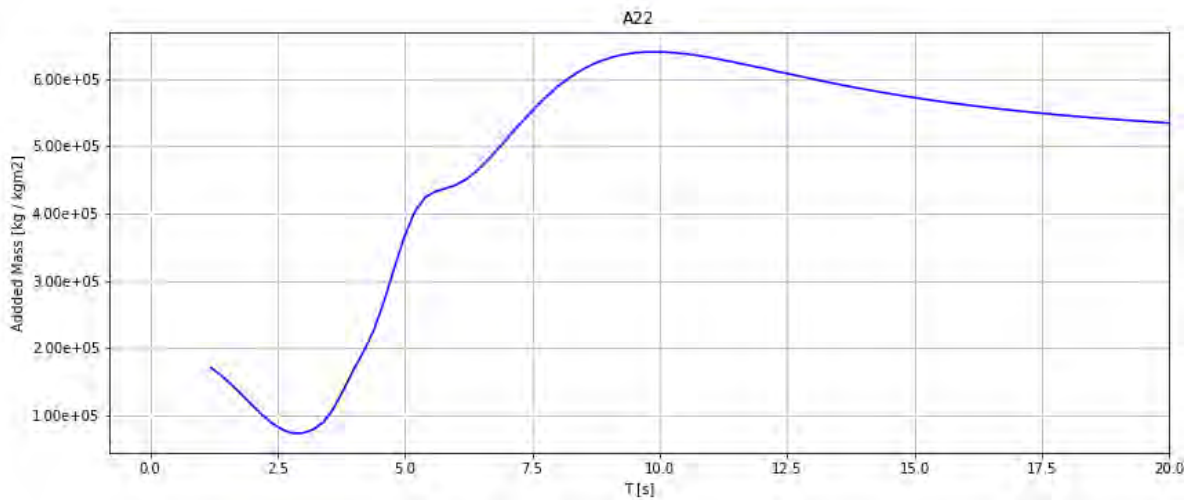


Figure 4-2 Added mass in sway

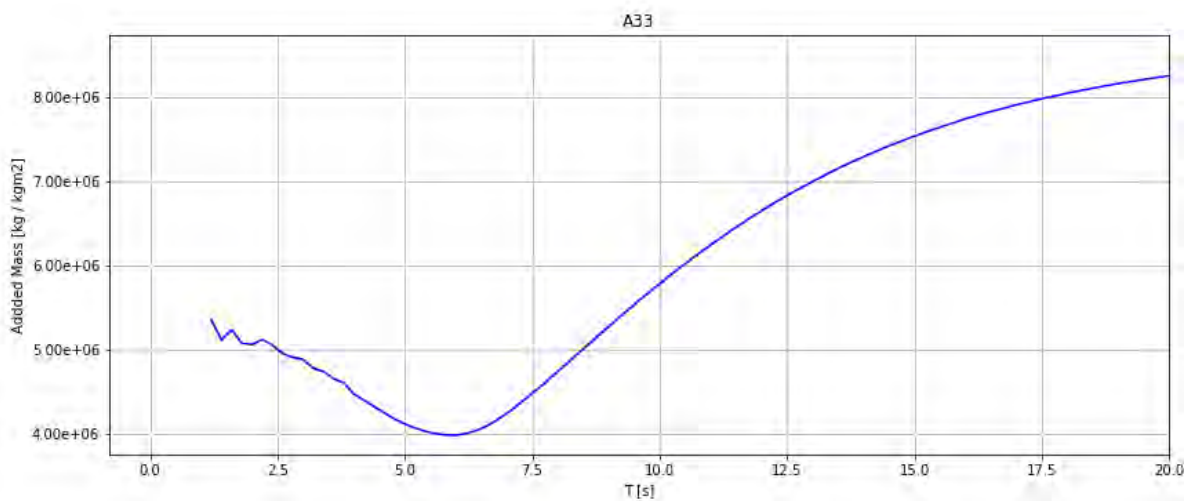


Figure 4-3 Added mass in heave

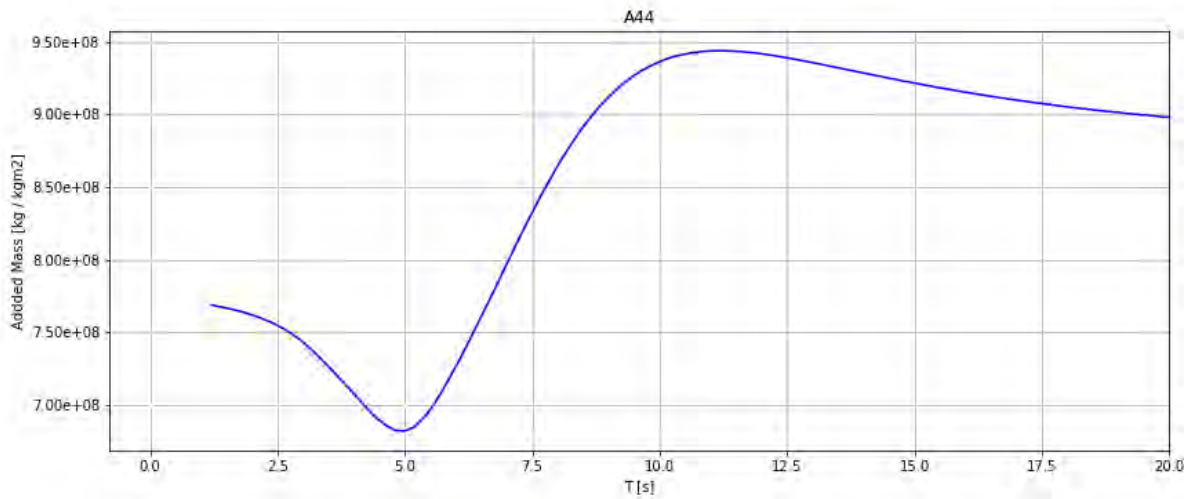


Figure 4-4 Added mass in roll

4.3.2 Potential flow damping

Circtangle 53m x 14.9m x 5.0m

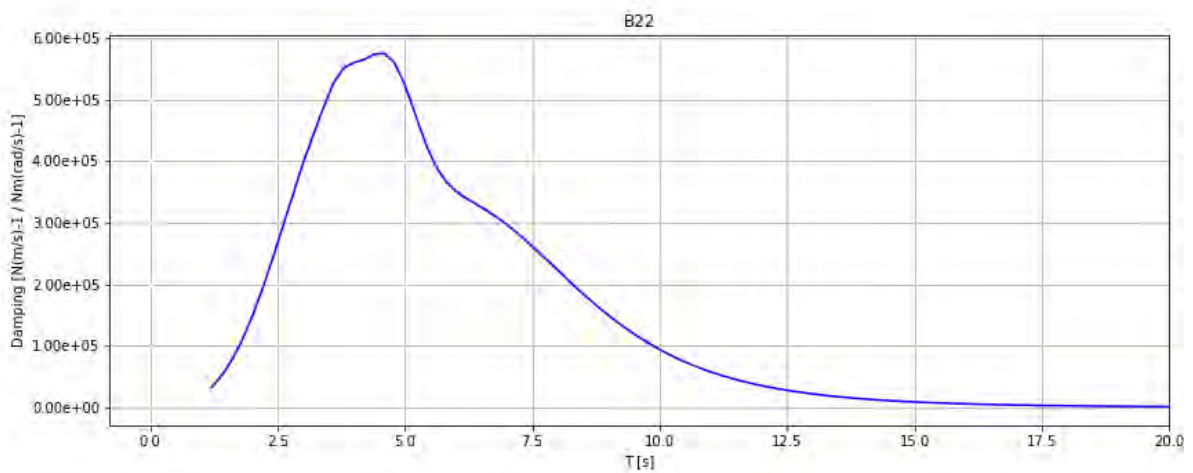


Figure 4-5 Potential flow damping in sway

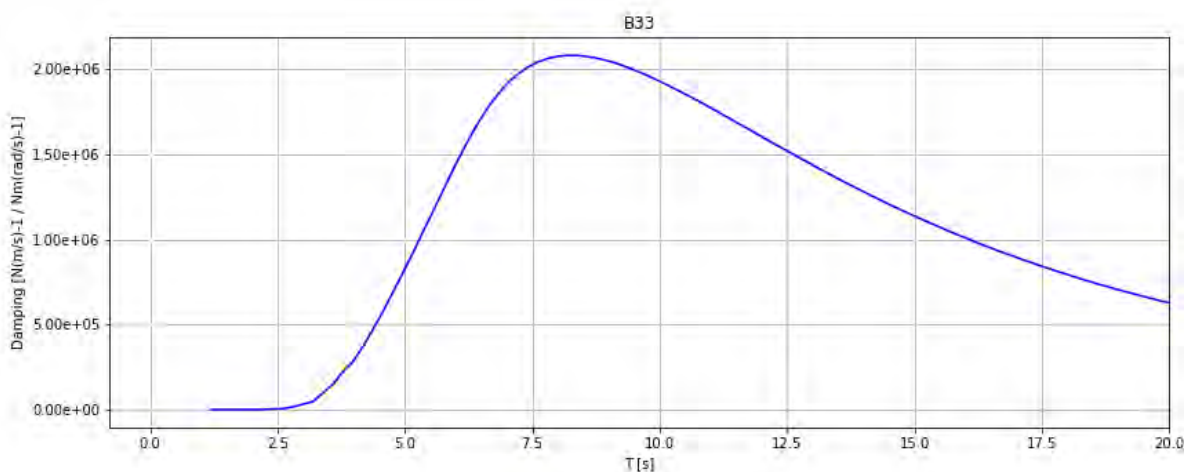


Figure 4-6 Potential flow damping in heave

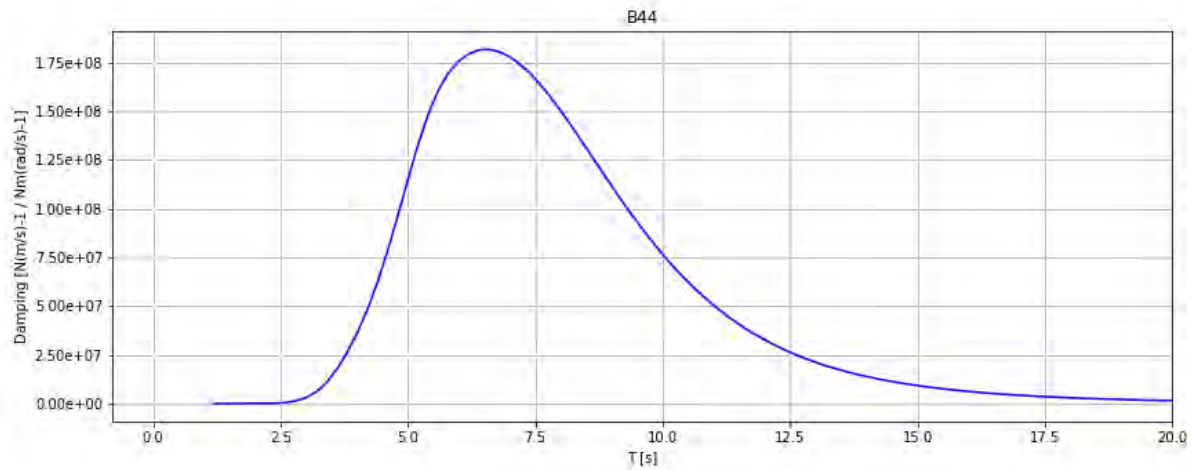


Figure 4-7 Potential flow damping in roll

4.3.3 Wave excitation forces

Circtangle 53m x 14.9m x 5.0m

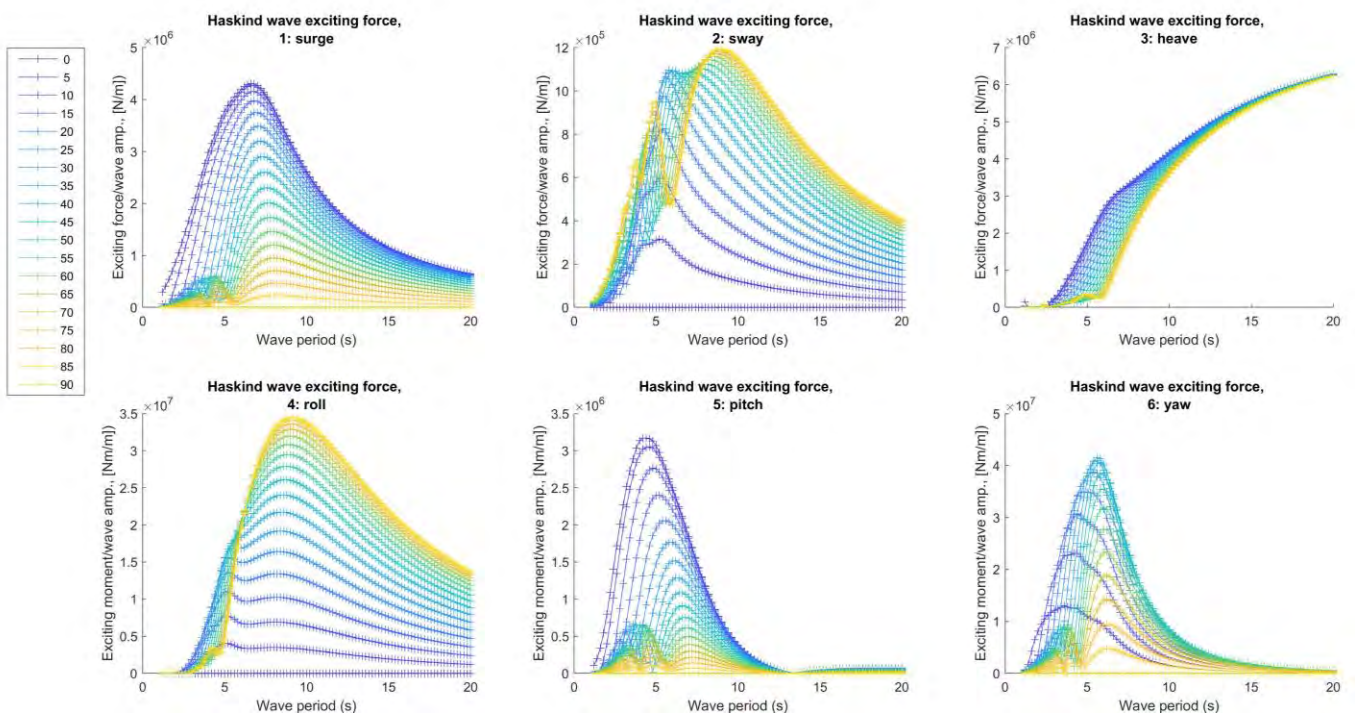


Figure 4-8 Wave excitation forces

4.3.4 Force divided by damping

Throughout the previous phases it has been found that the relationship $F_j(\omega) / i \omega B_{jj}(\omega)$ based on hydrodynamical coefficients can be used as a measure to select pontoons without checking the response in the global model for all alternatives.

Below are results for the chosen pontoon along with the pontoon used earlier for the bridge with 100 m span.

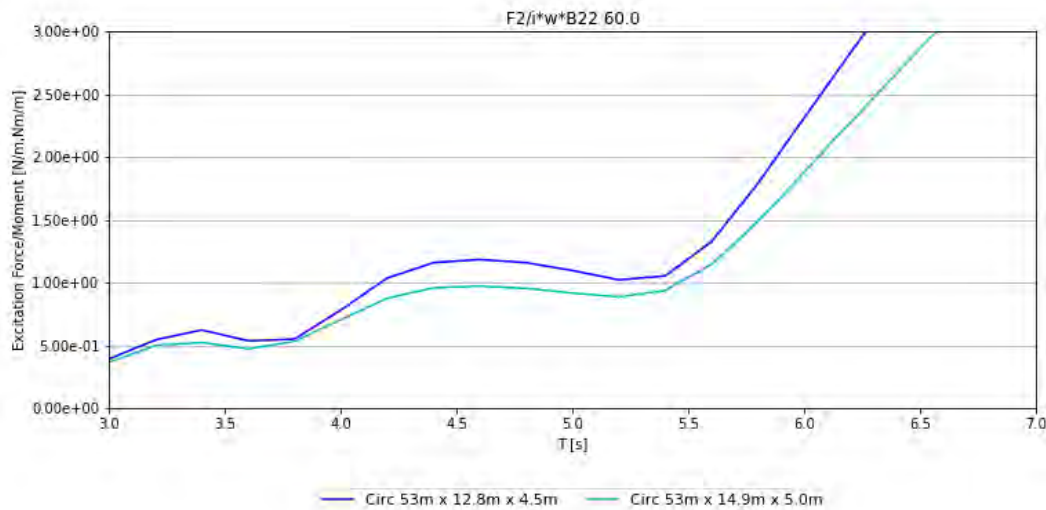


Figure 4-9 Force divided by damping comparison for sway with waves from 60 degrees of the bridge axis

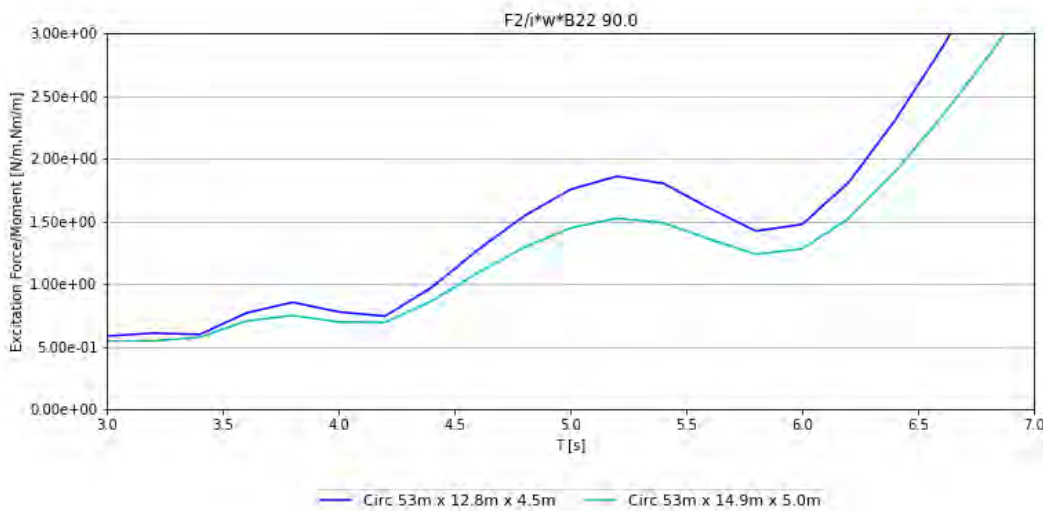


Figure 4-10 Force divided by damping comparison for sway with waves from 90 degrees of the bridge axis

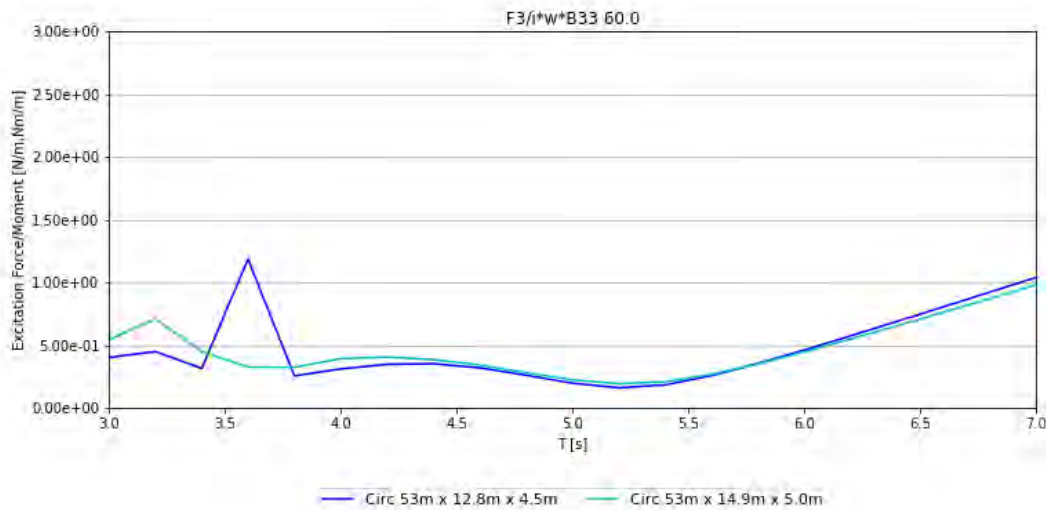


Figure 4-11 Force divided by damping comparison for heave with waves from 60 degrees of the bridge axis

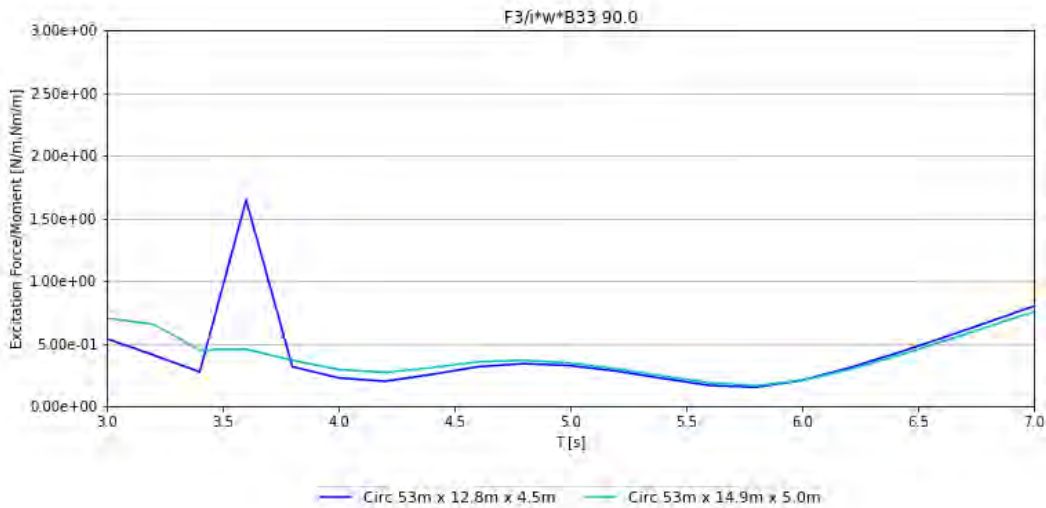


Figure 4-12 Force divided by damping comparison for heave with waves from 90 degrees of the bridge axis

4.4 Viscous damping

For the present geometry it has been challenging to determine a proper drag coefficient only based on literature. The drag coefficients are dependent on the velocity/motion amplitude (through the KC number) and to some extent the period. Depending on the geometry, the coefficients for stationary flow may or may not provide the lowest values compared to oscillating flow.

CFD studies performed late in the project shed some light on the possible range of coefficients, but model testing is required at a later stage. The stationary drag coefficient in the transverse direction was found to be 0.4, whereas the oscillatory drag coefficient shows large variations and a significant increase as the KC number approach 0 (approach small velocity/motion amplitudes).

The findings are discussed in detail in Appendix H [15]. Figure 4-13 shows the recommended values.

Orcaflex allow to separate low-frequent and wave-frequent viscous loading. A stationary drag coefficient of 0.4 was selected for low-frequent motion, defined as a period above 20 s, and a drag-coefficient of 0.8 was used for motion with lower periods than 20s. The latter was chosen as a

conservative estimate of the drag coefficient at low KC numbers (valid for $KC < 2$ based on the recommendation in Figure 4-13), in line with the motion response amplitudes observed in the numerical simulations.

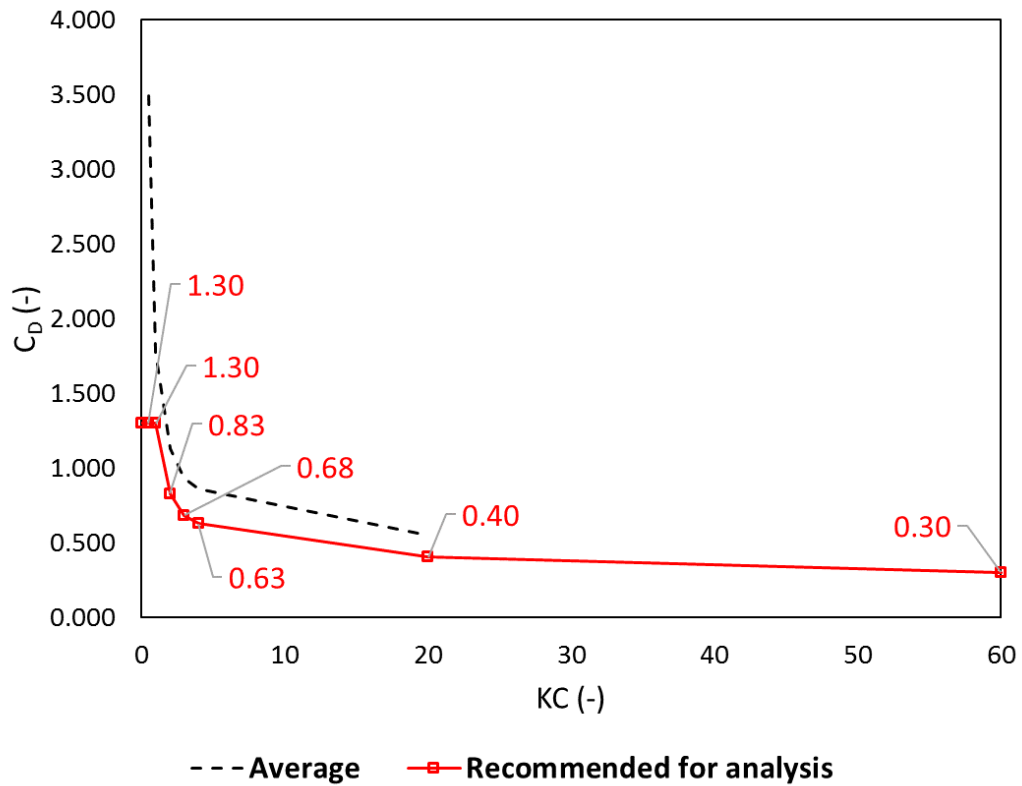


Figure 4-13 KC-dependent Morison drag coefficients for pontoon proposed for global analysis model (red line with square markers). The numbers indicate the value of the drag coefficient in the different data points.

5 Description of the aerodynamic buffeting analysis

This section gives an overview of the methodology used for the wind analyses. The analysis is performed by aerodynamic buffeting analysis in the time domain in Orcaflex.

In order to simulate the dynamic wind loads, an external function has been developed based on linear quasi-static wind theory that maps a pre-generated wind field onto the line elements in OrcaFlex.

The wind loads and moments are calculated considering the wind field together with the instantaneous position and structural velocity of the line elements. The procedure can be used both for wind analyses without waves, and for combined wave and wind analysis.

Skew wind is not accounted for.

5.1.1 Wind field simulation

Turbulent wind time series are simulated in the WindSim code for a set of positions based on mean wind speed, gust spectrum and coherence functions. The code is using inverse FFT to generate the wind speed time series from a spectral description of the fluctuating wind components.

WindSim facilitates the N400 description of the wind environment. The metocean design basis [12] has some deviations from the N400 standard with respect to length scales and turbulence intensities. For a discussion of necessary adaptations used, see Appendix E [6]. The simulations herein are based on the adaptations given in Appendix E.

5.1.2 Linear quasi-static wind theory

In general, the instantaneous wind load and moment per unit length of the bridge is given as

$$F_{D,WD} = \frac{1}{2} \rho C_D(\alpha) H \tilde{U}^2$$

$$F_{L,WD} = \frac{1}{2} \rho C_L(\alpha) B \tilde{U}^2$$

$$M_{WD} = \frac{1}{2} \rho C_M(\alpha) B^2 \tilde{U}^2$$

Where:

$F_{D,WD}$	Drag force per unit length in the dynamic wind coordinate system
$F_{L,WD}$	Lift force per unit length in the dynamic wind coordinate system
M_{WD}	Moment per unit length in the dynamic wind coordinate system
α	Azimuth angle
C_D	Drag load coefficient
C_L	Lift load coefficient
C_M	Moment coefficient
H	Reference height
B	Reference length
\tilde{U}	Instantaneous relative wind velocity

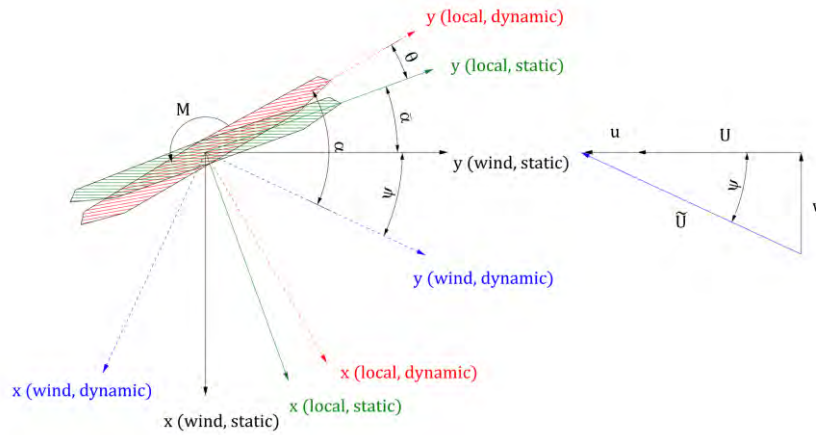


Figure 5-1 Sketch of an inclined bridge cross-section and corresponding load components

In linear theory, the quadratic wind speed and wind load coefficient is linearized

$$\bar{U}^2 = U^2 + 2uU + u^2 + w^2 \approx U^2 \left(1 + 2\frac{u}{U} \right)$$

$$C(\alpha) = \bar{C} + \alpha_f C'$$

$$C(\alpha) = [C_D(\alpha) \quad C_L(\alpha) \quad C_M(\alpha)]^T, \quad \bar{C} = [\bar{C}_D \quad \bar{C}_L \quad \bar{C}_M]^T, \quad C' = [C'_D \quad C'_L \quad C'_M]^T$$

The dynamic components u and w includes the gust wind speed and structural velocity. The horizontal dynamic component u is assumed small compared to the mean wind speed U

$$\alpha_f = \alpha - \bar{\alpha} = \psi + \theta = \frac{w}{U + u} + \theta \approx \frac{w}{U} + \theta$$

The complete linearized expression for the wind force in the static wind coordinate system is hence

$$F_{D,WS} = \frac{1}{2} \rho H U^2 \left(\bar{C}_D + 2\bar{C}_D \frac{u}{U} + \left(C'_D - \frac{B}{H} \bar{C}_L \right) \frac{w}{U} + C'_D \theta \right)$$

$$F_{L,WS} = \frac{1}{2} \rho B U^2 \left(\bar{C}_L + 2\bar{C}_L \frac{u}{U} + \left(C'_L + \frac{H}{B} \bar{C}_D \right) \frac{w}{U} + C'_L \theta \right)$$

$$M_{WS} = \frac{1}{2} \rho B^2 U^2 \left(\bar{C}_M + 2\bar{C}_M \frac{u}{U} + C'_M \frac{w}{U} + C'_M \theta \right)$$

Where:

- $F_{D,WS}$ Drag force per unit length in the static wind coordinate system
- $F_{L,WS}$ Lift force per unit length in the static wind coordinate system
- M_{WS} Moment per unit length in the static wind coordinate system
- \bar{C} Wind load coefficient at static wind angle of attack (mean wind load coefficient)
- C' Linear slope of the wind load coefficient at static wind angle of attack
- U Mean wind speed

5.1.3 Comparison between linear and nonlinear buffeting response

Linear buffeting theory was chosen in order to keep the same type of assumption between Novaframe and Orcaflex and avoid challenges with large changes of aerodynamic coefficients in the incident angle of wind in the vertical plane, but the implemented wind code supports both options. A comparison of bridge response under linear and nonlinear buffeting was performed in the Phase 3 of the project (but not documented with a reference). Figure 5-2 and Figure 5-3 show the comparison (for the straight side-anchored bridge in phase 3) for a 100-year wind event. The strong-axis moment is somewhat increased with nonlinear buffeting theory, whereas the weak-axis moment shows less sensitivity.

For future calculations it is recommended consider full nonlinear theory, but this may require a more comprehensive wind tunnel test regime.

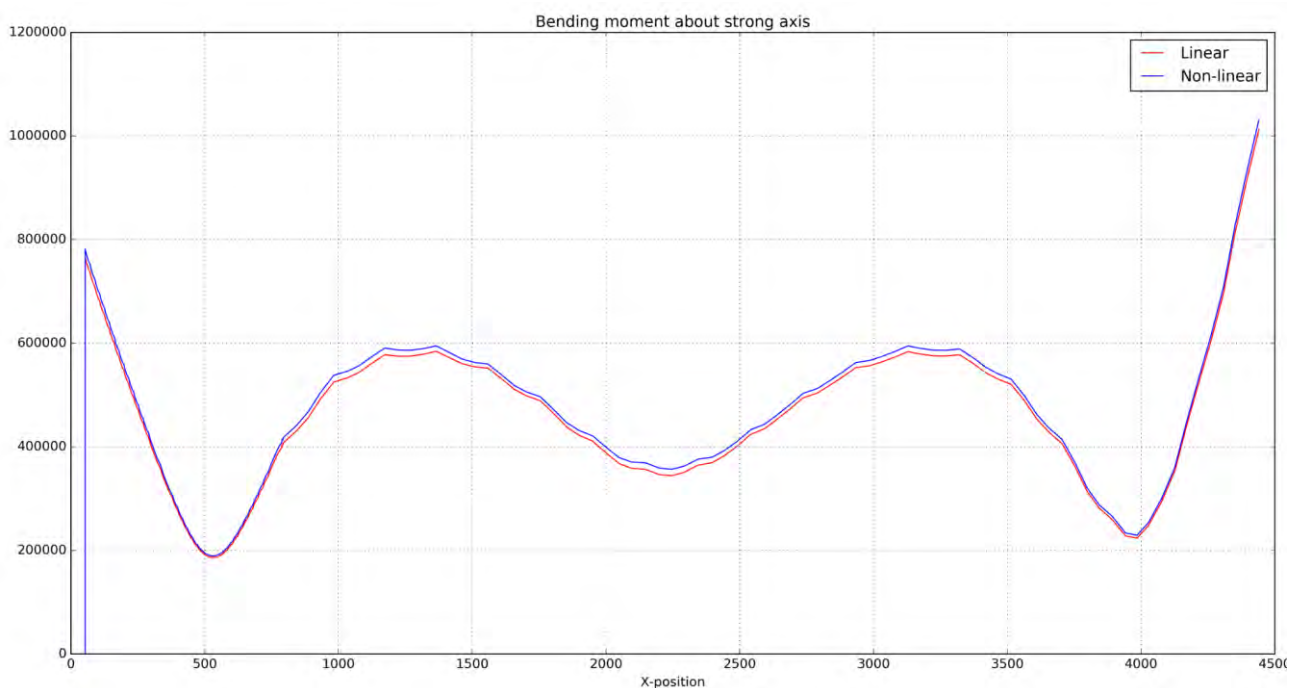


Figure 5-2 Comparison of strong-axis bending moment between linear and nonlinear buffeting response from Phase 3.

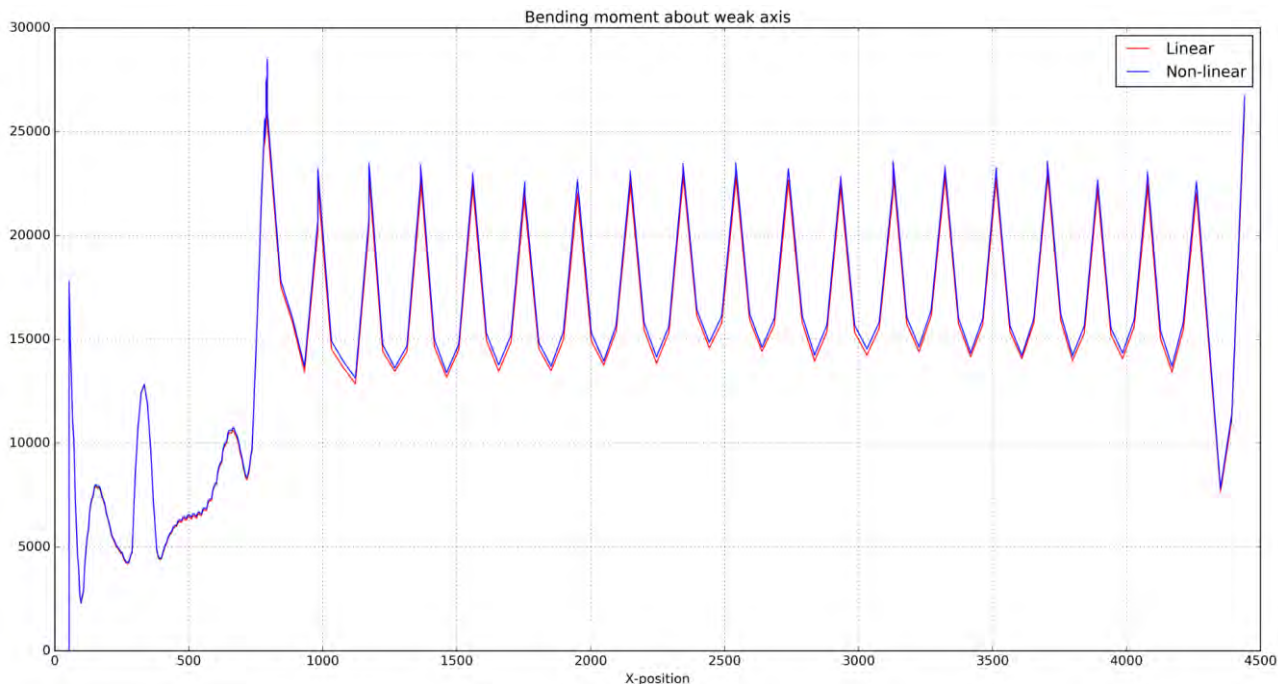


Figure 5-3 Comparison of weak-axis bending moment between linear and nonlinear buffeting response from Phase 3.

5.1.4 Wind load simulation

The wind load coefficients are given explicitly on a quadratic form to the external OrcaFlex function.

$$C(\alpha) = a\alpha^2 + b\alpha + c$$

$$C'(\alpha) = 2a\alpha + b$$

The coefficients are user-specified values for quadratic polynomial parameters (a, b, c) for each individual line type. During static calculation stage in OrcaFlex, the mean load coefficients \bar{C} are calculated based on iteration of the static azimuth angle $\bar{\alpha}$ at each wind load point along the line elements in the model. The max coefficient within a range of plus/minus 2 degrees from the static azimuth angle is used in the analysis to compensate for the uncertainty of the vertical wind direction.

$$\bar{C} = \max(C(\bar{\alpha} \pm 2))$$

The mean derivate coefficients \bar{C}' do not include the uncertainty angle.

$$\bar{C}' = C'(\bar{\alpha})$$

During the dynamic simulation, the external function will have access to both the instantaneous gust wind speed at the position and velocity of the structural element. The wind loads are calculated according to theory described above, transformed to the dynamic local coordinate system (element coordinate system) in OrcaFlex and included in the analysis using applied loads. Since both structural gust wind speed and structural velocity is available to the external function, aerodynamic load excitation and damping are both represented.

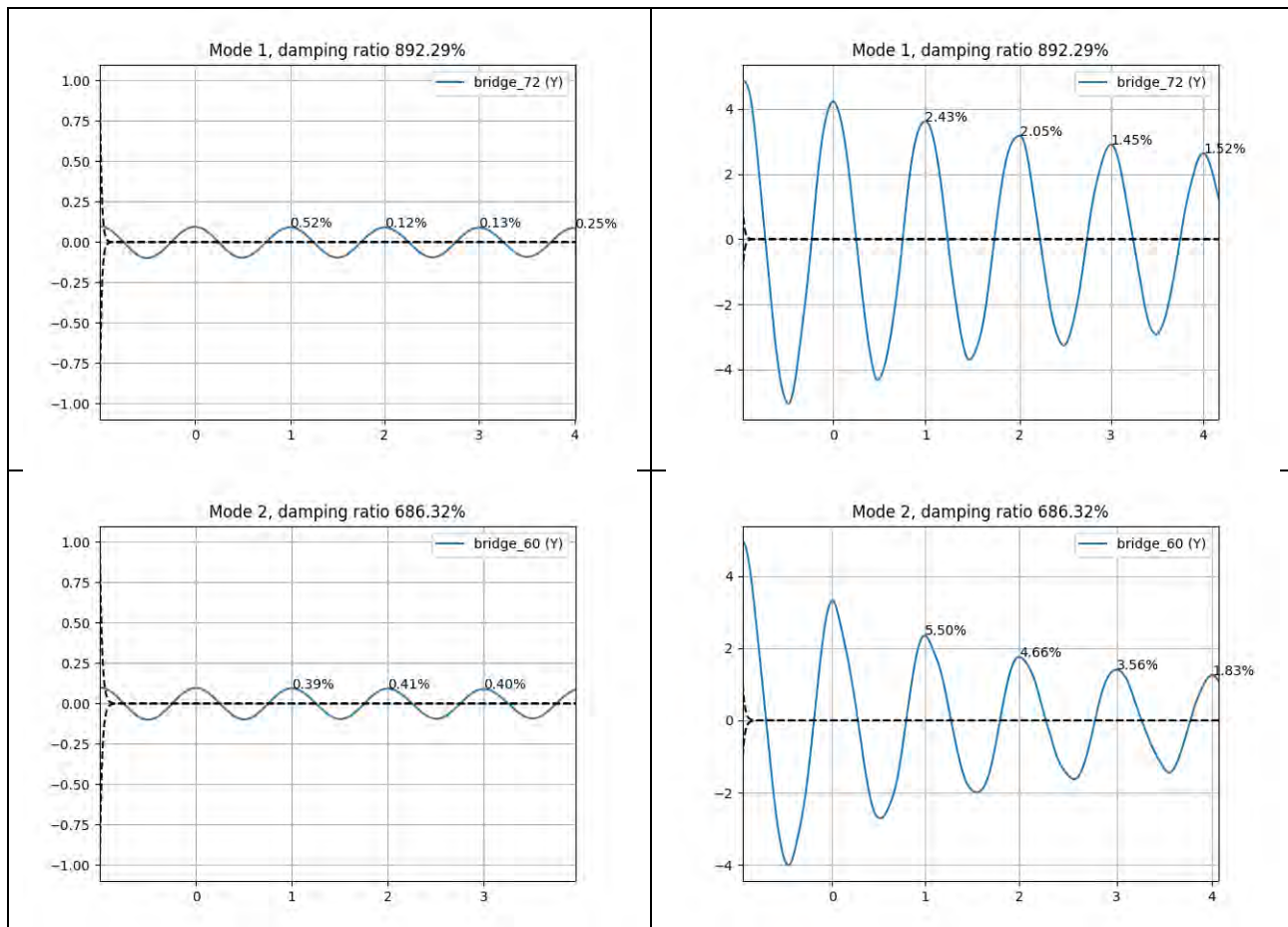
6 Global damping and modal analysis

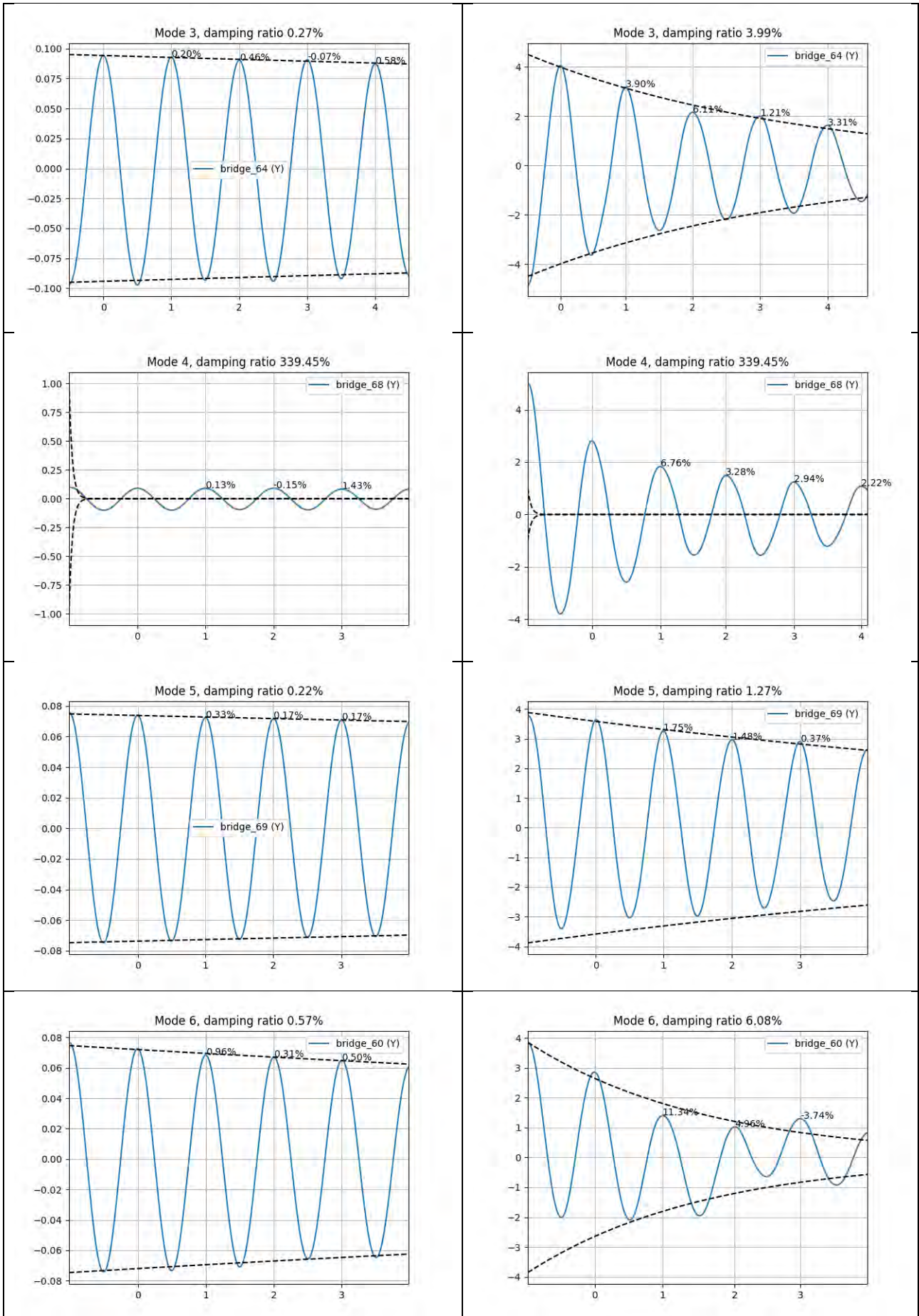
6.1 Decay tests

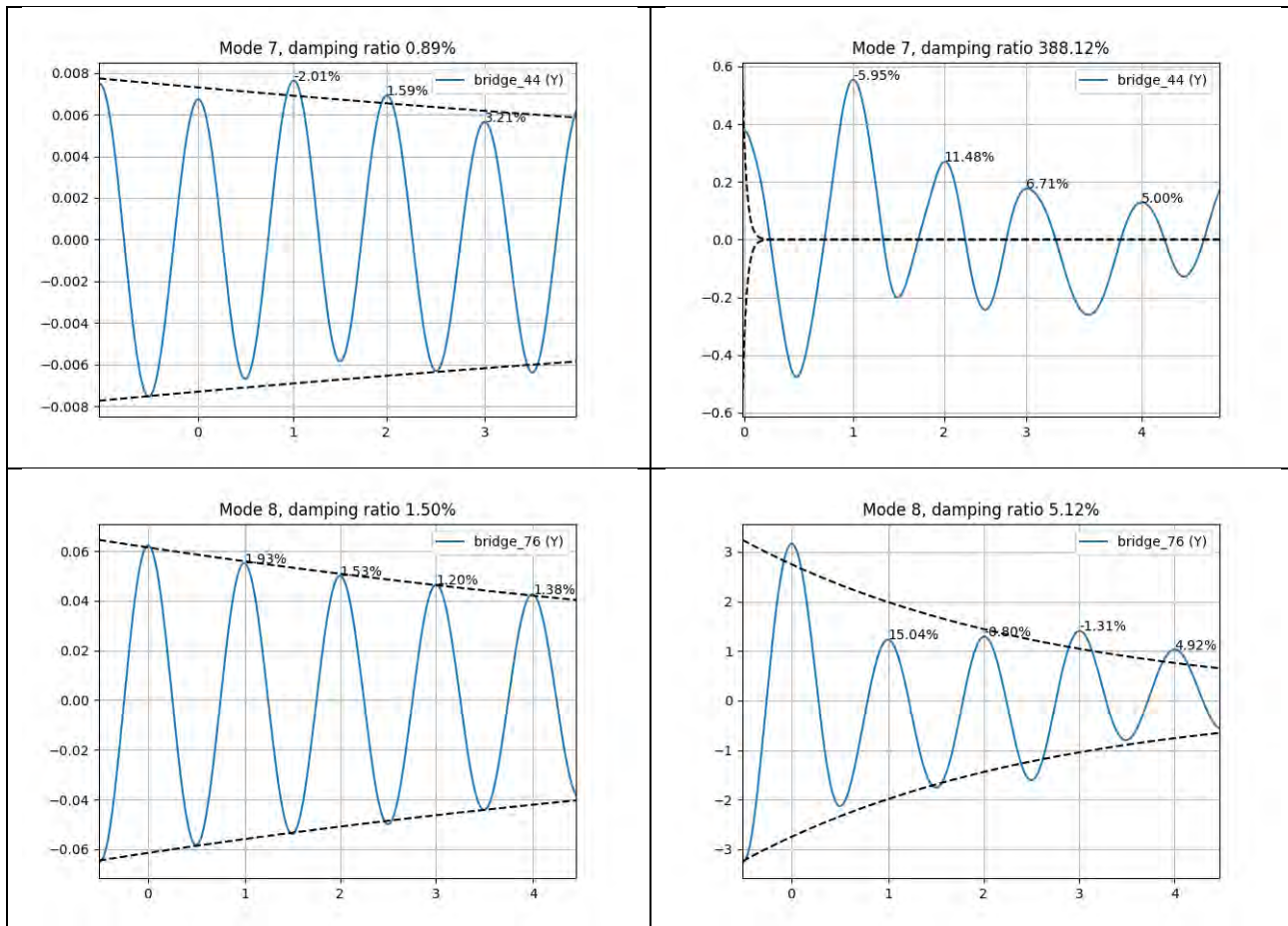
Damping ratios found in the global Orcaflex model are shown in the following. In the simulations the mooring stiffness is included as linear springs and quadratic mooring line damping as described in [11]. Decay simulations were performed in which the bridge is deformed into a specific mode shape with a specific amplitude and then released. The damping ratio is calculated based on the logarithmic decrement (defined as the natural log of the ratio of the amplitudes of any two successive peaks).

Note: The damping ratio given in the title of each subfigure is only representative when the dotted curve follows the peaks of the decay.

Figure 6-1 Plot of decay simulations for the 8 first eigenmodes for the K12 concept, at 0.1m initial amplitude (left) and 5m initial amplitude (right).







6.2 Modal analysis

Floating bridges are prone to a more complex behavior than more traditional bridges. To ensure that the modes can describe the true dynamic behavior, the modal analysis should be performed in a more refined manner than what is classically the case; i.e., it should be treated as a frequency-dependent and non-classically damped eigenvalue problem. The vibration modes corresponding to the bridge concepts are in the following used as a tool to better understand their dynamic behavior. More details about the procedure and the key results obtained from the analysis of the four considered concepts are given in the following sections.

6.2.1 Modal analysis: solving the frequency-dependent eigenvalue problem

The modes of the full system, including hydrodynamic and aerodynamic frequency-dependent contributions to mass, damping and stiffness, can be solved according to the methodology in [16]. This relies on the solution of the complex eigenvalue problem, which does not assume anything about the damping in the system, and thus gives a more complete picture of the modes at play.

Dry modes are defined as the modes from a system excluding hydrodynamic and aerodynamic frequency-dependent mass, damping, and stiffness, and thus, does not represent the true system. The modal transformation matrix $[\phi_0]$, and the modal mass m_0 and natural frequencies $\omega_{n,0}$ for all modes are established using the Novaframe model, described in Section 2.6. The modal transformation matrix corresponding to the dry modes transforms generalized degrees of freedom (DOFs) $\{y\}$ to physical DOFs $\{u\}$, as follows:

$$\{u\} = [\phi_0]\{y\}$$

The contributions from hydrodynamics and aerodynamics are included by first transforming them to the coordinate basis defined by the dry modes in $[\phi_0]$. The resulting system matrices are used to conduct a second eigenvalue solution, which results in a transformation matrix $[\psi]$ that transform the true generalized coordinates $\{q\}$ to dry generalized coordinates $\{y\}$, as follows:

$$\{y\} = [\psi]\{q\}$$

The physical DOFs $\{u\}$ are therefore related to the true generalized degrees of freedom (DOFs) $\{q\}$ as follows:

$$\begin{aligned}\{u\} &= [\phi_0]\{y\} \\ &= [\phi_0][\psi]\{q\}\end{aligned}$$

This implies that the total modal transformation matrix is given as $[\phi] = [\phi_0][\psi]$. Because the system matrices are frequency-dependent, the eigenvalue problem is solved by iteration [16]. The following aspects make the potential usage of the predicted modes limited, compared to more traditional problems:

1. Because the damping is non-classical, the damping matrix does not become diagonal when transforming with the modal transformation matrix resulting from the undamped eigenvalue problem. As a consequence, the eigenvalues and eigenvectors will become complex-valued. This implies that the contributions to the physical response from one mode does not reach their maximum at the same time instance; but rather, they are responding with relative phase shifts between them. The mode shape plots following in this section are therefore given at the phase that maximizes the real part of the mode shapes.
2. Because there are frequency-dependent contributions to the overall system matrices, the eigenvalue problem is solved by iteration. In principle, this assumes that the resulting modal values are only valid at the mode's natural frequency, i.e., for resonant behaviour. A mode's contribution to the physical response will depend on what frequency the mode is loaded at. Still, this is assumed as a fair approximation, and it is also believed to be the best result available to characterize the modes of the system.

6.2.1.1 Assessment of the diagonality of the modal equation system

The response of a system exposed to external forces be computed in the frequency domain using the following expression:

$$\{U(\omega)\} = [H(\omega)]\{P(\omega)\}$$

Here, $\{U(\omega)\}$ and $\{P(\omega)\}$ are the frequency domain representations of system response and external force, respectively; and $[H(\omega)]$ is the frequency response function (FRF) matrix (frequency-domain transfer function). By considering the equation of motion of a structural system with frequency dependent system matrices, the FRF matrix can be determined as follows:

$$[H(\omega)] = (-\omega^2[M(\omega)] + i\omega[C(\omega)] + K[\omega])^{-1}$$

As this matrix fully characterizes the relation between forces and displacements in all DOFs, it is a convenient choice to study how much the modal equation system is coupled. The modal system matrices may be established, exemplified with the mass, as follows:

$$[M^*(\omega)] = [\psi]^T [\tilde{M}(\omega)] [\psi]$$

where $[\tilde{M}(\omega)]$ is the total system mass matrix described using the coordinate basis defined by the dry modes. By using the modal system matrices, a modal FRF matrix is established. This matrix can be evaluated at each frequency, to establish a measure of the diagonality of the matrix at that frequency value:

$$\mathfrak{D}(\omega) = \frac{\|Diag [H^*(\omega)]\|}{\|[H^*(\omega)]\|} \quad (1)$$

where $Diag$ and $\|\cdot\|$ represent the diagonal and *Frobenius* norm of a matrix, respectively. For diagonal FRFs, indicating uncoupled equation systems, the value of this factor is 1.0. For matrices where the off-diagonal terms increasingly dominate, the value converges towards 0.

The values of the diagonality factor is listed for frequency values of the damped natural frequency of the modes, for each concept, in Section 6.2.2.

6.2.1.2 Assessment of the complexity of the modes

The degree of complexity of a mode is assessed by the modal phase collinearity (MPC) factor, commonly used in the scientific community of operational modal analysis (see, e.g., [17]). The MPC factor describes the correlation between the real and imaginary parts of the mode shape under consideration, such that real modes yield values close to 1. The MPC of a mode characterized by mode shape $\{\phi_n\}$ with N DOFs is computed as follows [18]:

$$MPC = \left(\frac{\lambda_1 - \lambda_2}{\lambda_1 + \lambda_2} \right)^2$$

where the following expressions are introduced for readability:

$$\sigma_x^2 = Re\{\phi_n\}^T Re\{\phi_n\}$$

$$\sigma_y^2 = Im\{\phi_n\}^T Im\{\phi_n\}$$

$$\sigma_{xy} = Re\{\phi_n\}^T Im\{\phi_n\}$$

$$\eta = \frac{\sigma_y^2 - \sigma_x^2}{2\sigma_{xy}}$$

$$\lambda_{1,2} = \frac{\sigma_x^2 + \sigma_y^2}{2} \pm \sigma_{xy} \cdot \sqrt{\eta^2 + 1}$$

The values of the MPC factor is given for the modes obtained from the analysis of the Bjørnafjorden Bridge concepts in Section 6.2.2.

6.2.2 Modal analysis of the Bjørnafjord Bridge concept K12

The analyses conducted below are based on a structural damping corresponding to a critical damping ratio of 0.5%. This is assumed to apply only for the dry part of the structure, i.e., for the system without hydrodynamic or aerodynamic contributions. Aerodynamic contributions to the system matrices are not included in the analysis generating the results provided below, as they are dependent on the mean wind velocity. The aerodynamic damping contributions have not been included.

The first horizontal modes have critical damping ratios are close to the predefined structural damping (0.5%). Because the potential damping is close to zero in the lowest frequency range, and the added mass has a non-zero contribution in the same range, the system critical damping ratios are

below the predefined structural damping of 0.5. For modes with damped natural frequency around 0.6rad/s, or, equivalently, damped natural period around 11 seconds, the potential damping contributions acting on the pontoons give a significant contribution to the systems’ damping ratios. The vertical modes are all highly damped due to the contribution from potential damping. Furthermore, they are very closely spaced in frequency.

The modal parameters for K12 are shown in Figure 6-2, and the mode shapes of the first ten modes depicted in Figure 6-3. Note that the values are based on the 06-iteration of the model, and some stiffness changes were included in the 07 revision. This has a small effect on the modal periods.

Figure 6-4 and Figure 6-5 depict the diagonality and complexity, respectively, corresponding to the first 30 mode shapes obtained from the modal analysis of K12. The figures reveal that the first 10 modes, predominately being horizontal modes, reasonably can be assumed to be uncoupled and real in their behaviour.

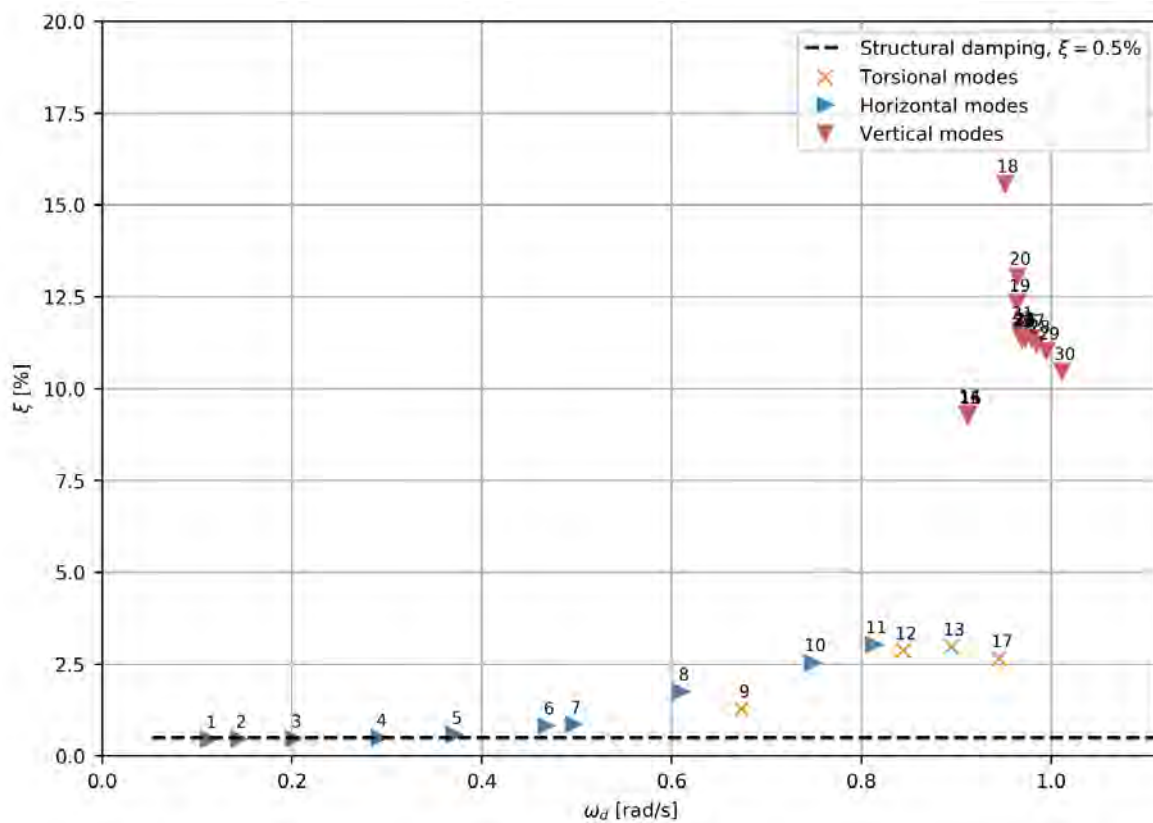


Figure 6-2. Critical damping ratios and damped natural frequencies of the first 30 modes of K12_07. The dominating mode types are denoted by different symbols.

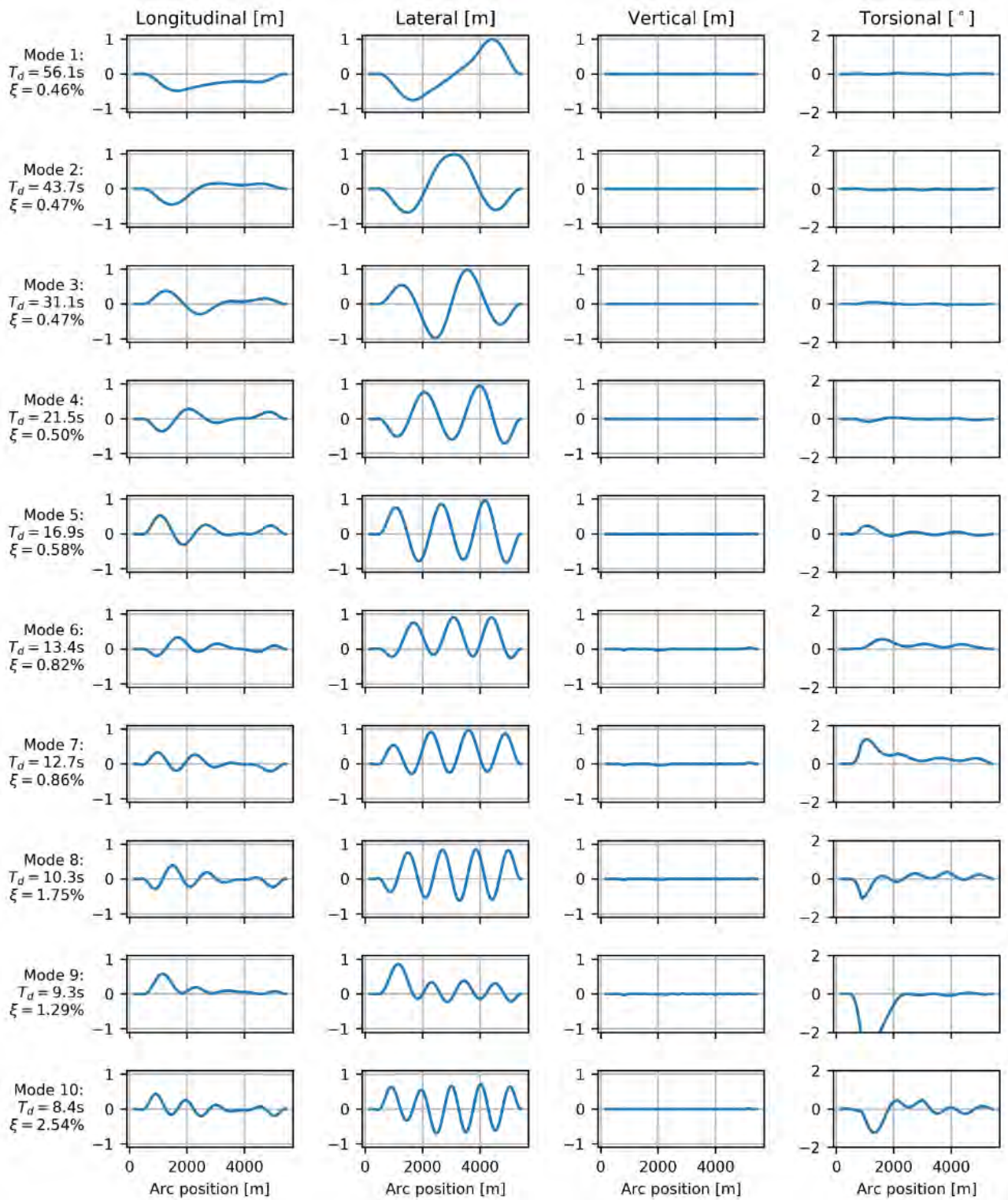


Figure 6-3. Mode shapes of the first ten modes of K12_07.

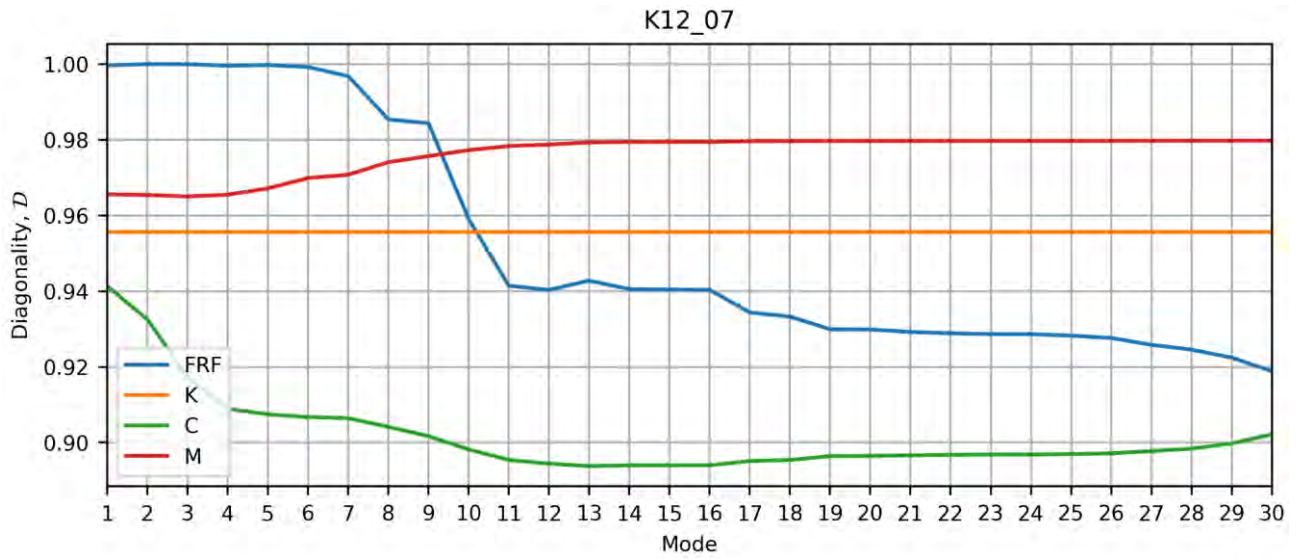


Figure 6-4. Diagonality measure \mathcal{D} for matrices corresponding to K12, from Equation 1. Modes 1 through 7 are highly diagonal, indicating low amount of coupling.

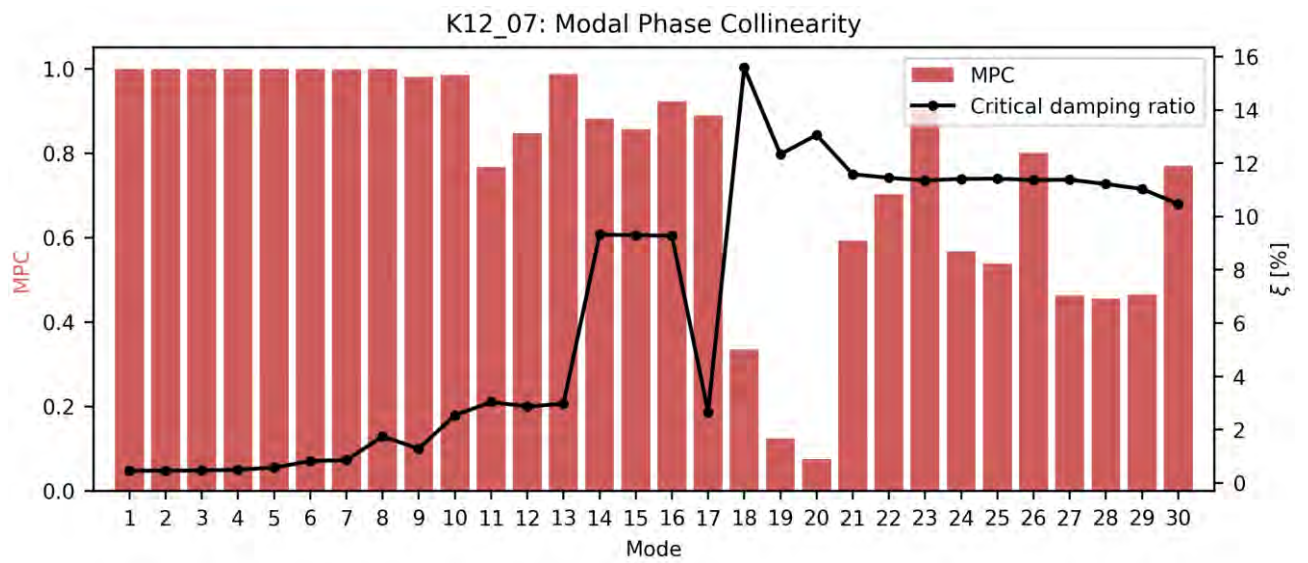


Figure 6-5. Modal phase collinearity (MPC) for modes of K12, from Equation 2. Modes 1 through 10 have small inter-phase differences.

7 Benchmark between softwares

7.1 Eigenmodes

Eigenmodes for the main dynamic simulation tools Novaframe and Orcaflex are given in the following. Overall, they match well in period and shape. Primary, the differences seen are due to a different methodology for normalising the modes. In Novaframe, the modes are normalised so that the maximum nodal displacement in the global X, Y and Z-direction is equal to 1. In Orcaflex, the modes are normalised so that the size of the maximum displacement vector is equal to 1.

In general, a very good agreement was found between the two softwares. The deviation between modes in the two software for K12 are within 3% for the first 38 modes, but in general significantly less.

Table 7-1 Comparison of modes for K12_07

Mode #	Period OrcaFlex [sec]	Period NovaFrame [sec]	Difference [%]	Mode #	Period OrcaFlex [sec]	Period NovaFrame [sec]	Difference [%]
1	56.3	56.4	0.3%	26	6.40	6.44	0.7%
2	43.2	44.1	2.0%	27	6.39	6.44	0.8%
3	31.0	31.4	1.0%	28	6.35	6.35	0.0%
4	21.4	21.7	1.3%	29	6.30	6.31	0.1%
5	17.1	17.1	0.4%	30	6.22	6.33	1.9%
6	13.4	13.8	2.3%	31	6.15	6.26	1.8%
7	12.7	12.9	1.2%	32	6.08	6.13	0.8%
8	10.3	10.4	1.4%	33	6.03	6.15	1.9%
9	9.48	9.58	1.0%	34	5.93	5.94	0.1%
10	8.36	8.54	2.1%	35	5.81	5.97	2.7%
11	7.39	7.50	1.4%	36	5.79	5.82	0.4%
12	7.06	7.19	1.8%	37	5.65	5.67	0.4%
13	6.89	6.98	1.2%	38	5.56	5.65	1.6%
14	6.89	6.85	-0.5%	39	5.35	5.53	3.3%
15	6.88	6.82	-0.8%	40	5.28	5.39	2.0%
16	6.85	6.79	-1.0%	41	5.21	5.38	3.0%
17	6.61	6.74	2.0%	42	5.13	5.26	2.3%
18	6.53	6.59	0.9%	43	5.07	5.09	0.4%
19	6.48	6.60	1.8%	44	4.92	5.03	2.2%
20	6.47	6.51	0.7%	45	4.75	4.74	-0.2%
21	6.46	6.48	0.3%	46	4.73	4.79	1.3%
22	6.46	6.53	1.1%	47	4.61	4.64	0.7%
23	6.46	6.46	0.1%	48	4.46	4.70	5.0%
24	6.44	6.46	0.4%	49	4.45	4.44	-0.3%
25	6.43	6.46	0.4%	50	4.31	4.48	3.6%

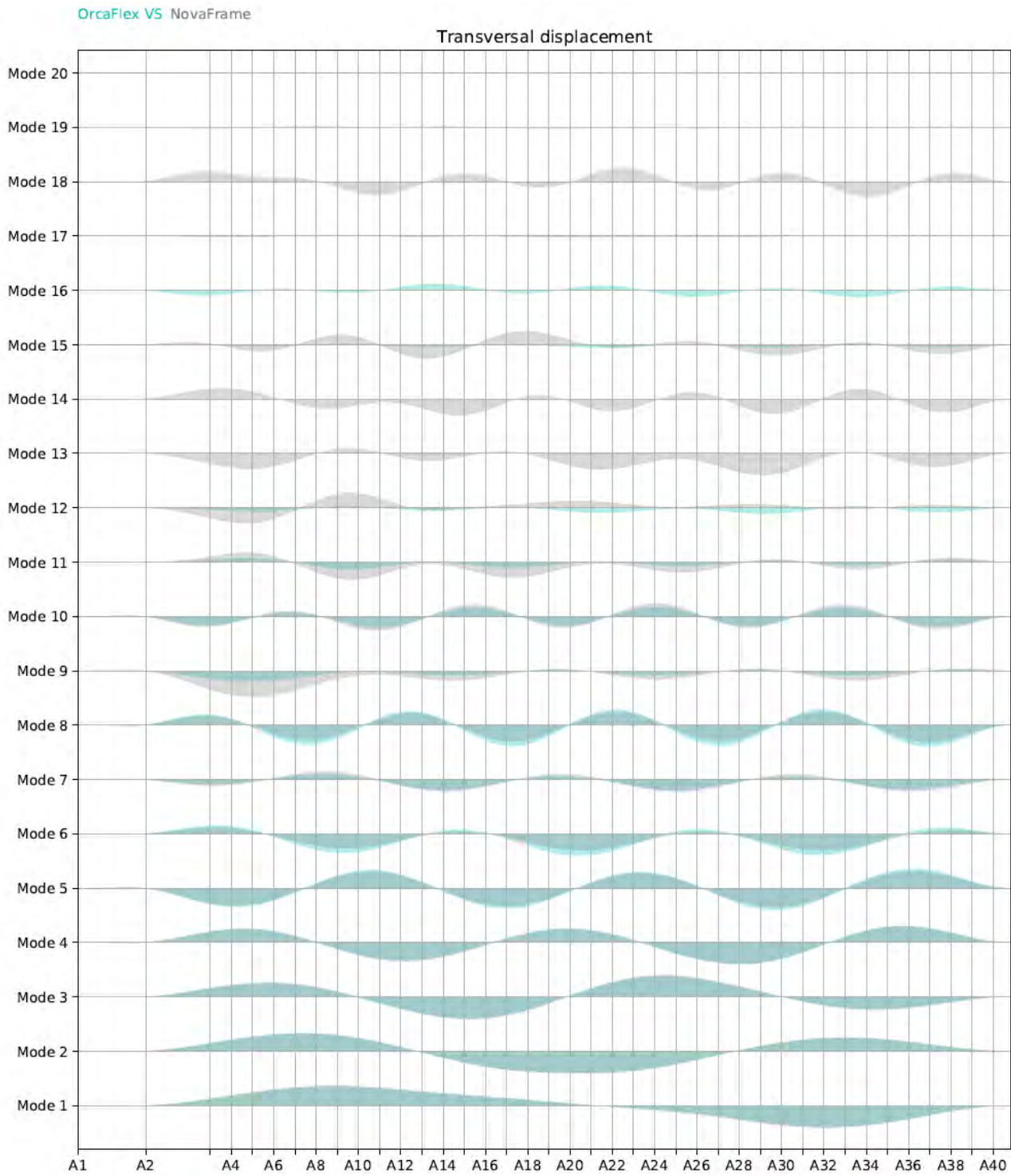


Figure 7-1 Transverse eigenmodes for K12_07

7.2 Comparison of static response

The simulated response in Novaframe, RM-Bridge and Orcaflex were compared for some defined load cases; permanent loads (self-weight and tensioning) in high bridge, transverse shear loads, temperature deformation and torsional load (around bridge girder axis).

The differences between the static results from Novaframe and Orcaflex are generally small, as is the case with other static loading conditions. The difference is generally small for most of the force and moment components, with the largest difference seen in weak axis moment and vertical shear force. The discrepancy between the results from Novaframe and Orcaflex is due to the varying geometric stiffness that is accounted for in the time domain analyses in Orcaflex, but not in the frequency domain analysis of Novaframe.

A few issues cause differences between the softwares:

- Nonlinear effects are included in Orcaflex, but not included in Novaframe or RM-bridge.
- Shear deformation is included in the beam formulation in RM-bridge but not Orcaflex or Novaframe
- Compression in the bridge girder due to the cable-stay tension are corrected for in RM-Bridge but not in Orcaflex. Hence, bridge compression will cause a global response in Orcaflex.
- Mooring lines are modelled in their planned slightly asymmetric conditions in Orcaflex but with an idealized spring in the other softwares. This cause some bridge girder responses both for permanent and variable loads.

Considering the above issues and the magnitude of the response to permanent loads and other load components are considered acceptable.

Note that for load combinations used for design (in [19]) the response to all static loads are taken from the RM-bridge model that gives the most accurate response estimation. The Orcaflex and Novaframe models are shown below as a means of benchmark of model behavior, and the initialization of especially the permanent load is included in these softwares so that the response to environmental loads include an adequate initial configuration of the bridge to include second-order effects on the environmental loading. All of the static response plots are generated from model K12_07.

7.2.1 Permanent loads

The permanent loads comprise of self-weight and tensioning of cables. Only the main bridge is plotted with a few selected responses in Figure 7-2 to Figure 7-6. Permanent loads are in general well represented between the softwares and e.g. axial forces are similar, but some deviation was found especially for the Orcaflex model. This is likely due to initialization of the model with a split between the high bridge and the floating bridge in which compression of the bridge girder due to cable tension is not corrected for. The effect is clearly seen in the figures, e.g. for torsional response, but has no practical consequence for the response estimation. The differences in strong-axis moment between the solvers, 150 MNm, are small when compared to the capacity and utilization of 2-3000 MNm.

Orcaflex and Novaframe does not account for the compression of the bridge girder when the stay-cables are tensioned, and consequently shows a different weak-axis moment behaviour in the backspan of the cable-stayed bridge as compared to RM-bridge. RM fully compensate for this, and as a result have good control of the vertical deflection between the backspan columns and thereby the weak-axis bending moment.

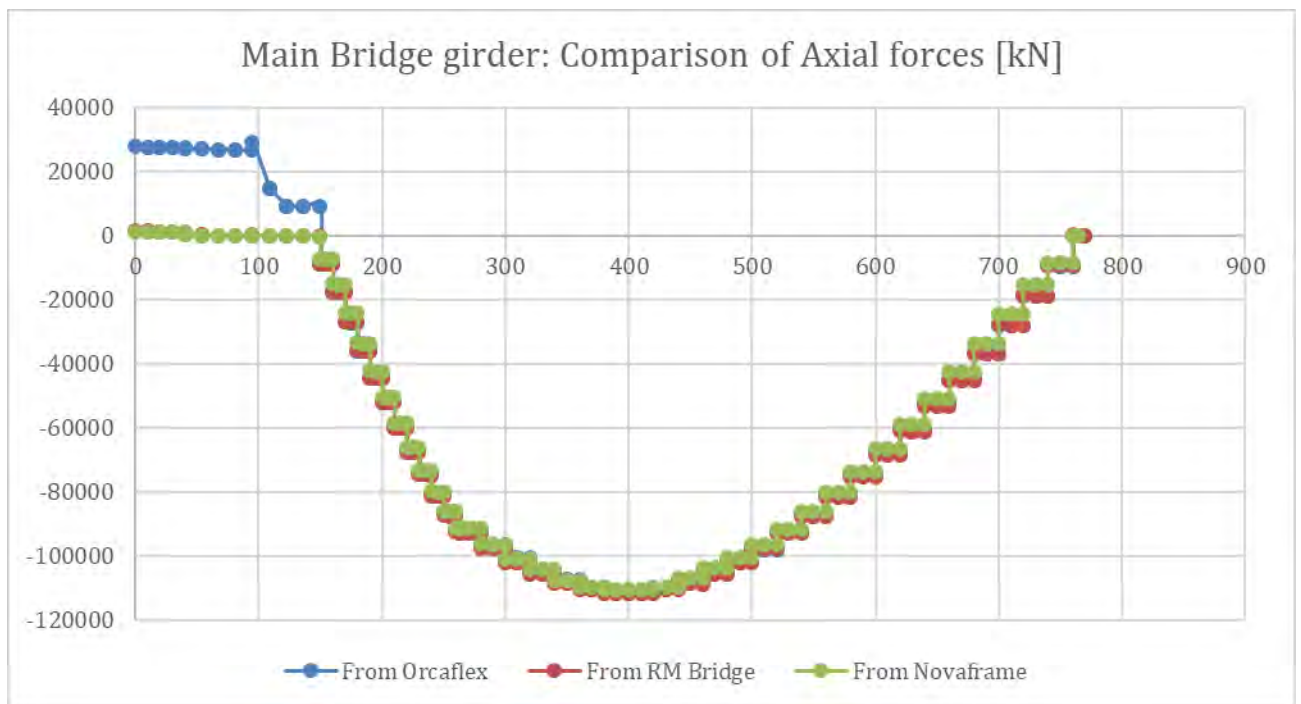


Figure 7-2 Comparison of axial forces in main bridge for permanent loads for K12 in kN

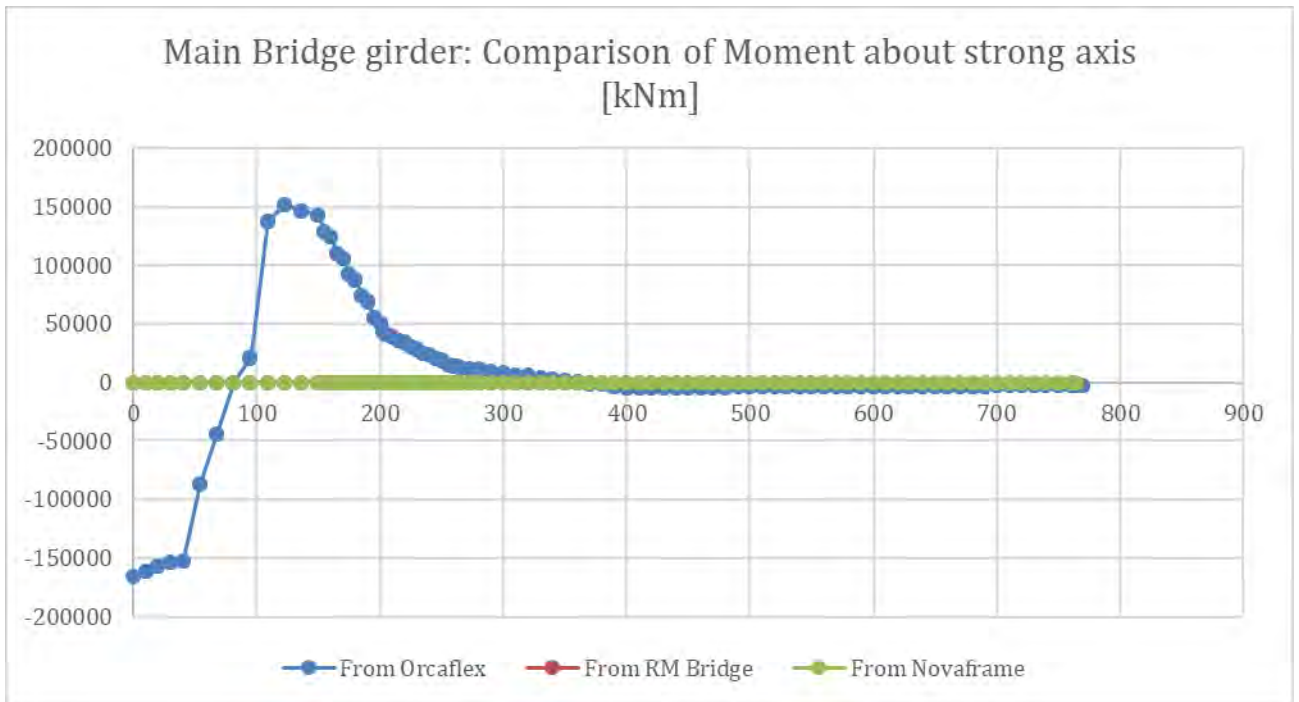


Figure 7-3 Comparison of moment about strong axis in main bridge for permanent loads for K12 in kNm

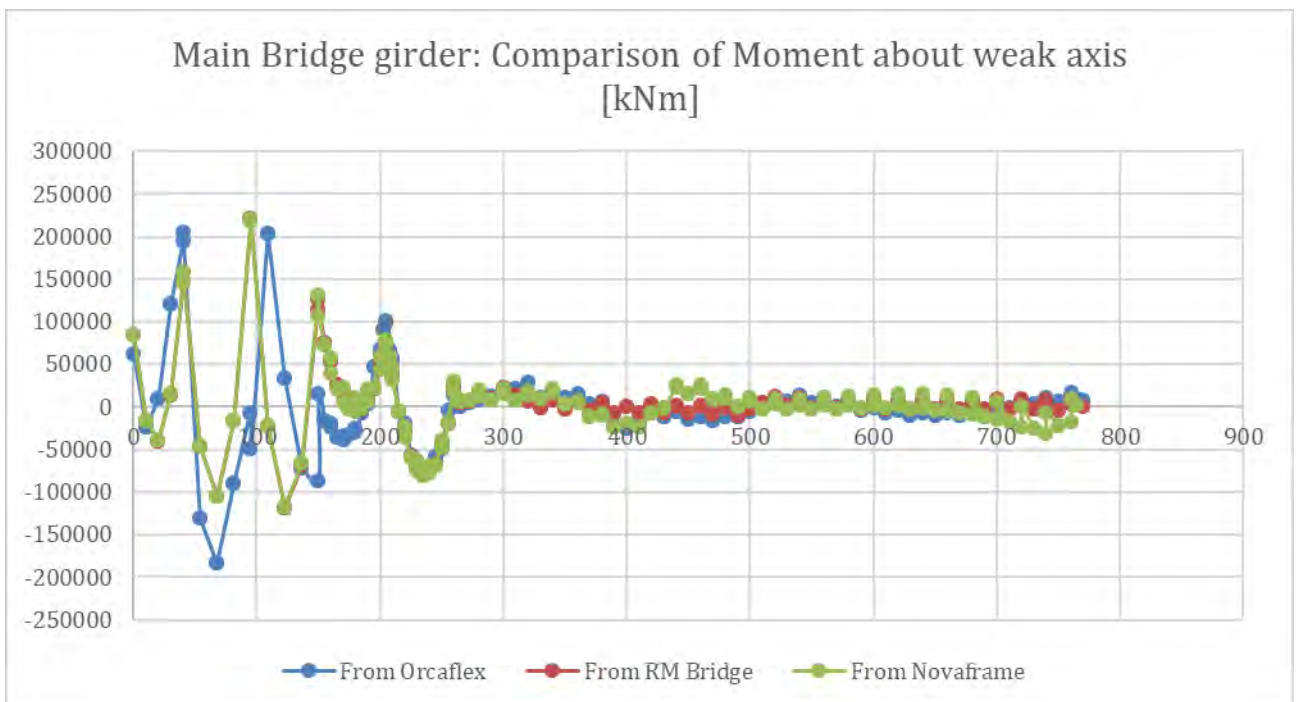


Figure 7-4 Comparison of moment about weak axis in main bridge for permanent loads for K12 in kNm

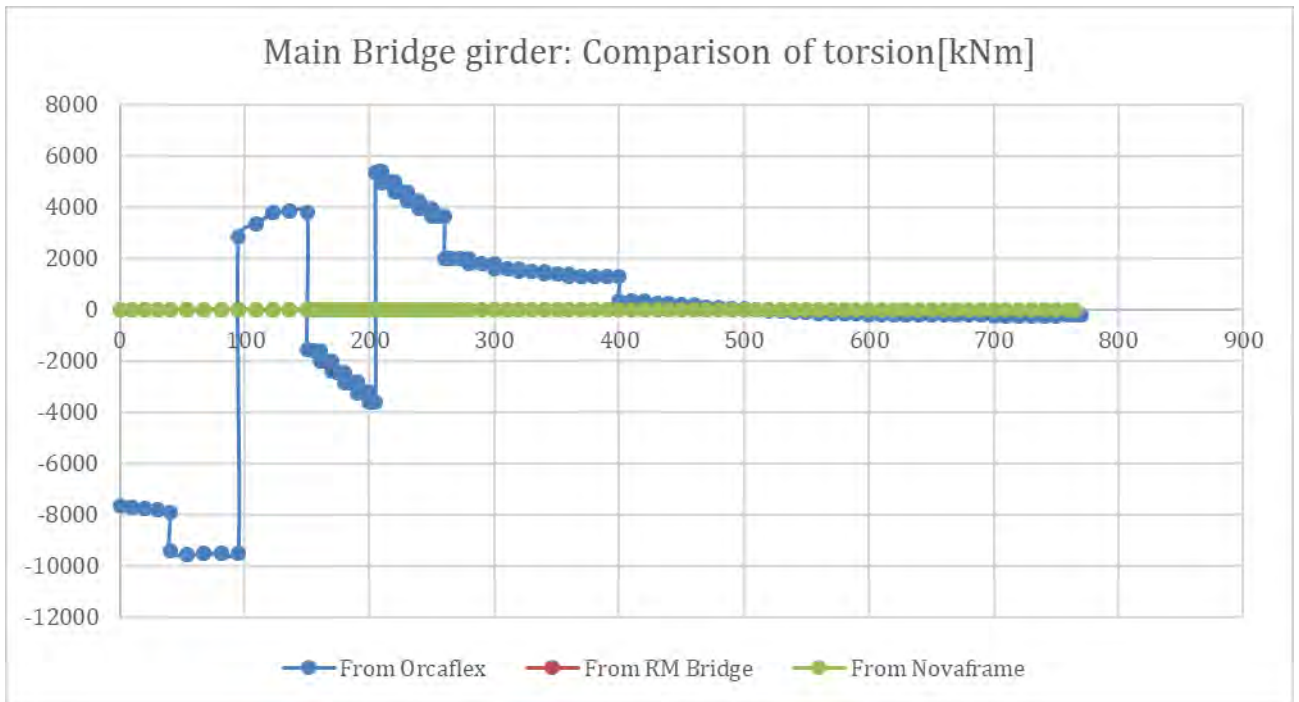


Figure 7-5 Comparison of torsion in main bridge for permanent loads for K12 in kNm

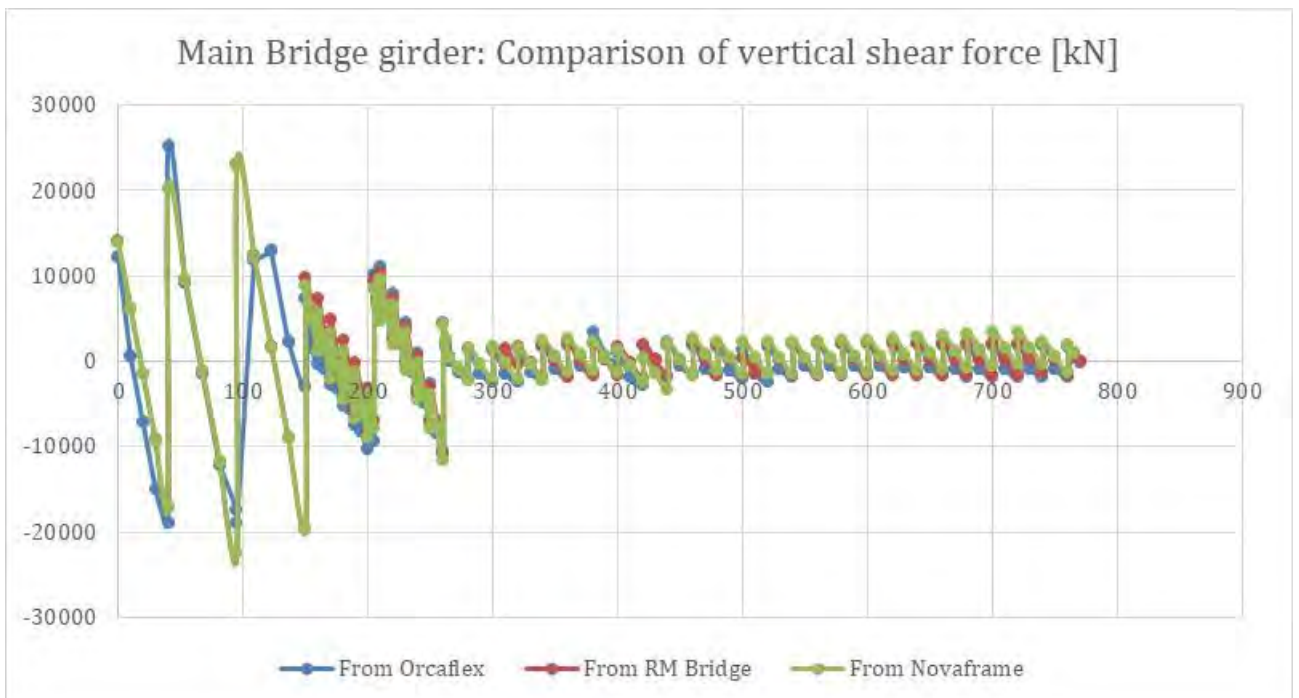


Figure 7-6 Comparison of vertical shear force in main bridge for permanent loads for K12 in kN

7.2.2 Transverse load

The transverse load comprises of a 1kN/m loaded perpendicular to the bridge axis. Selected results are compared in Figure 7-7 to Figure 7-10 . Forces and moments are very similar between the softwares, especially the transverse shear force and strong-axis moment. Minor differences are seen for axial force and torsional moment.

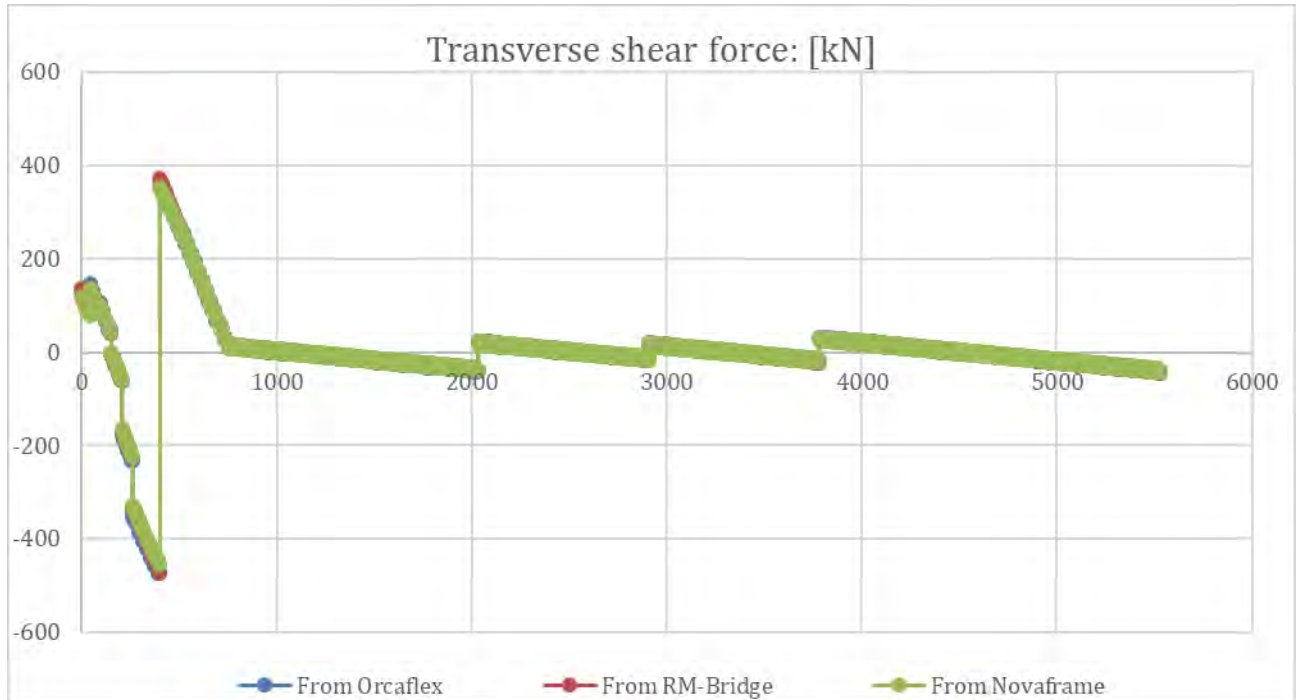


Figure 7-7 Comparison of transverse shear force for transverse load for K12 in kNm

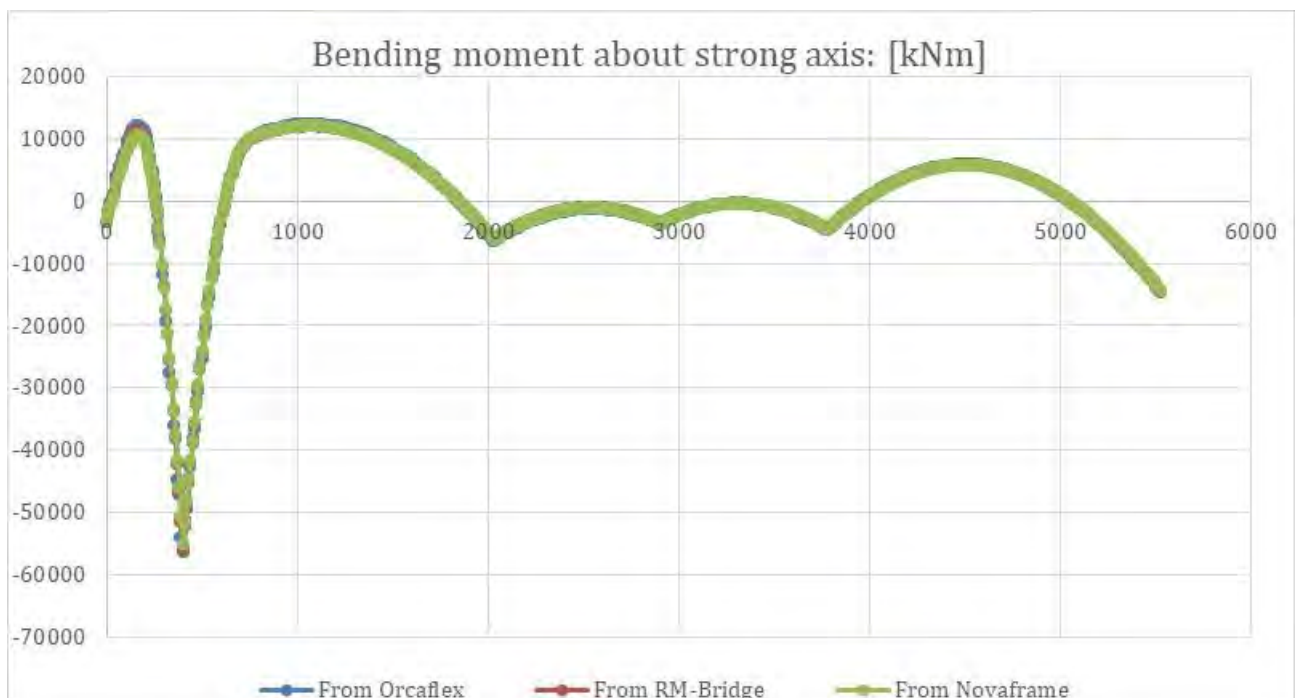


Figure 7-8 Comparison of bending moment about strong axis for transverse load for K12 in kNm

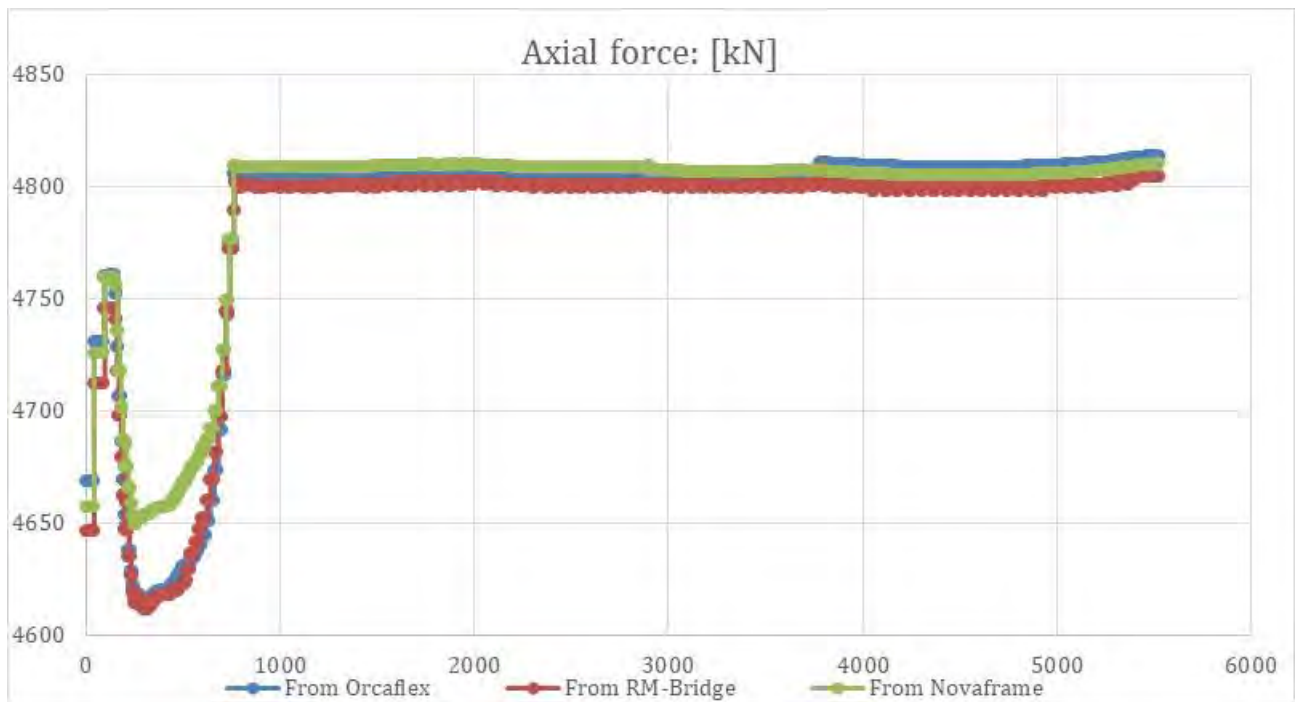


Figure 7-9 Comparison of axial force for transverse load for K12 in kN



Figure 7-10 Comparison of torsional moment for transverse load for K12 in kNm

7.2.3 Torsional load

The torsional load response shown in Figure 7-11 to Figure 7-14 show good agreement between the softwares, especially for torsional moment. Minor differences are seen for the other response types, but the amplitude of response is small.



Figure 7-11 Comparison of torsional moment for torsional load for K12 in kNm

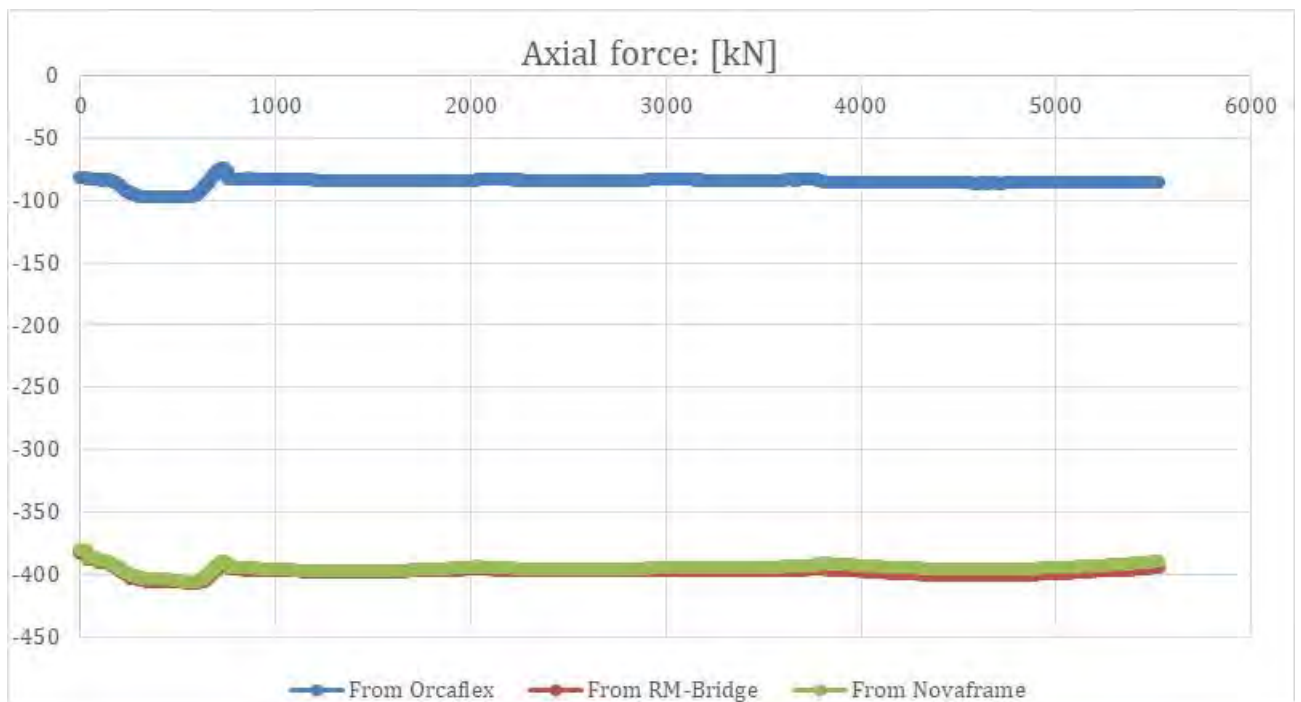


Figure 7-12 Comparison of axial force for torsional load for K12 in kN



Figure 7-13 Bending moment about strong axis for torsional load for K12 in kNm

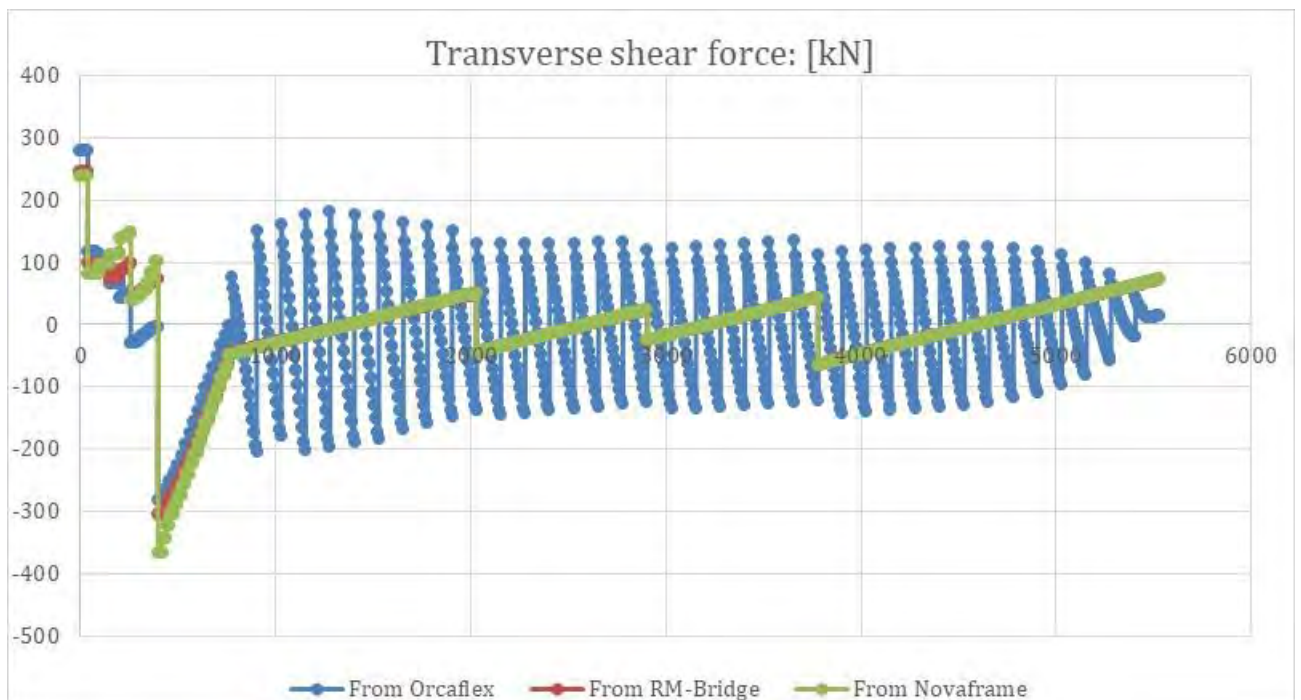


Figure 7-14 Transverse shear force for torsional load for K12 in kN

7.2.4 Temperature load

The temperature load is applied as a constant temperature increase of 30 degrees. Figure 7-15 to Figure 7-18 compares the response between the models, showing good agreement except for minor differences in the torsional moment.

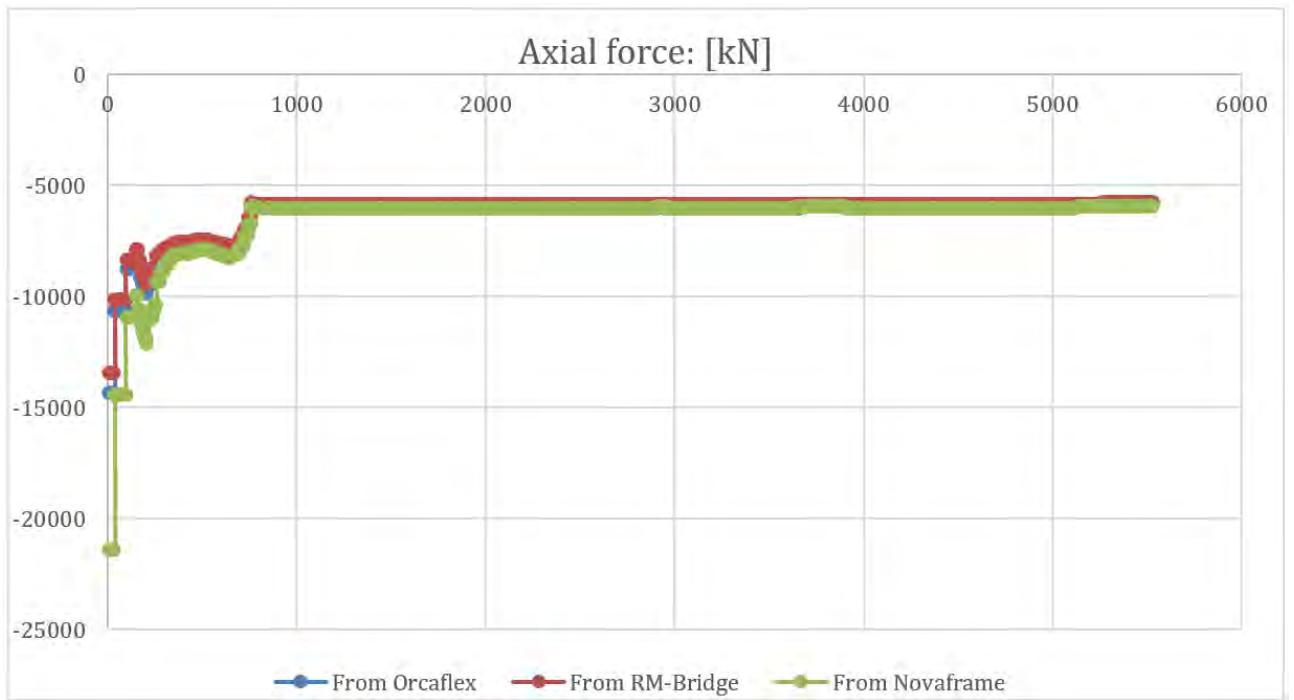


Figure 7-15 Axial force for temperature load for K12 in kN

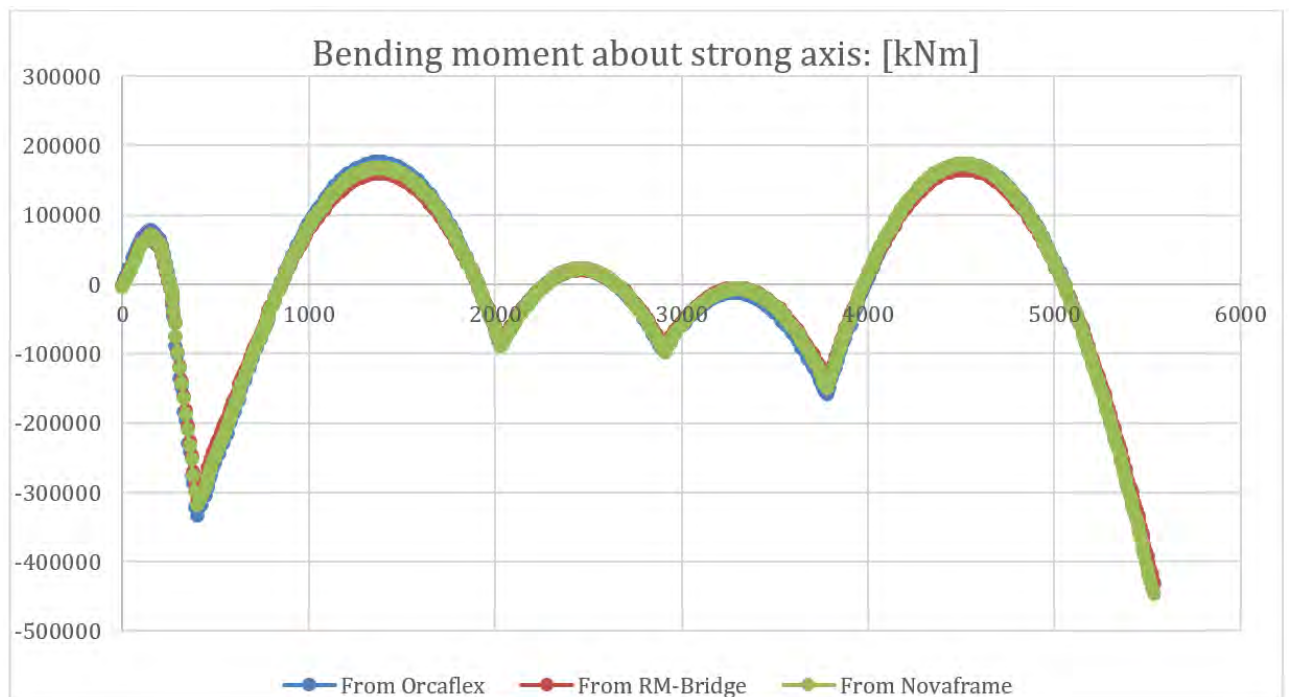


Figure 7-16 Comparison of bending moment about strong axis for temperature load for K12 in kNm

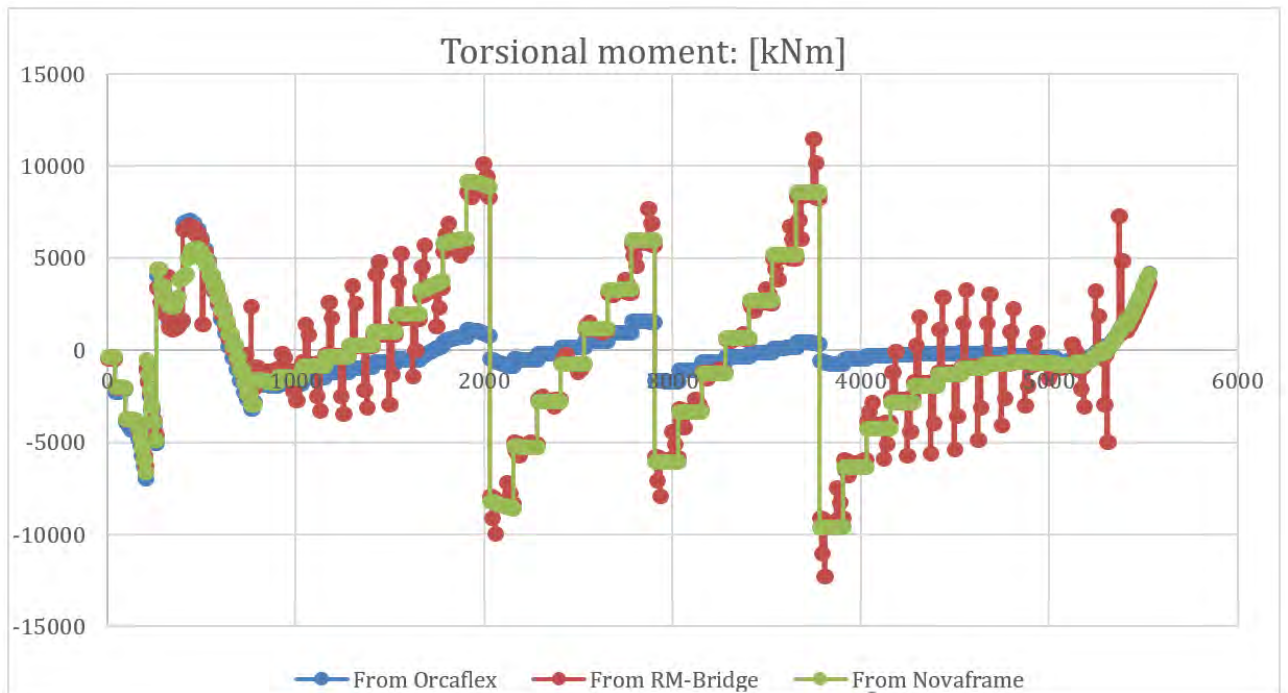


Figure 7-17 Comparison of torsional moment for temperature load for K12 in kNm



Figure 7-18 Comparison of transverse shear force for temperature load for K12 in kN

7.3 Comparison of wind response

The resulting forces and moments from static and dynamic wind analyses are compared between Novaframe and Orcaflex. The static results from Orcaflex are taken as the mean results from a wind time series subtracted by the permanent forces from a static analysis. The static wind results for Novaframe are obtained for the model with added geometric stiffness from mean wind and tensioning of cables.

For the dynamic analysis, the standard deviation of the resulting forces and moments are compared.

- The wind spectrum is treated differently between the programs; orcaflex through windsim evaluates the spectrum over the entire bridge whereas novaframe evaluates at only one point.
- Linear stiffness updates are included in orcaflex, so that the bridge direction towards the wind direction is updated in both yaw and roll. Novaframe considers a static configuration of the bridge. This is a source of discrepancy in the results.
- Full nonlinear geometric stiffness is accounted for in Orcaflex by default whereas Novaframe has the option to either have a linear stiffness or perform a single stiffness update due to static deflection upon which the dynamic response is evaluated. Nonlinear geometric effects are of increasing importance with increasing deformation.
- Modal damping is accounted for directly in Orcaflex, whereas Novaframe require an assimilation of the various damping sources.

Note that the comparison was performed for the 06-iteration of the K12 model.

7.3.1 Input parameters

Wind response is checked with a basis wind speed at 21.4m/s towards 80°, as can be seen in Figure 7-19. The worst drag, moment and lift coefficient between -2° and 2° are used.

Basis wind speed (at height 10m) = 21.4m/s

Wind direction = 260°

Uncertainty angle = 2°

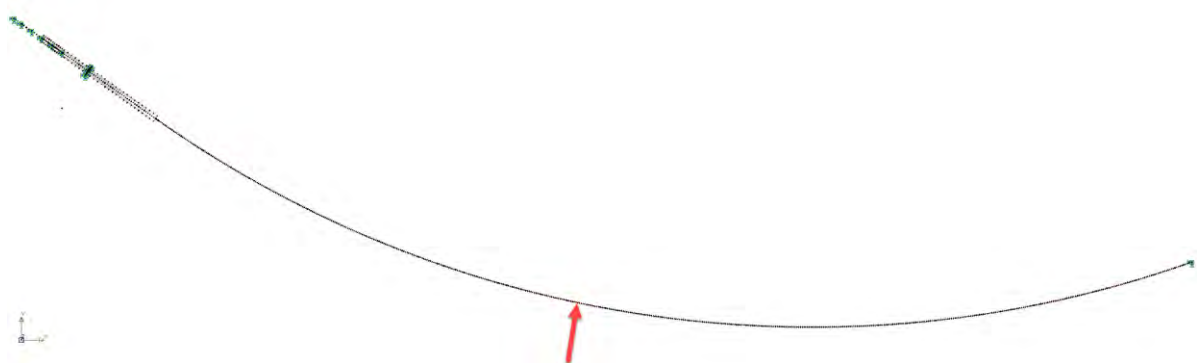


Figure 7-19 Top down view of bridge displaying the angle of the incoming wind

The tested dynamic N400 wind parameters are given in Table 7-2. The wind series in Orcaflex is generated by Windsim and is varying over the entire height of the structure. The loads in Novaframe are based upon the wind spectral parameters derived at a height of 50 meters. Two sets of wind parameter input were evaluated for the Orcaflex models, termed C1 and C2.

Table 7-2: Spectral parameters for dynamic wind analysis of K12_06

Parameter	Z=50m Novaframe	Z=10m Orcaflex C1	Z=10m Orcaflex C2
xLu	162.1	100	100
xLv	40.5	25	25
xLw	13.5	8.3	8.3
Au	6.8	6.8	6.8
Av	9.4	9.4	9.4
Aw	9.4	9.4	9.4
Cux	10.0	10.0	3
Cuy	10.0	10.0	10.0
Cuz	10.0	10.0	10.0
Cvx	10.0	10.0	6.0
Cvy	6.5	6.5	6.5
Cvz	6.5	6.5	6.5
Cwx	10.0	10.0	3.0
Cwy	6.5	6.5	6.5
Cwz	3.0	6.5	3.0

7.3.2 Static wind response

Plots of the resulting force components are given in Figure 7-20 to Figure 7-23. The forces and moments are plotted versus the arclength of the bridge and generally shows acceptable agreement between the programs when considering the differences in methodology.

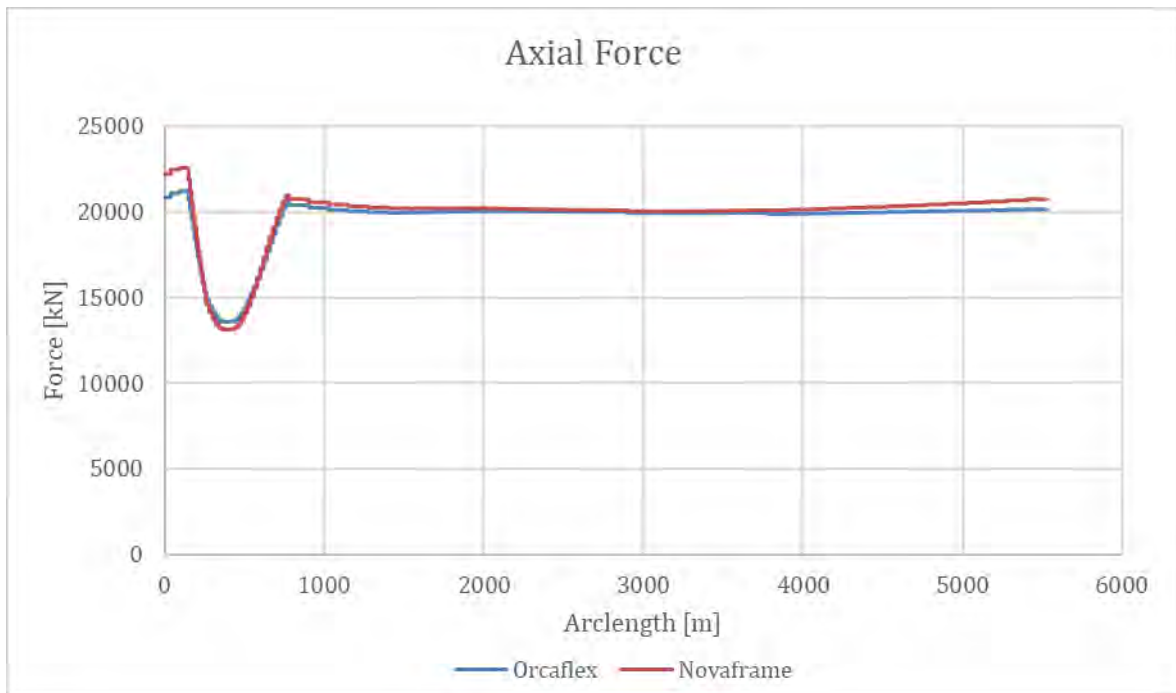


Figure 7-20: Comparison of static axial force in kN

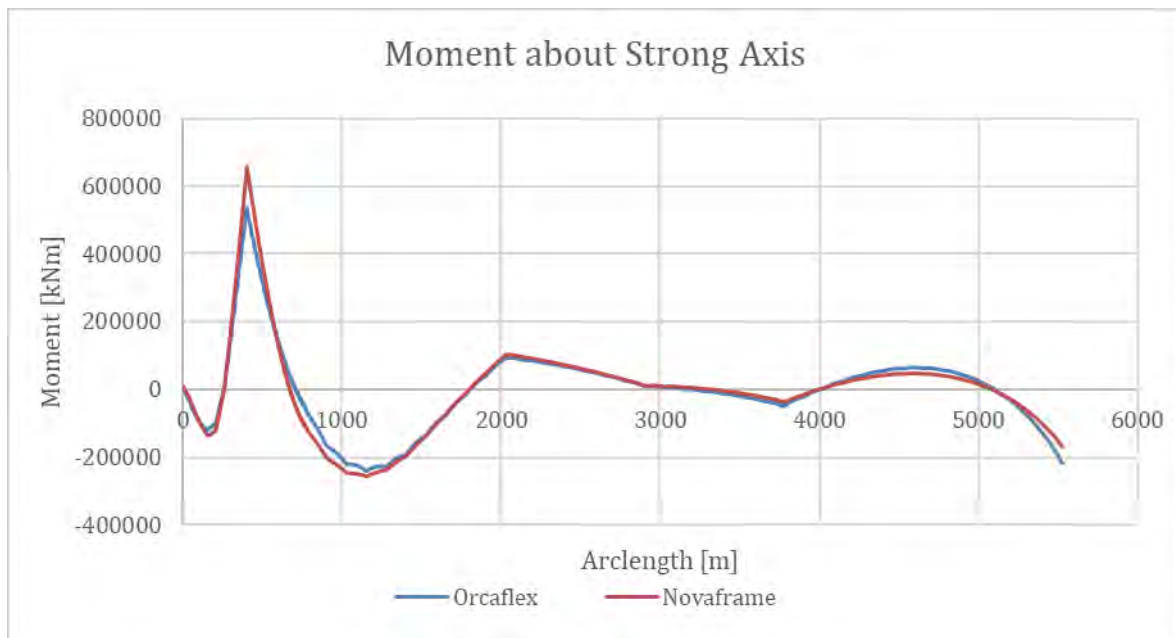


Figure 7-21: Comparison of moment about strong axis in kNm

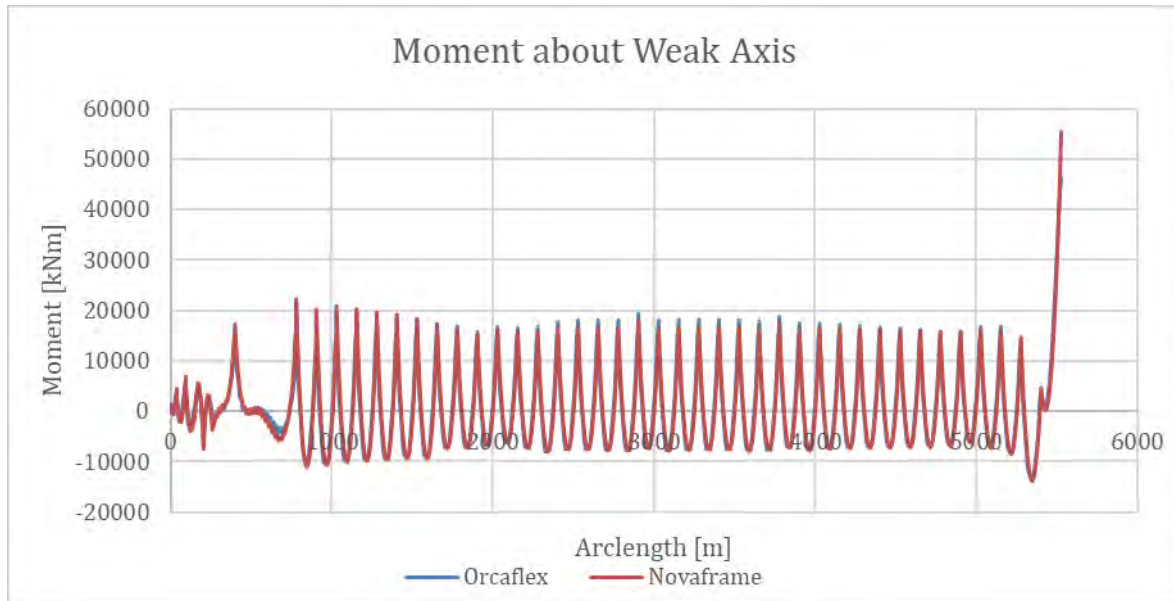


Figure 7-22: Comparison of moment about weak axis in kNm

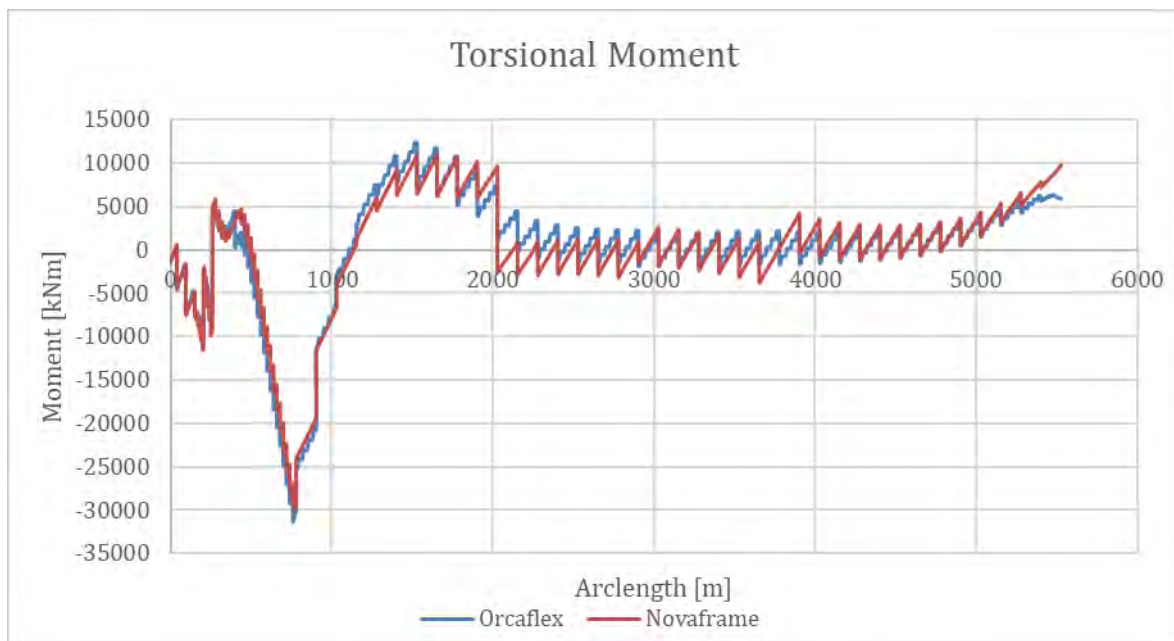


Figure 7-23: Comparison of torsional moment in kNm

7.3.3 Dynamic wind results

The resulting standard deviations of the forces for are plotted in the following. The difference between the dynamic results are larger than the between the static results. This is in large part due to a varying geometric stiffness in the nonlinear analysis. The largest differences are found for the weak axis moment and the vertical shear force. The difference is relatively larger for weak axis moment and shear force because of the relatively smaller stiffness in the vertical direction than in the transverse direction.

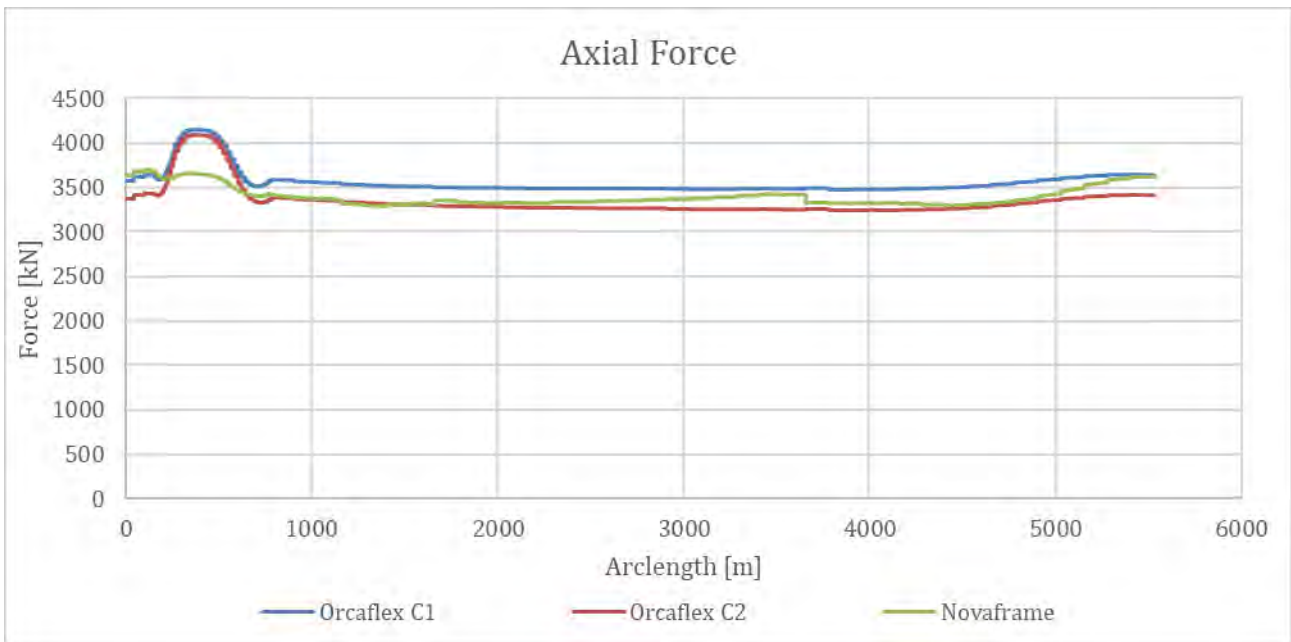


Figure 7-24: Comparison of axial force STD in kN

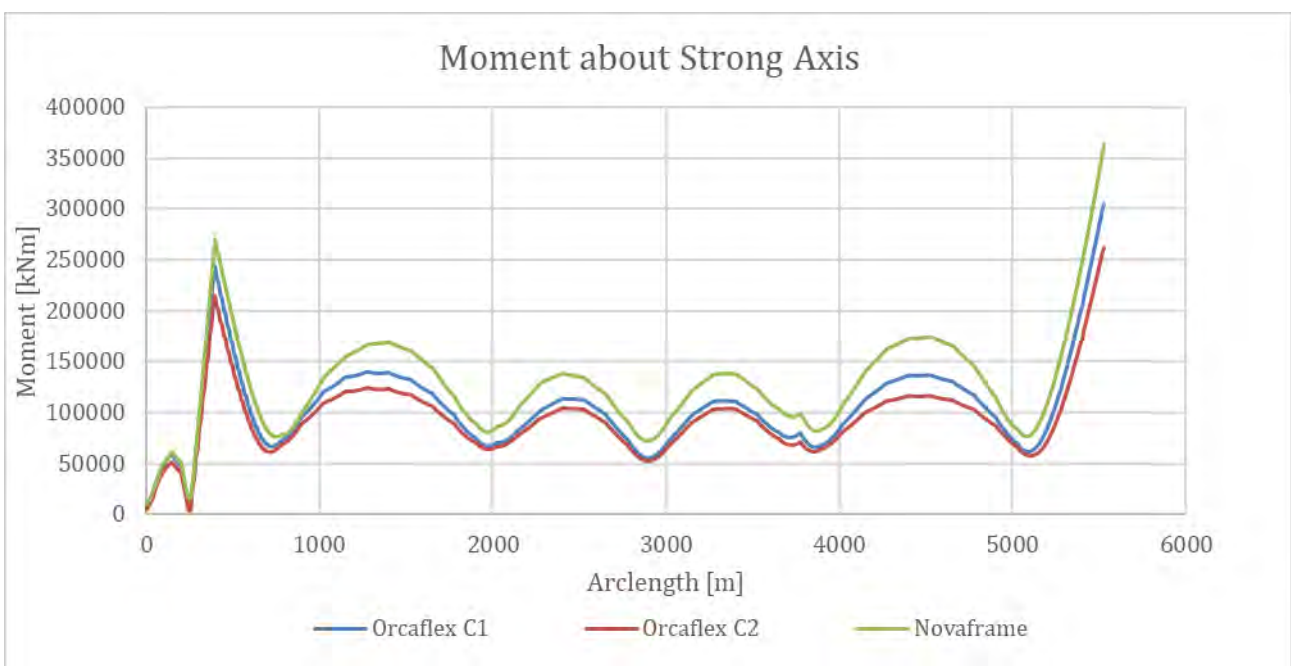


Figure 7-25: Comparison of strong axis moment STD in kNm

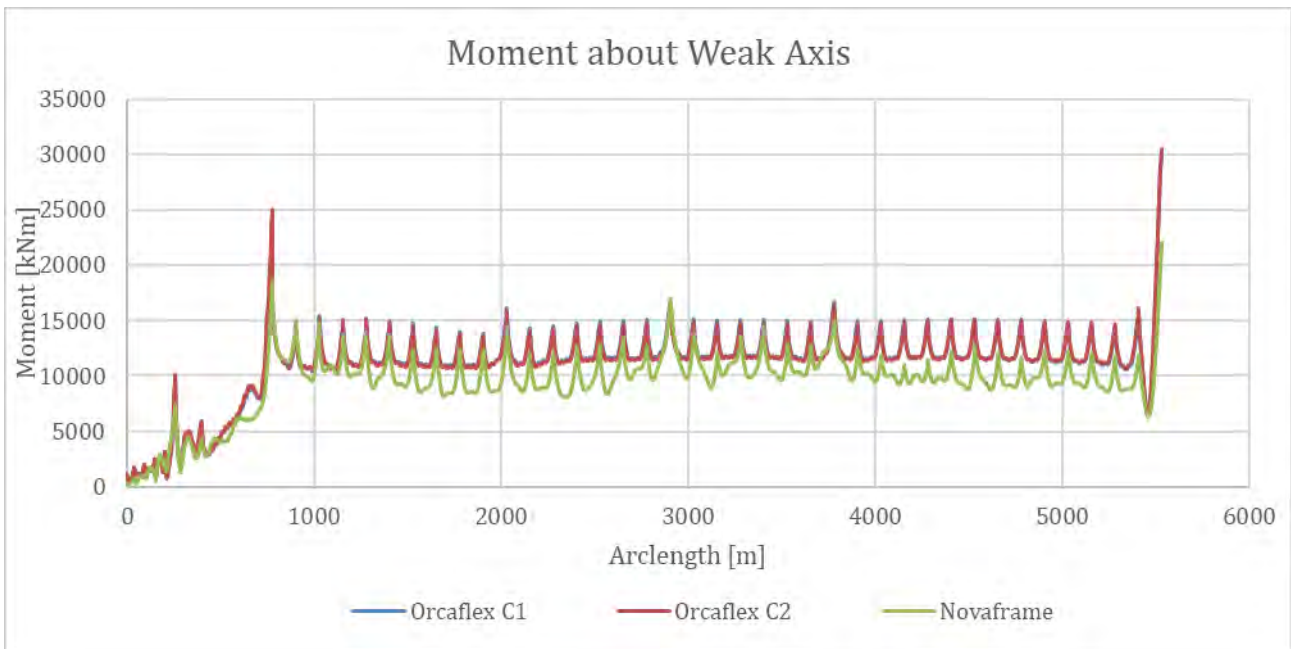


Figure 7-26: Comparison of weak axis moment STD in kNm

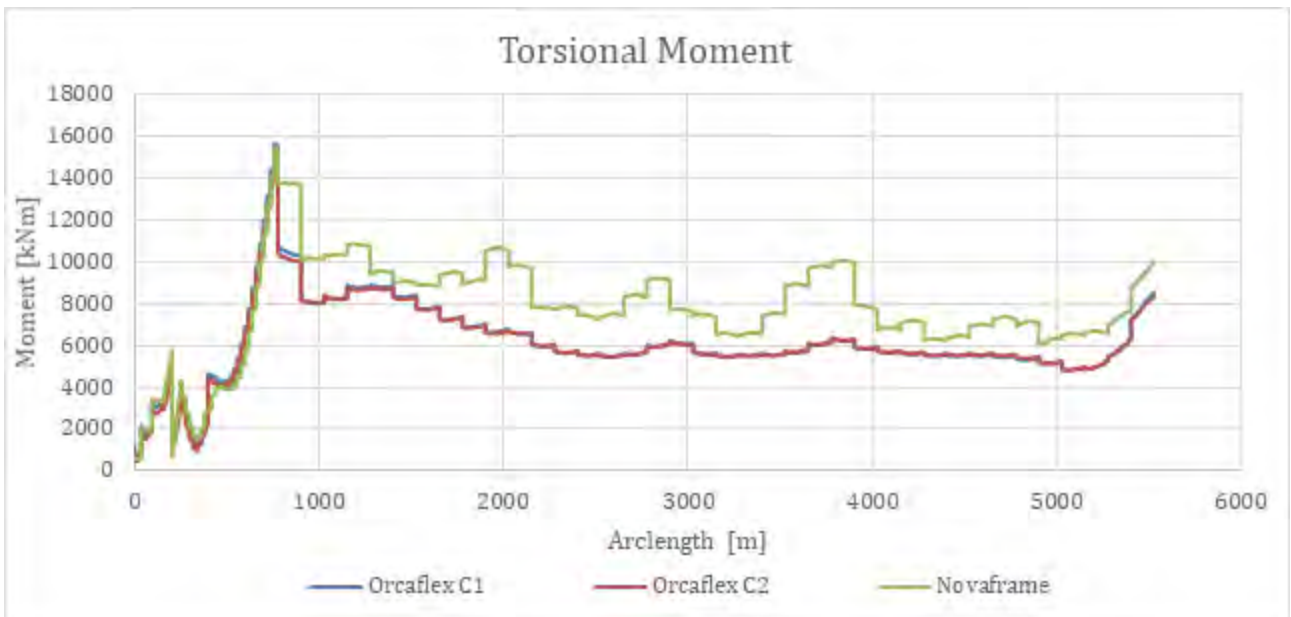


Figure 7-27: Comparison of torsional moment STD in kNm

7.3.4 Discussion

The findings show a generally good agreement between Novaframe and Orcaflex for wind response when considering the differences in how nonlinear geometric stiffness is accounted for and the differences in wind spectrum input. Hence, the use of Novaframe as a supplement to Orcaflex for wind-response in the fatigue calculations will yield acceptable results. Note that dynamic wind was not found to be governing for fatigue design, see Appendix I [20].

8 Numerical modelling aspects

Several aspects of the numerical representation of the bridge model have been studied in depth to reduce uncertainties regarding the models' ability to accurately predict the response of the bridge to external loads. Both frequency domain and time domain analysis have been investigated and compared.

8.1 Method

The first step is to check simulation time duration, simulation ramp-up and simulation time step. It is assumed that checks of simulation time parameters are independent of checks of spectrum parameters. Using the estimated simulation time parameters from the first step, step two is to check the number of directions necessary to capture the response of the bridge due to directional spread and the number of components per direction necessary for convergence. First, the spectrum parameter check is done using a native orcaflex discretization method. This method is then used as a benchmark to check a newly developed discretization method against. The check of directional spread and number of components are then checked for frequency domain analysis. The next step is to check seed variability. Finally, we compare frequency domain results against time domain results.

8.2 Conclusion

- 3600 seconds simulation time is enough to achieve sufficiently low statistical variance between seeds. More details are found in section 8.3.
- 300 seconds ramping period is enough to avoid that transient behavior affect the predicted response for bridge concepts K12-K14. More details are found in section 8.4.
- 0.2 seconds time step is sufficiently low to achieve convergence. More details are found in section 8.5.
- 600 wave components divided between 15 wave directions is enough to capture the physics in time domain analysis. In time domain all 600 wave components have unique frequencies.
- Preliminary analysis indicates that the number of wave components necessary to capture the physics in time domain analysis can be reduced by 75% (150 components divided between 15 directions) if the wave spectrum is discretized with a refined method where the distribution of wave frequencies is concentrated in important frequency ranges. More details are found in section 8.6.
- 2250 wave components divided between 15 wave directions is enough to capture the physics in frequency domain analysis with less than 1.5% error. In frequency domain the 2250 components are divided in 15 directional sets of 150 components with unique frequencies. However, the number of wave components could be increased to about 500 reducing the error to below 0.1% without increasing the computation time too much. More details are found in section 8.9.
- 10 seeds are enough to achieve 96% convergence of the predicted standard deviation of the response with 90% certainty. More details are found in section 8.8.
- Frequency domain analysis and time domain analysis show corresponding results.

8.3 Time duration

The dynamic convergence of the model has been studied by simulating one seed of each of the conditions tabulated below.

Table 8-1: Environmental parameters in time domain study

Parameter	Wind sea	Swell	Wind
Wave Type	JONSWAP	JONSWAP	
Wave Hs	2.1	0.34	
Wave Tp	5.5	13.5	
Wave Gamma	2.3	5.0	
Wave Direction	75	300	
Spreading exponent	8	10	
Wind Direction			100
Wind Speed			22.5

Table 8-2: Simulation parameters in time duration study

Parameter	Wind sea	Swell	Wind
Time step	0.2	0.2	0.2
Duration	10800	21600	21600
Ramping period	300	300	300
Number of directions	15	15	15
Components per direction	40	40	40
Number of seeds	1	1	1

The results have been extracted in bridge axis 2 (at the tower). Rolling (moving) mean and standard deviation with different statistical windows (60 s, 600 s, 3600 s, 10800 s) have then been plotted in order to observe the evolution of the statistical process during the time duration. In addition, the coefficient of variation (CV) of each window has been calculated. The coefficient of variation is defined as the standard deviation σ divided by the mean μ .

$$CV_{\text{rolling mean}} = \frac{\sigma_{\text{rolling mean}}}{\mu_{\text{rolling mean}}}, CV_{\text{rolling std}} = \frac{\sigma_{\text{rolling std}}}{\mu_{\text{rolling std}}}$$

The rolling mean and standard deviation decreases with larger statistical windows. The statistical variation will therefore typically be smaller between several longer simulations, and higher between several shorter simulations. Therefore, it may be necessary to simulate more seeds if the duration is short.

The rolling mean and standard deviation are stationary processes, meaning that the dynamic processes in the simulation are stable even at the very beginning of the simulation. A simulation of 3600 seconds is therefore long enough to meet a stable condition and to keep statistical variation between seeds to a low level.

8.3.1 Axial force

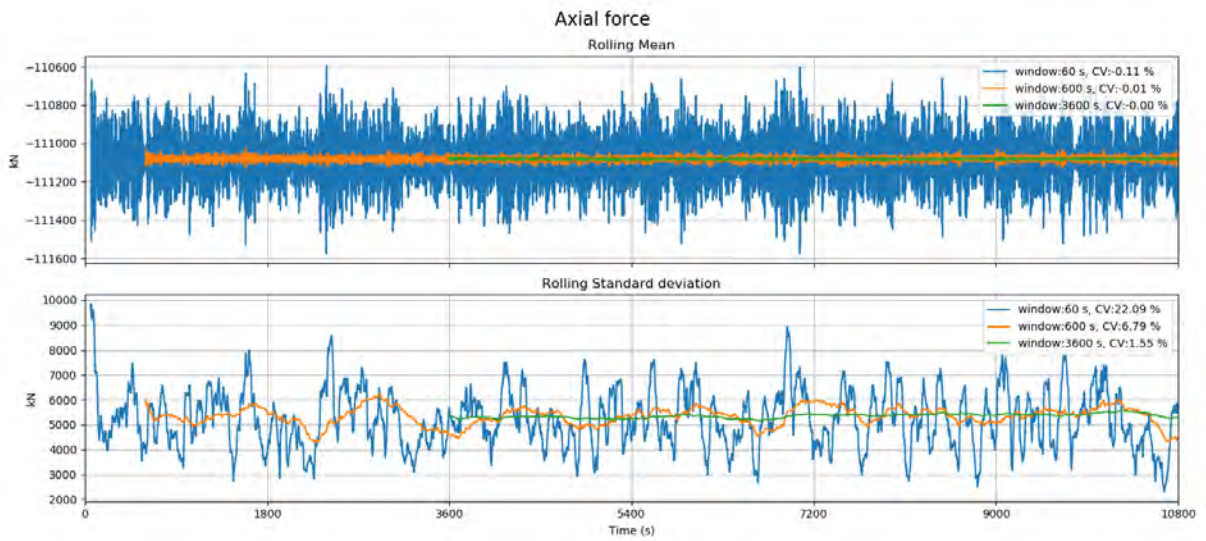


Figure 8-1: Wind sea, axial force

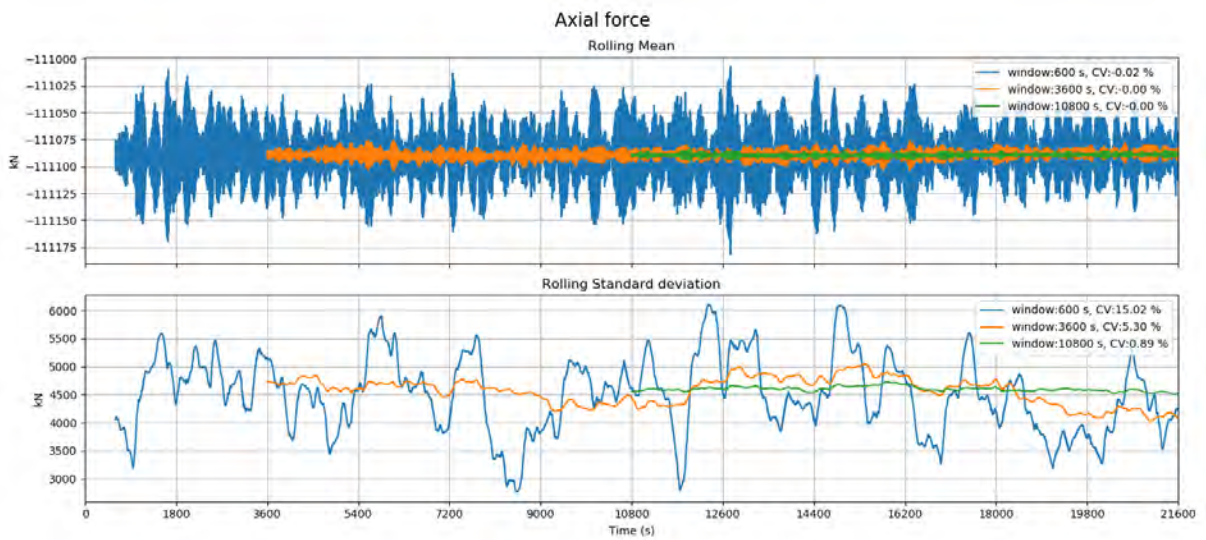


Figure 8-2: Swell sea, axial force

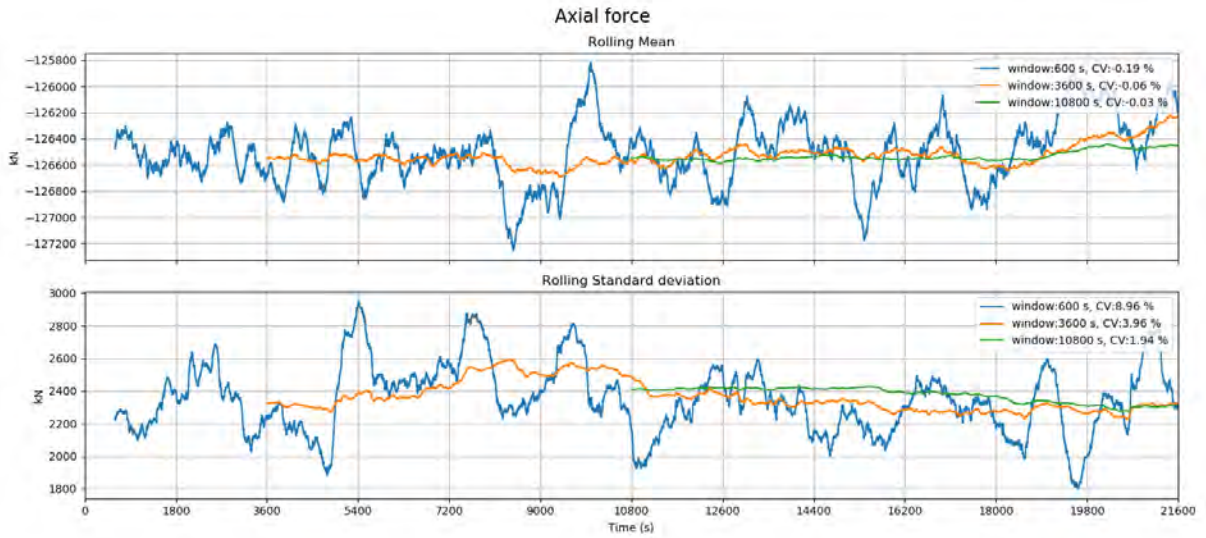


Figure 8-3: Wind, axial force

8.3.2 Weak axis bending moment

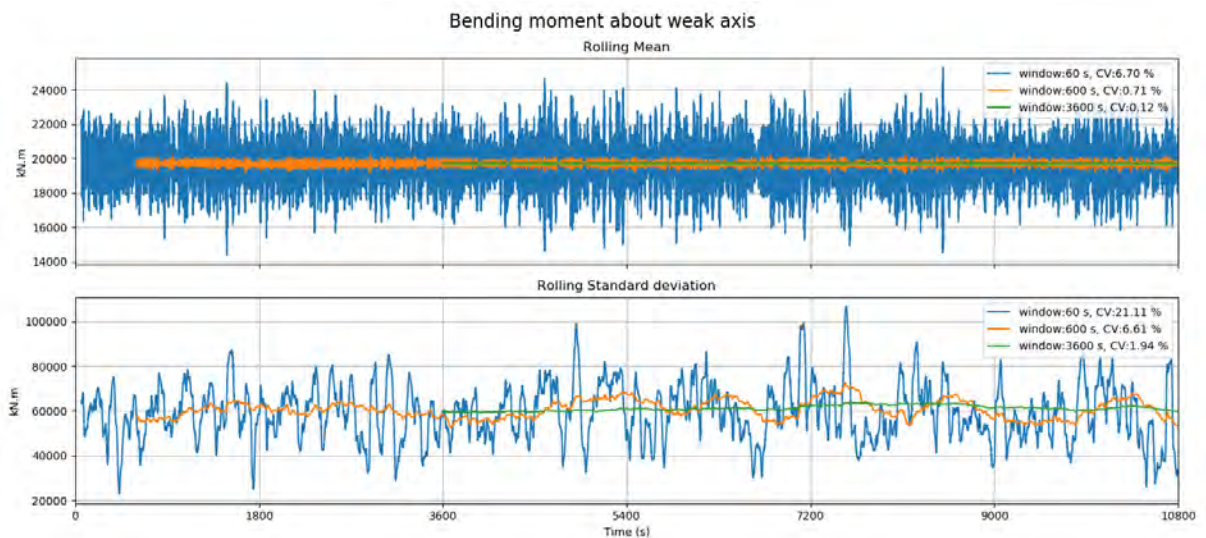


Figure 8-4: Wind sea, weak axis bending moment

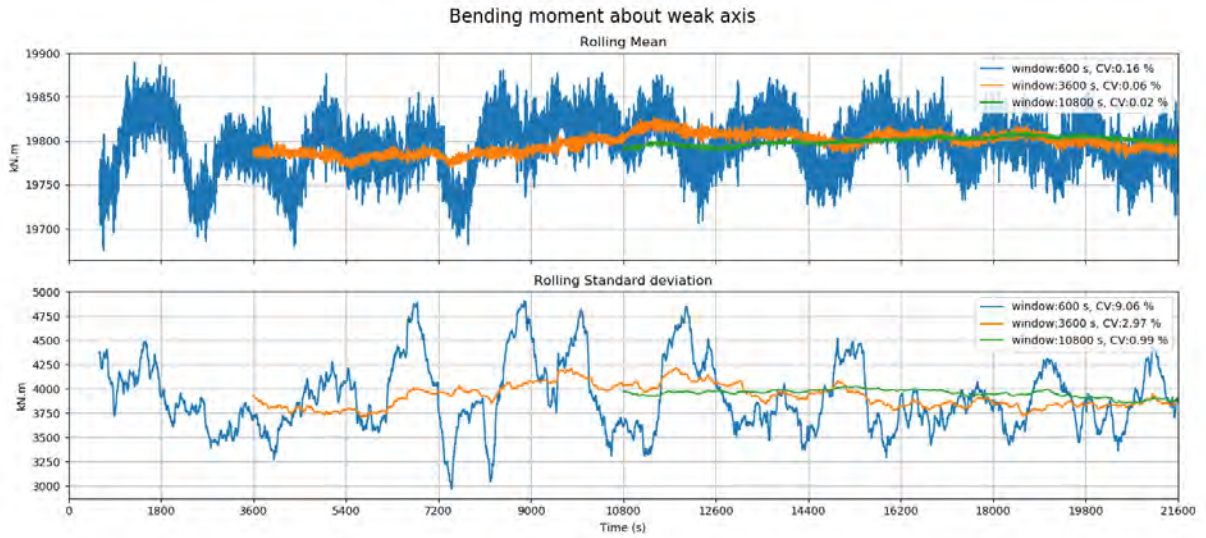


Figure 8-5: Swell sea, weak axis bending moment

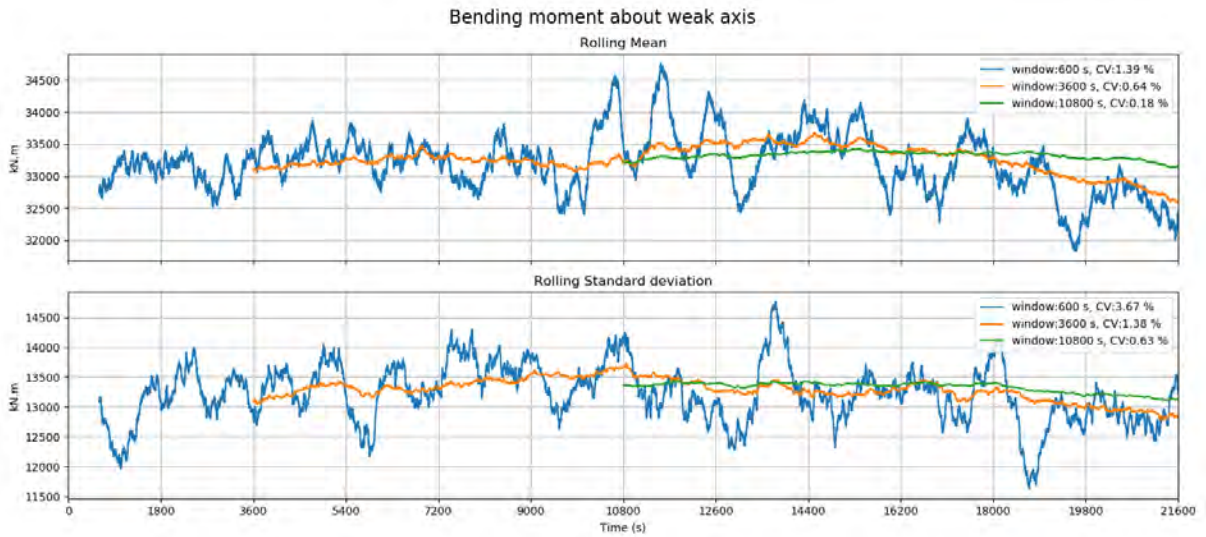


Figure 8-6: Wind, weak axis bending moment

8.3.3 Strong axis bending moment

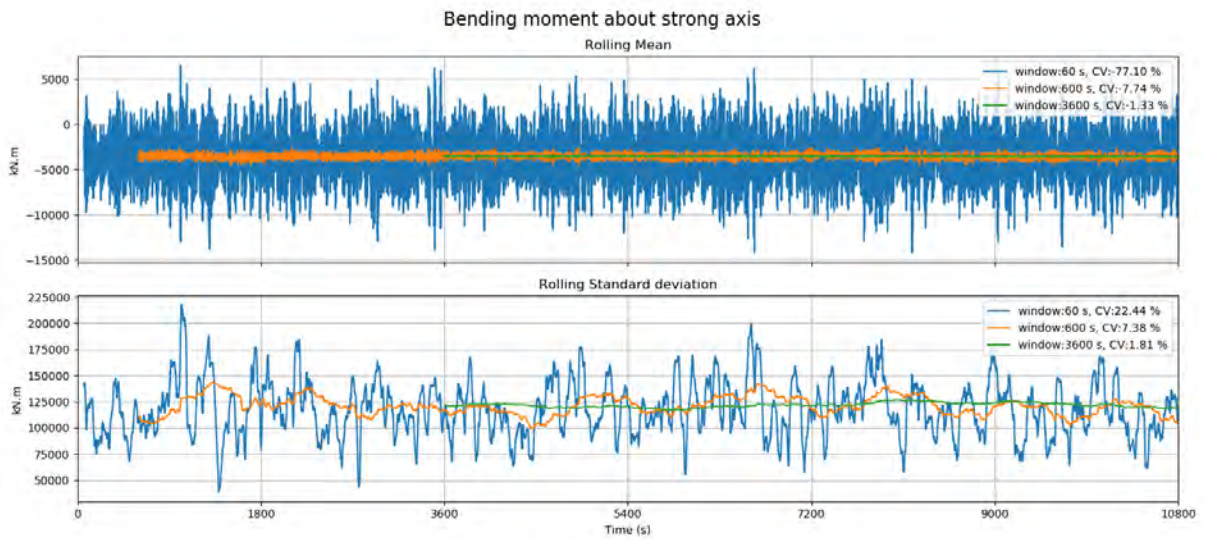


Figure 8-7: Wind sea, strong axis bending moment

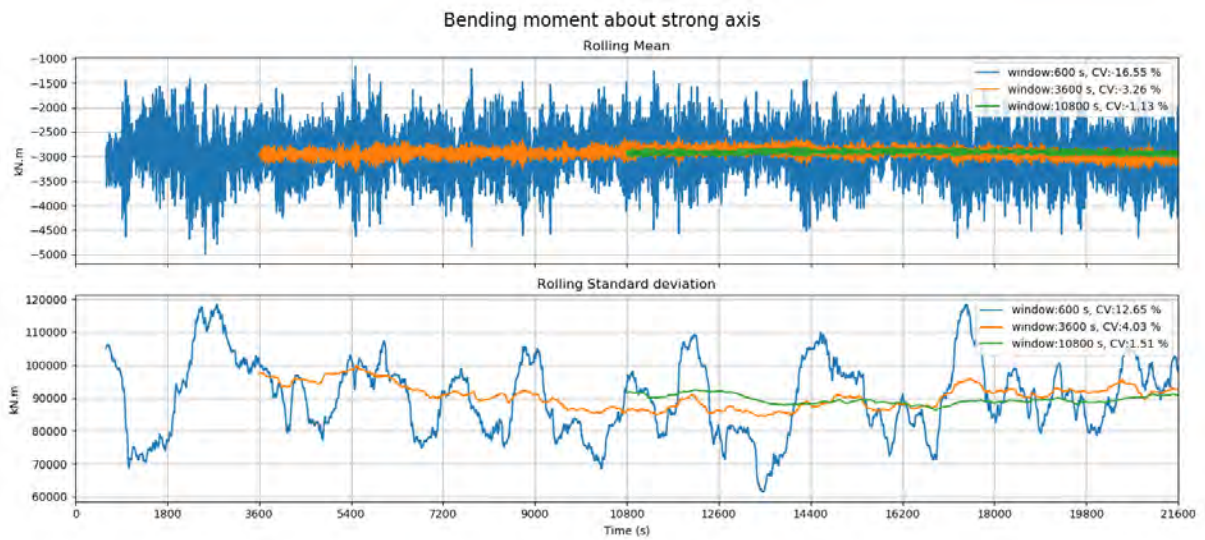


Figure 8-8: Swell sea, strong axis bending moment

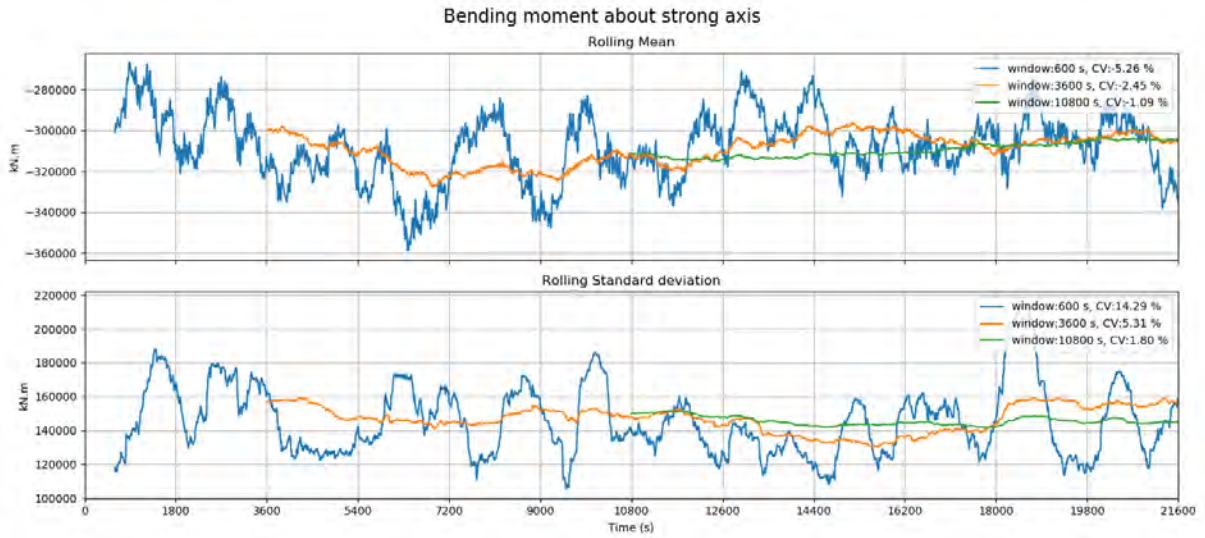


Figure 8-9: Wind, strong axis bending moment

8.3.4 Torsional moment

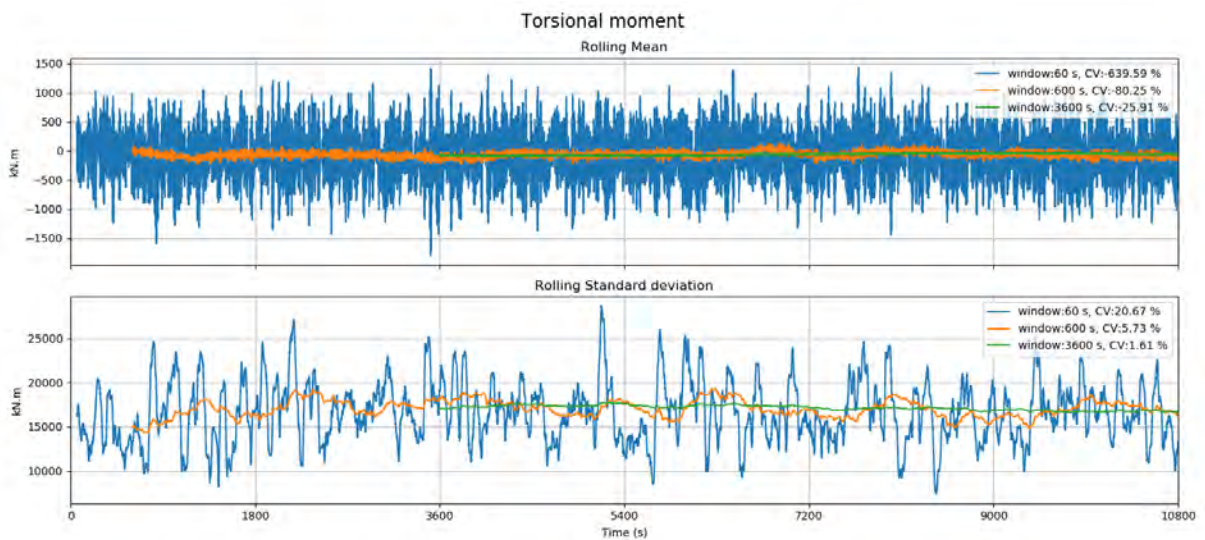


Figure 8-10: Wind sea, torsional moment

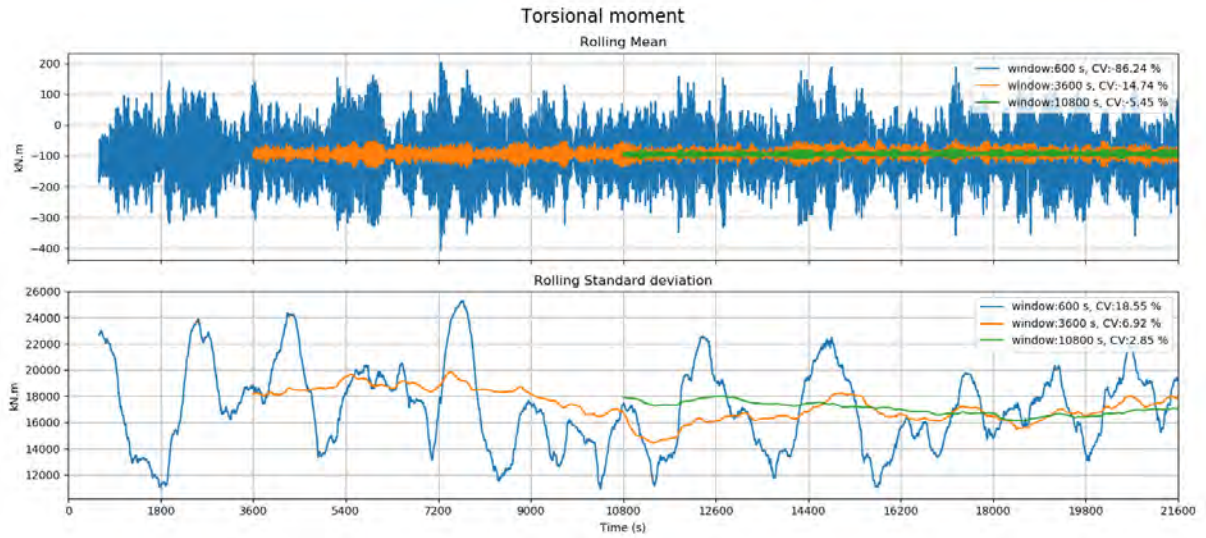


Figure 8-11: Swell sea, torsional moment

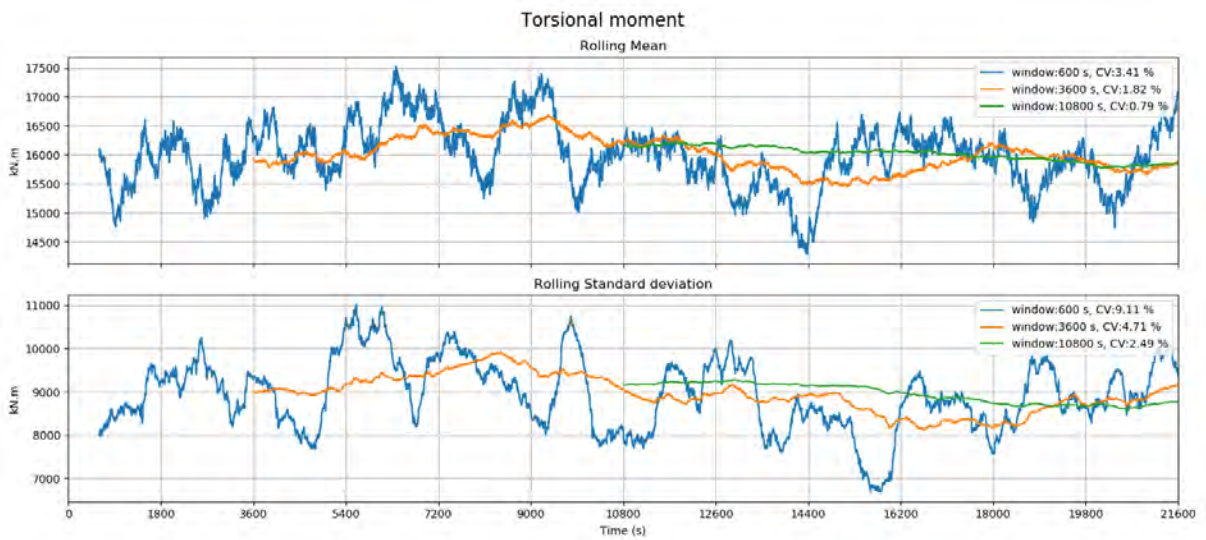


Figure 8-12: Wind, torsional moment

8.4 Ramping

In order to avoid transient effects due to impulse loads at simulation startup, a simulation ramping stage is used in OrcaFlex. During the ramping stage, the dynamic load effects are increased from 0 to 100%.

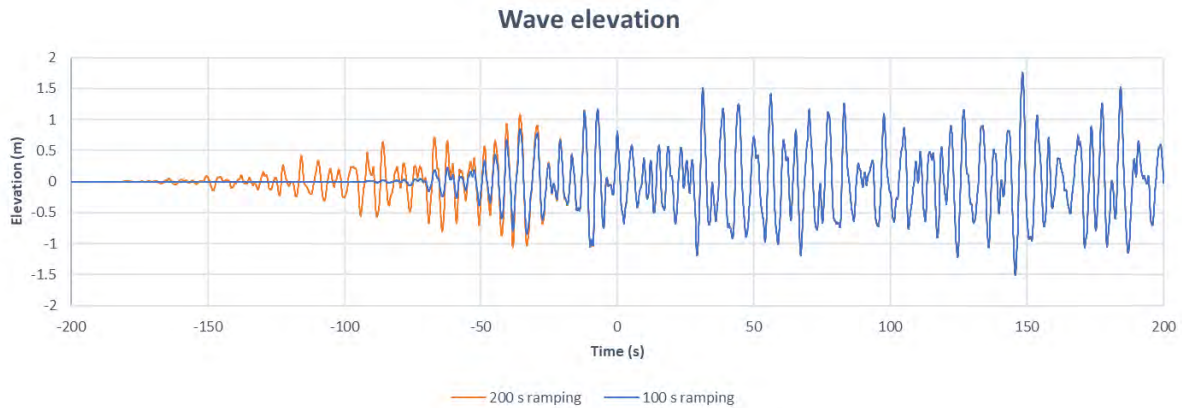


Figure 8-13: Wave elevation ramping

The load effects in this case is the wave amplitude and the wind speed. The time series in the ramping stage is not extracted from the simulation for post processing. To investigate how the duration of the ramping is affecting the results, one wind sea seed and one swell sea seed has been simulated with ramping lengths from 50 s to 1500 s.

Table 8-3: Environmental parameters in ramping study

Parameter	Wind sea	Swell
Wave Type	JONSWAP	JONSWAP
Wave Hs	2.1	0.34
Wave Tp	5.5	13.5
Wave Gamma	2.3	5.0
Wave Direction	75	300
Spreading exponent	8	10

Table 8-4: Simulation parameters in ramping study

Parameter	Wind sea	Swell
Time step	0.2	0.2
Duration	600	600
Ramping period	50-1500	50-1500
Number of directions	15	15
Components per direction	40	40
Number of seeds	1	1

The spectral density of the time domain results is obtained using FFT. Only the first 10 minutes of the time series is considered because the transient effects from simulation start up diminish with time. In wind sea (see Figure 8-14), where only short natural periods are excited, the transient effect vanishes quickly. Therefore, wind sea simulations without 2nd order drift effects included converge with 50 seconds of ramping. With 2nd order drift effects included; the convergence of the low frequencies is slower (see Figure 8-15). However, the spectral energy in low frequencies (<0.1 Hz) is small

compared to the total spectral energy. Full convergence is therefore not considered crucial. Swell sea without 2nd order drift effects included converges with 300 seconds of ramping (see Figure 8-16). After one hour, the transients from a 50 seconds ramping vanish (see Figure 8-18). As we see by comparing Figure 8-16 with Figure 8-17 2nd order drift effects are not affecting the result. The reason for this is that the wave height is small, and the wave peak period is high. The wave drift forces are typically high in sea states with high spectral energy also in the high frequency range, since the 2nd order drift coefficients typically increases at high frequencies.

Note that wind may induce response in eigen modes with lower frequency than swell, and as such require longer ramp-up time. This has not been studied specifically.

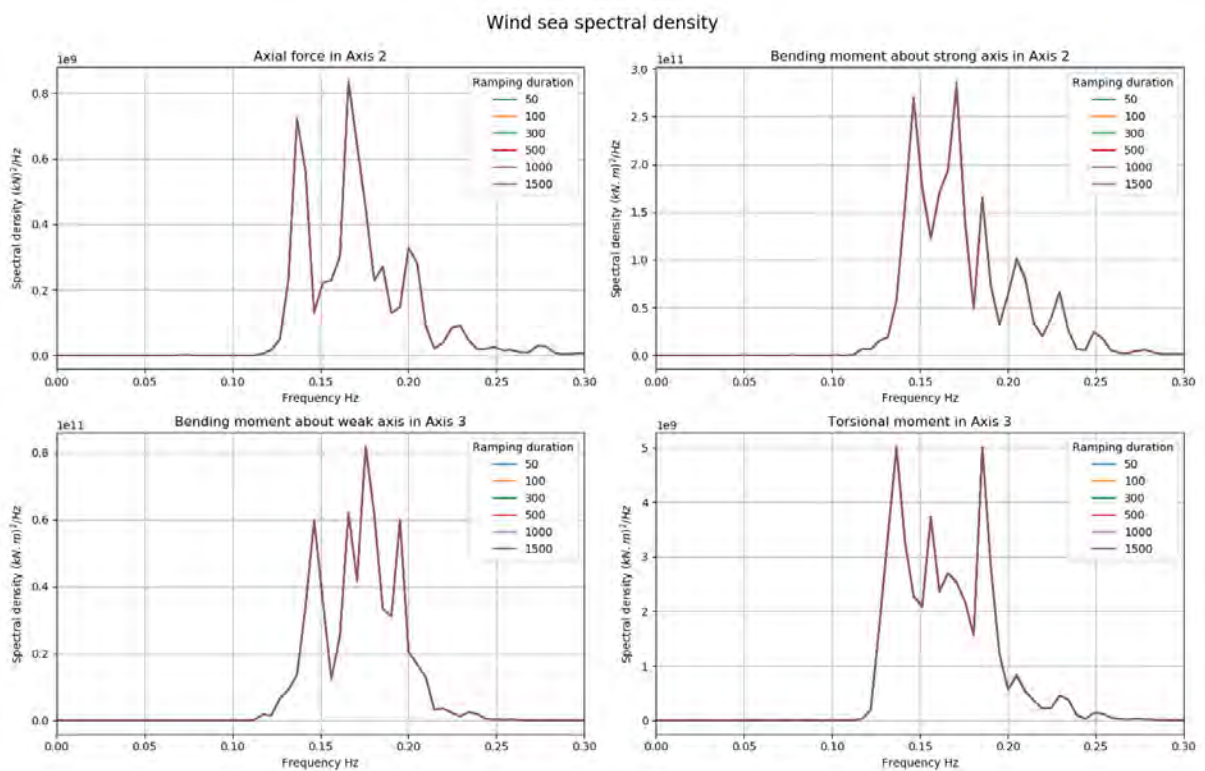


Figure 8-14: Spectral density of 10-minutes wind sea simulation

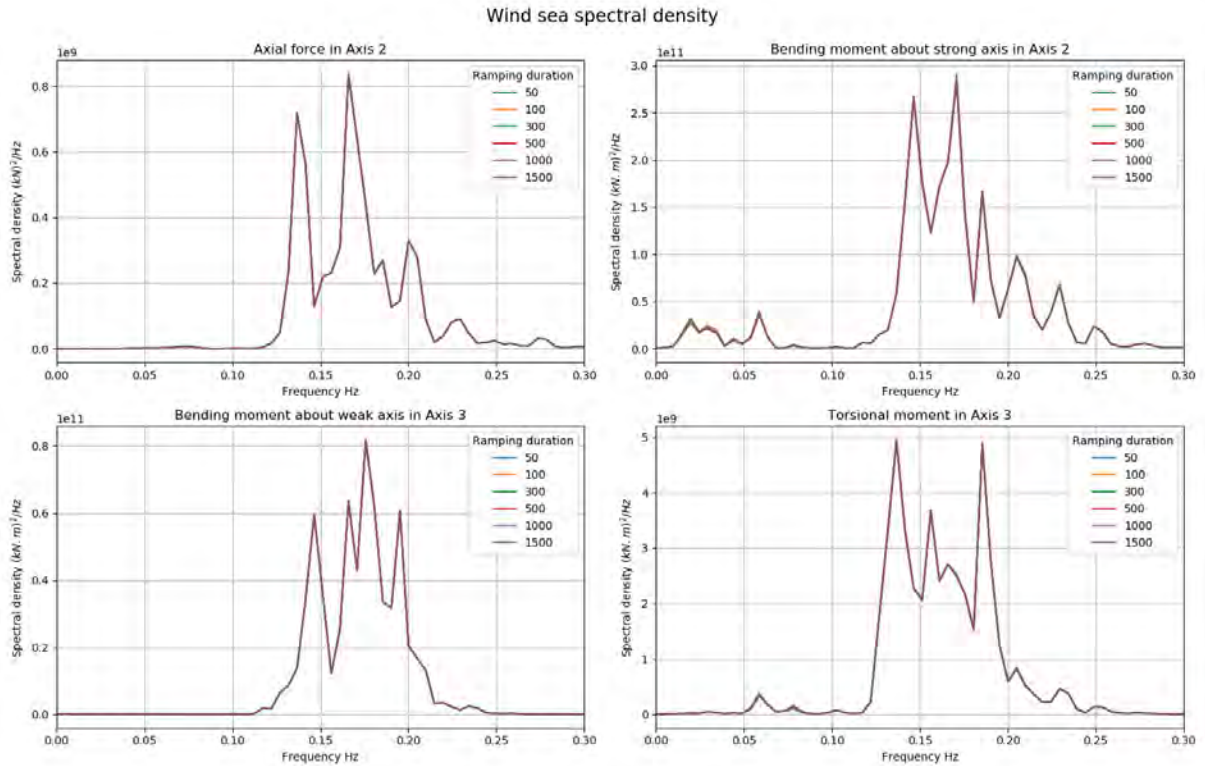


Figure 8-15: Spectral density of 10-minutes wind sea including wave drift effect simulation

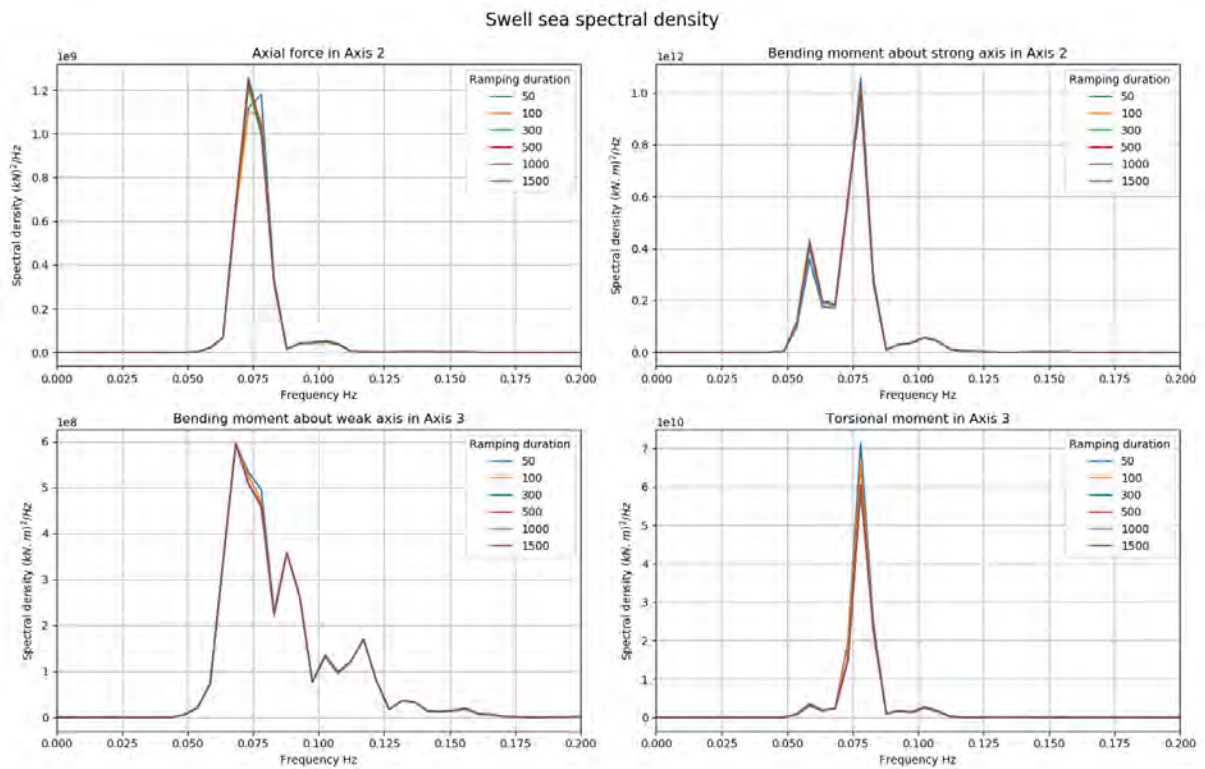


Figure 8-16: Spectral density of 10-minutes swell sea simulation

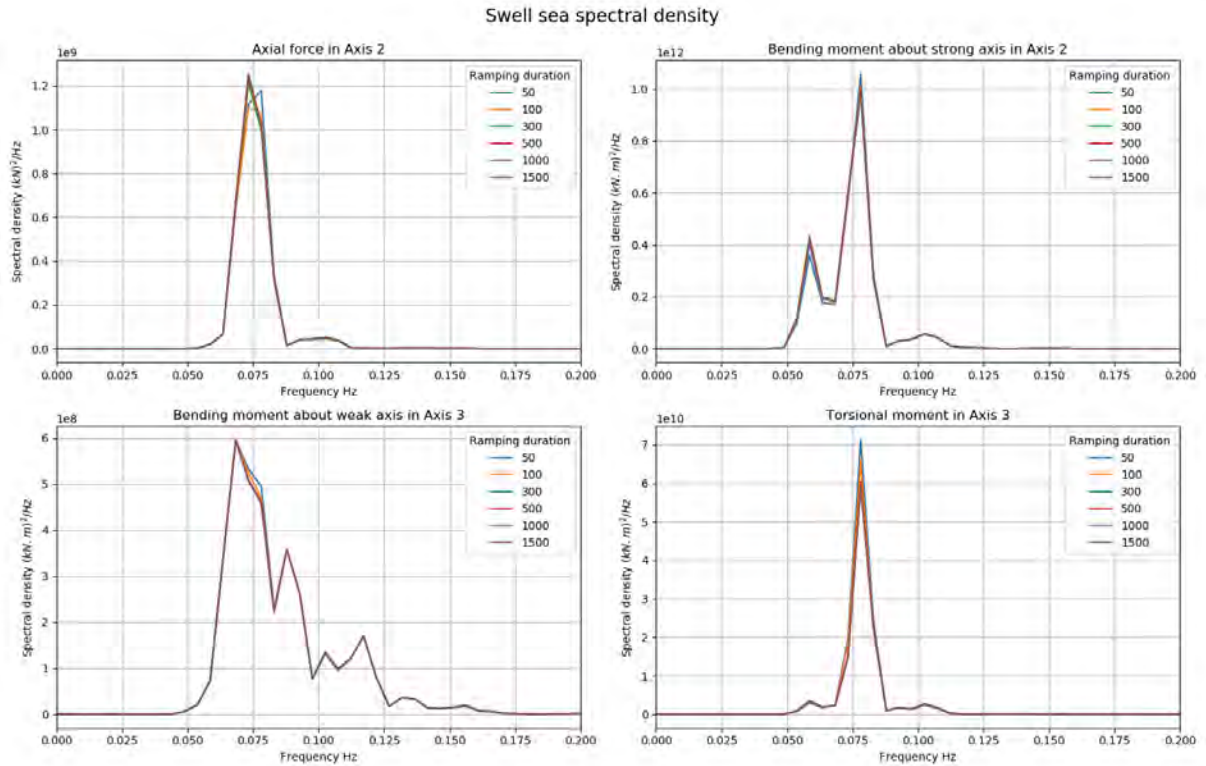


Figure 8-17: Spectral density of 10-minutes swell sea including wave drift effect simulation

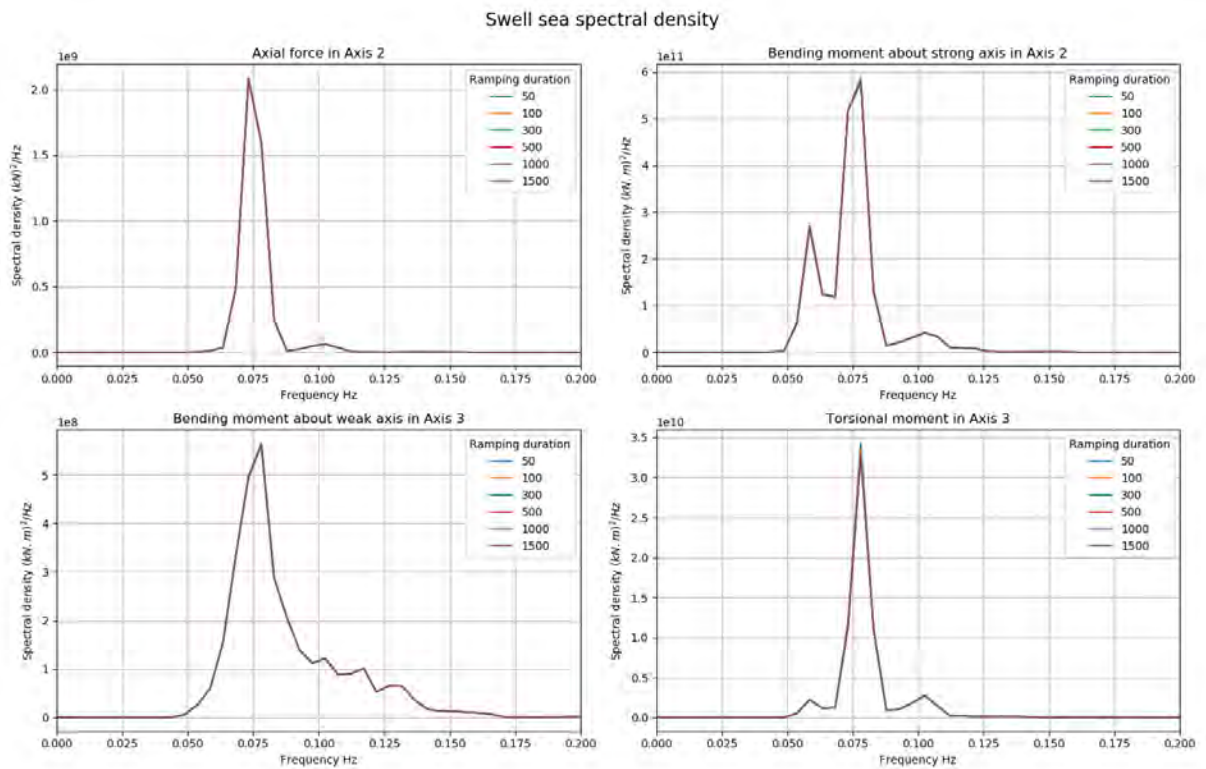


Figure 8-18: Spectral density of 1-hour swell sea simulation

8.5 Time step

The dependency of time step has been analyzed with 0.1, 0.2, 0.3 and 0.5 second time increments respectively in a wind sea environment. The same seed is used in all simulation. The highest natural frequencies are excited in wind sea and the time step is therefore considered to be more critical here than for swell and wind conditions.

Table 8-5: Environmental parameters in time step study

Parameter	Wind sea
Wave Type	JONSWAP
Wave Hs	2.1
Wave Tp	5.5
Wave Gamma	2.3
Wave Direction	75
Spreading exponent	8

Table 8-6: Simulation parameters in time step study

Parameter	Wind sea
Time step	0.1-0.5
Duration	3600
Ramping period	300
Number of directions	15
Components per direction	40
Number of seeds	1

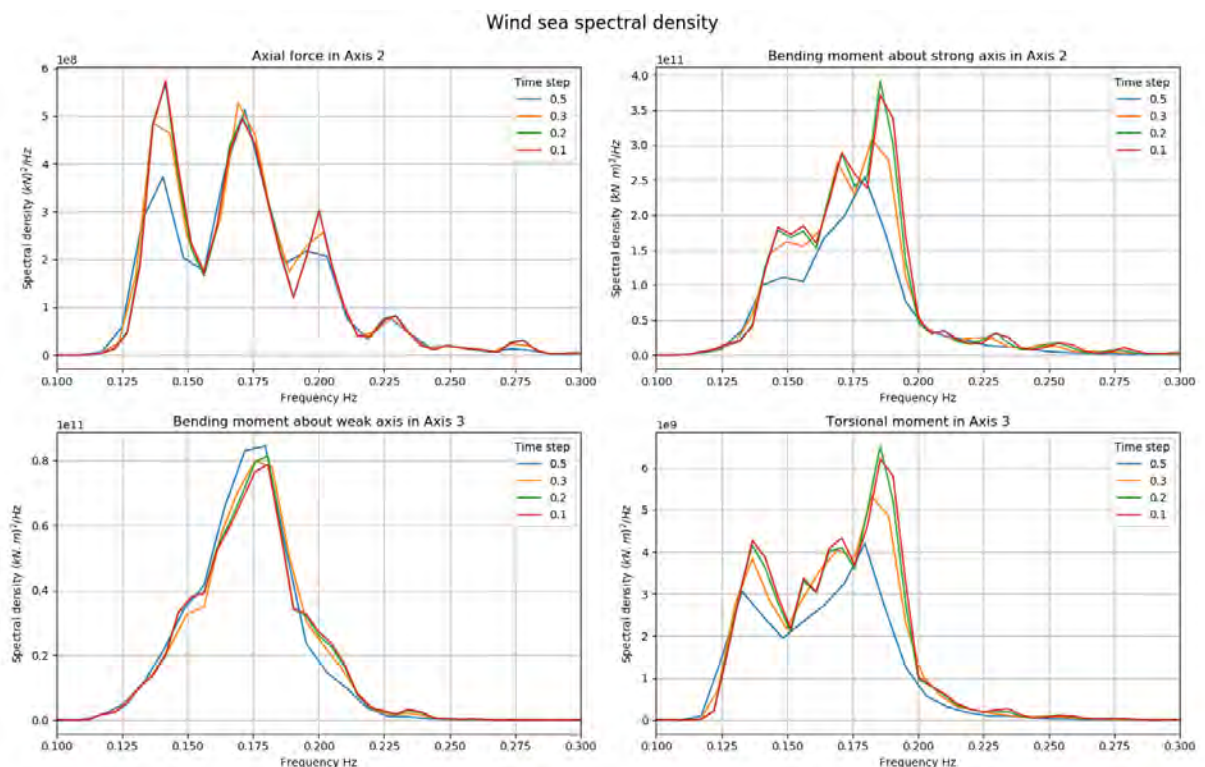


Figure 8-19: Spectral density of wind sea with varying time steps

The analysis indicates that time step of 0.2 seconds is small enough to capture the processes with high precision while maintaining a reasonable computational cost.

8.6 Wave spectrum discretization

8.6.1 Conclusion

The time domain analysis is performed with 600 wave components discretized with the equal energy approach. As the analysis shows, this is enough to capture the physics in the analyzed sea state. However, the discretization is not optimal because the same level of precision could be achieved with less wave components discretized with refinement where it is needed. As long as there is no signal repetition and the effects are captured, less wave components should be used to save computation time.

8.6.2 Analysis

The wave spectrum may be discretized into discrete wave components using various methods. The energy in each wave component is proportional to the wave amplitude squared.

$$E \propto \zeta_i^2 = 2 \int_{f_i^-}^{f_i^+} S(f) df$$

In OrcaFlex, there are three methods readily available.

- Arithmetic progression
- Geometric progression
- Equal energy

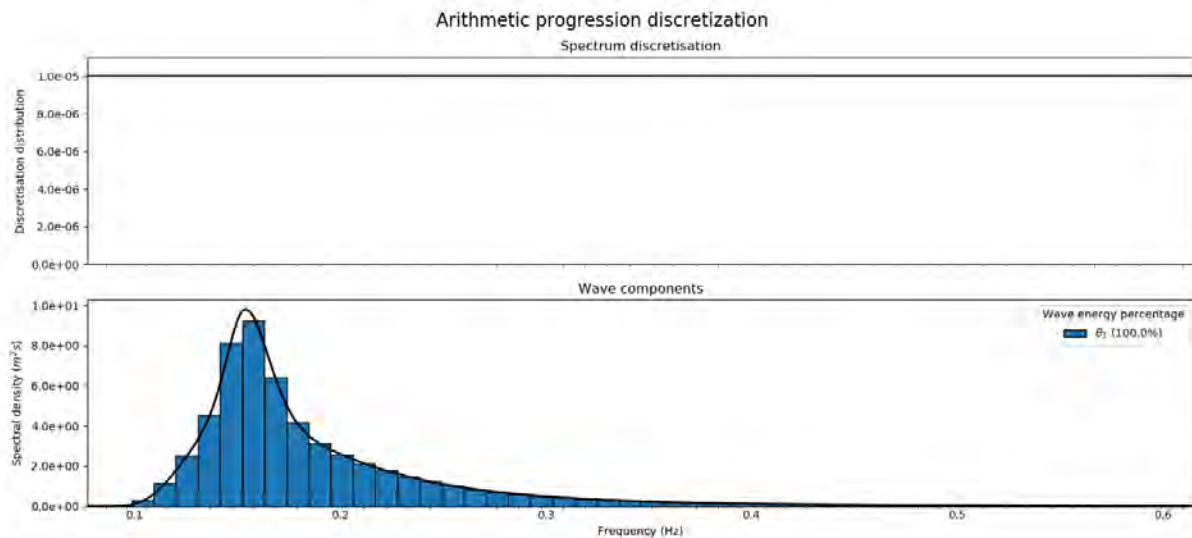


Figure 8-20: Arithmetic progression

In arithmetic progression, the frequency increments are constant, and the wave amplitudes are varying.

$$f_i = f_{i-1} + df$$

The wave signal will be repeated after $T = N / (f_{max} - f_{min})$ seconds, where N is the number of wave components. In order to simulate a spectral frequency range of 1.5 Hz for 1 hour without signal repetition, 5400 wave components are needed.

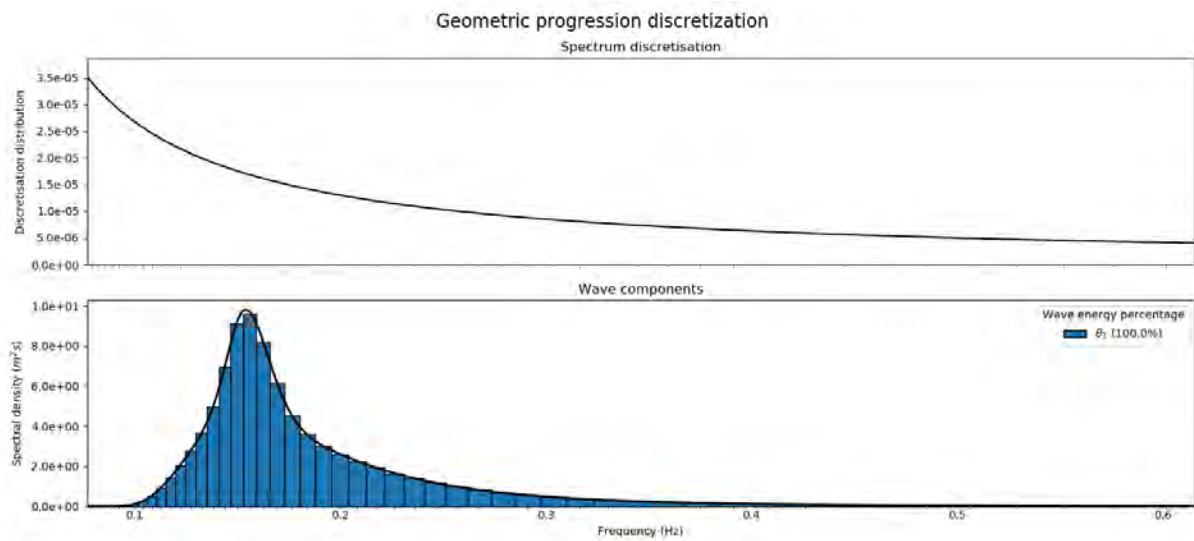


Figure 8-21: Geometric progression

In geometric progression, the ratio between successive frequencies is constant, and the wave amplitudes are varying.

$$f_{i+1} = r \cdot f_i$$

The ratio r is defined as $r = (f_{max}/f_{min})^{1/N}$

The geometric progression discretization method does not suffer from signal repetition, and hence much fewer wave components are needed. The resolution is higher for low frequencies.

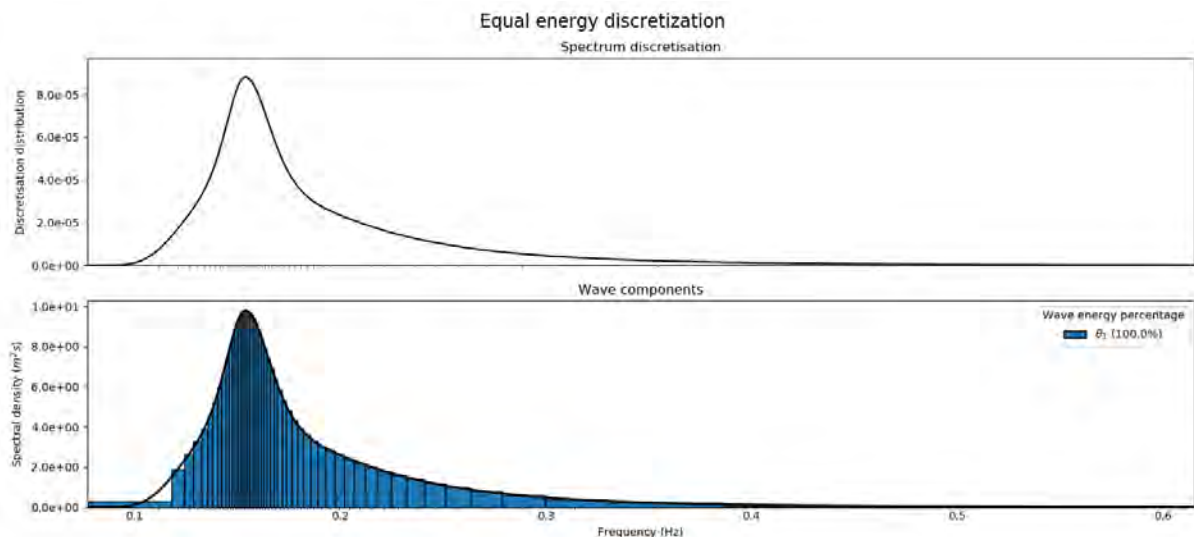


Figure 8-22: Equal energy

In the equal energy approach, the wave amplitudes are constant, and the wave frequency increments are varying. This means that the frequency increments are small where the spectral density is high. In practise there will be no signal repetition for equal energy discretization, and much fewer wave components are needed to represent the spectrum. It is however important to notice that the frequency increments will be large when the spectral density is low. The energy in these

frequencies is concentrated in few wave components, which may yield unrealistic representation of the spectrum, especially for structures with many important natural periods.

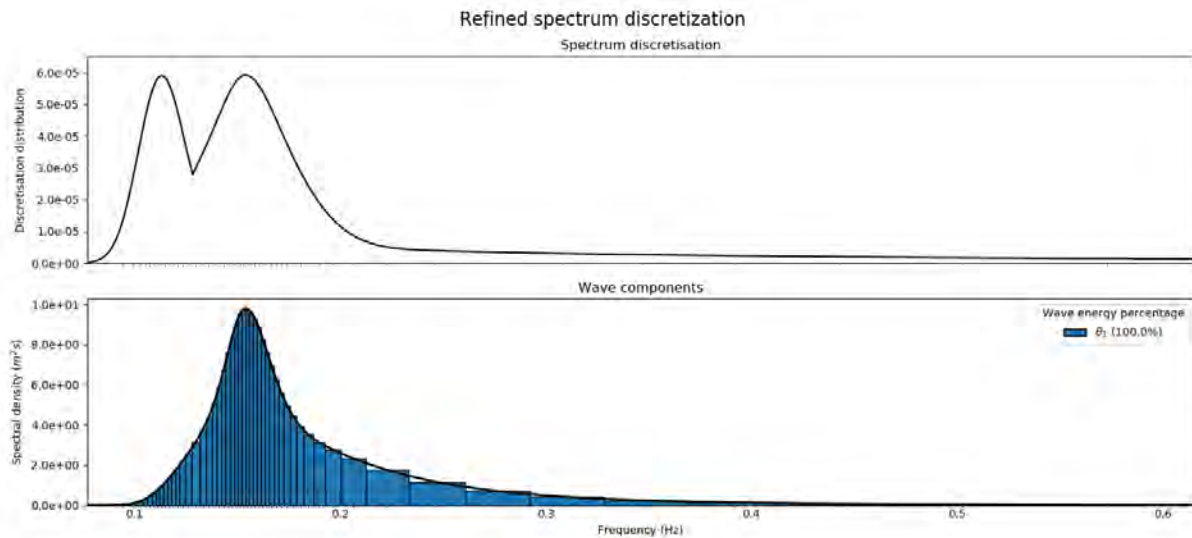


Figure 8-23: Refined discretization

In order to ensure a fine discretization where it is needed (around the structural responses), and at the same time avoid signal repetition an alternative (refined) discretization method is proposed. The discretization resolution could for example be modelled using a set of gaussian distributions with mean at the frequencies of interest with standard deviation to control the concentration of the resolution. In addition, the spectral density could be included to introduce a higher weighting on the frequencies with most wave energy.

To investigate how the total number of frequencies and their distribution affect the results, the following has been simulated.

Table 8-7: Environmental parameters in wave spectrum discretization study

Parameter	Equal energy	Refined
Wave Type	JONSWAP	JONSWAP
Wave Hs	3.1	3.1
Wave Tp	6.5	6.5
Wave Gamma	2.3	2.3
Wave Direction	105	105
Spreading exponent	8	8

Table 8-8: Simulation parameters in wave spectrum discretization study

Parameter	Equal energy	Refined
Time step	0.2	0.2
Duration	3600	3600
Ramping period	300	300
Number of directions	15	15
Components per direction	10-50	5-50
Number of seeds	10	10

The 10 seeds are merged into one long time series which is transformed to frequency plane using FFT. From the below plots it is obvious that equal energy method needs more wave components than the refined discretization method in order to capture the spectral details near 10 seconds.

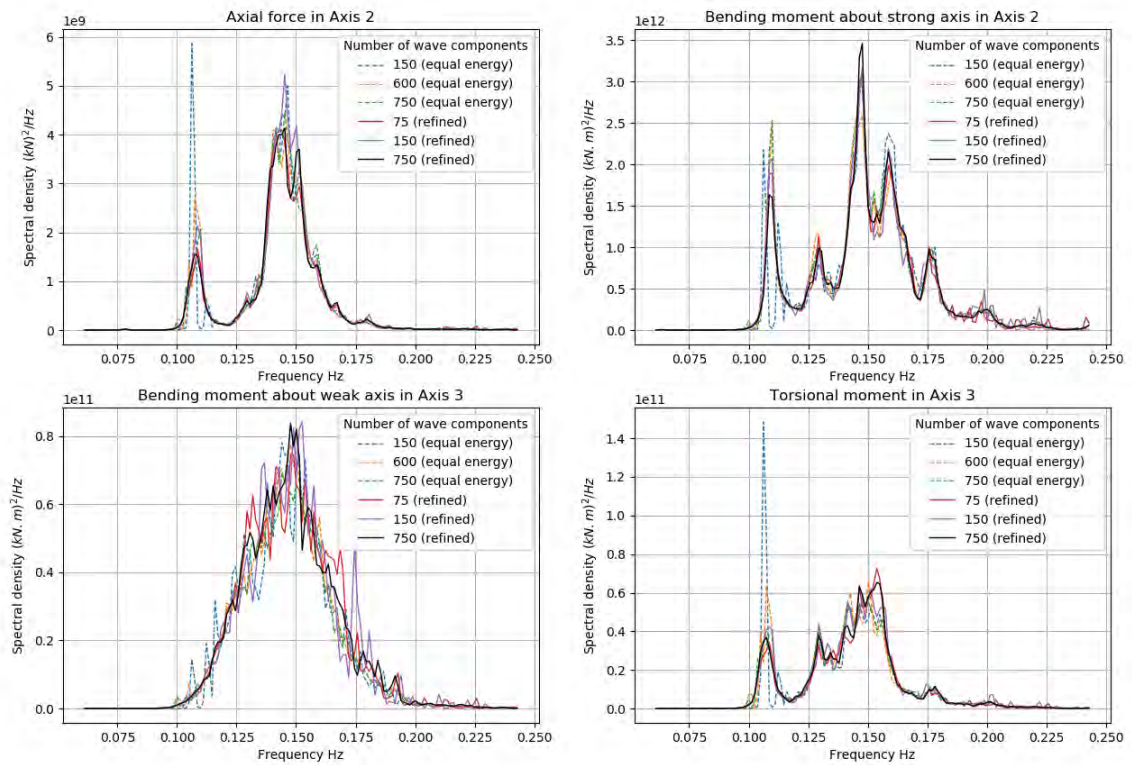


Figure 8-24: Wave spectrum discretization benchmark

8.7 Wave direction discretization

In time domain analysis, the wave spreading function is discretized using the equal energy approach, which means that the wave heading increments are smaller near the main wave direction. The wave spectrum is discretized into a set of N wave components which are distributed randomly among the N_d directions in a way that gives N_f wave components in each of the N_d directions. A parameter study with varying N_d has been performed for a wind sea condition and a swell sea condition. The total number of wave components $N = N_d \times N_f$ should be kept constant in all simulations to ensure that only the directional discretization is being studied.

Table 8-9: Environmental parameters in wave direction discretization study

Parameter	Wind sea	Swell sea
Wave Type	JONSWAP	JONSWAP
Wave Hs	2.1	0.34
Wave Tp	5.5	13.5
Wave Gamma	2.3	5.0
Wave Direction	75	300
Spreading exponent	8	10

Table 8-10: Simulation parameters in wave direction discretization study

Parameter	Wind sea	Swell sea
Time step	0.2	0.2
Duration	3600	3600
Ramping period	300	300
Number of directions	5-21	5-21
Components per direction	120-29	120-29
Number of seeds	10	10

From the spectral density plots below, it can be concluded that $N_d=5$ is too coarse to capture all the effects precisely. Overall, $N_d=15$ seems to be close enough to $N_d=21$ for both wind waves and swell and is considered converged for practical purposes.

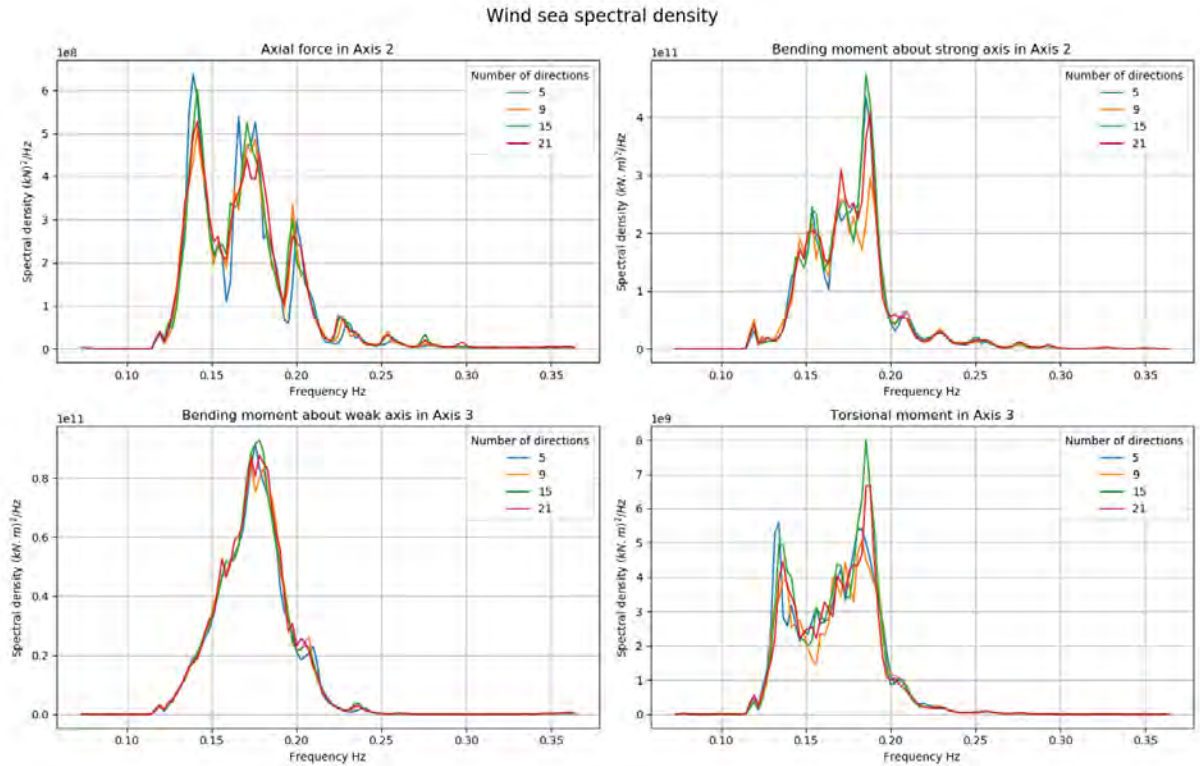


Figure 8-25: Spectral density in wind sea with varying number of wave directions

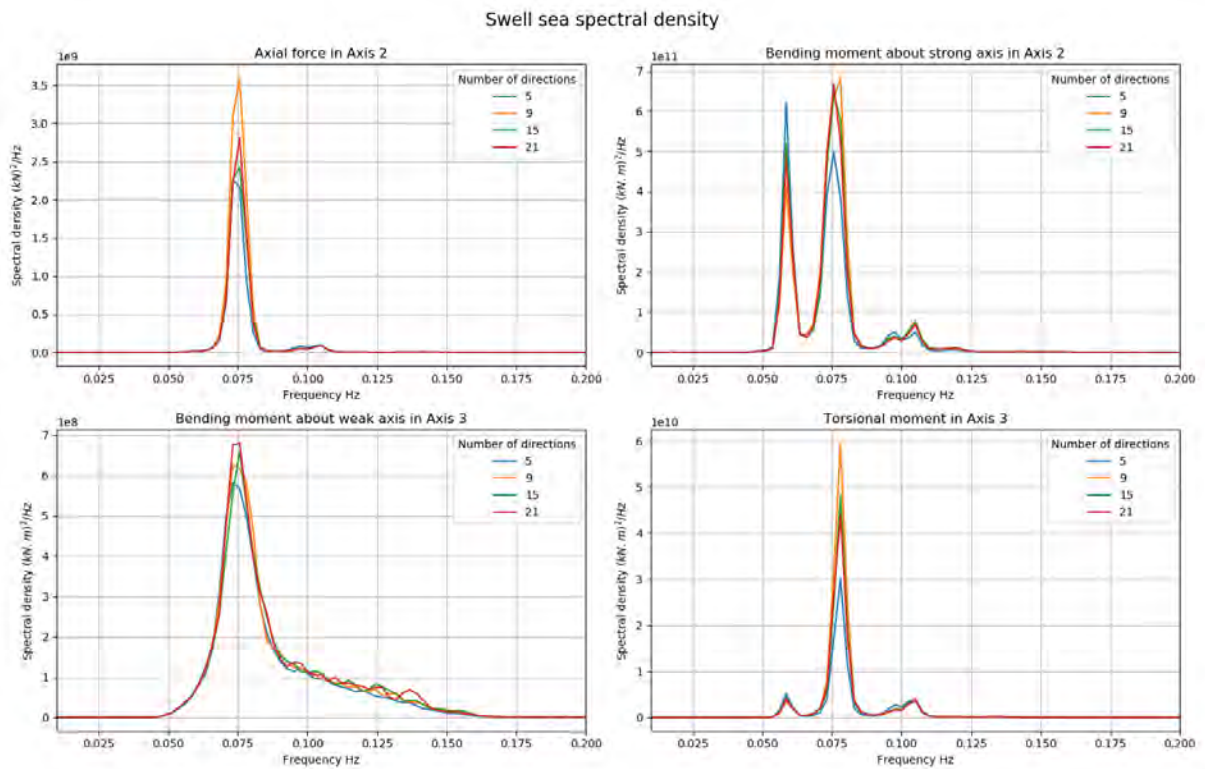


Figure 8-26: Spectral density in swell sea with varying number of wave directions

8.8 Seed variability

To investigate the seed variability, 50 seeds of 3600 s have been simulated in Wind sea, Swell sea and Wind respectively.

Table 8-11: Environmental parameters in seed variability study

Parameter	Wind sea	Swell	Wind
Wave Type	JONSWAP	JONSWAP	
Wave Hs	2.1	0.34	
Wave Tp	5.5	13.5	
Wave Gamma	2.3	5.0	
Wave Direction	75	300	
Spreading exponent	8	10	
Wind Direction			100
Wind Speed			22.5

Table 8-12: Simulation parameters in seed variability study

Parameter	Wind sea	Swell	Wind
Time step	0.2	0.2	0.2
Duration	3600	3600	3600
Ramping period	300	300	300
Number of directions	15	15	15
Components per direction	40	40	40
Number of seeds	50	50	50

The cumulative absolute relative error of the resulting standard deviations is then plotted to examine the seed convergence. As one has a total of 50 different realizations, the realizations may be combined in several different ways giving you different convergence plots. We have randomly chosen 10000 different paths of combining the seeds and then used these as a basis for our calculation.

The postulate here is that the mean of the 50 realizations give the “correct” answer. Based on this, the deviations from the “correct” answer are calculated for each of these 10000 paths as a function of the number of realizations that are included. The results of these calculations for a selected subset of response results are shown on the following pages. Based on this cloud of results the 50 percentile and 90 percentile absolute relative error are estimated as a function of the number of seeds included.

The analysis shows that 10 seeds are enough to achieve at least 96 % convergence of the standard deviation with 90% certainty.

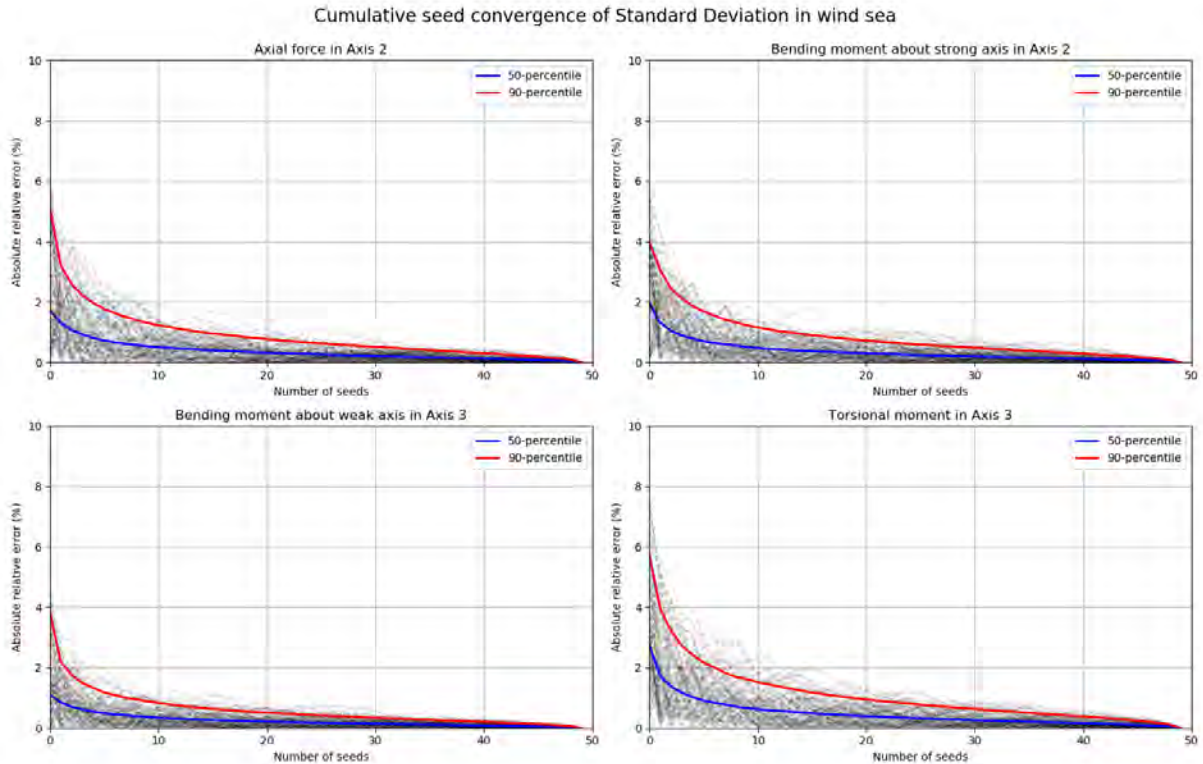


Figure 8-27: Wind sea seed convergence

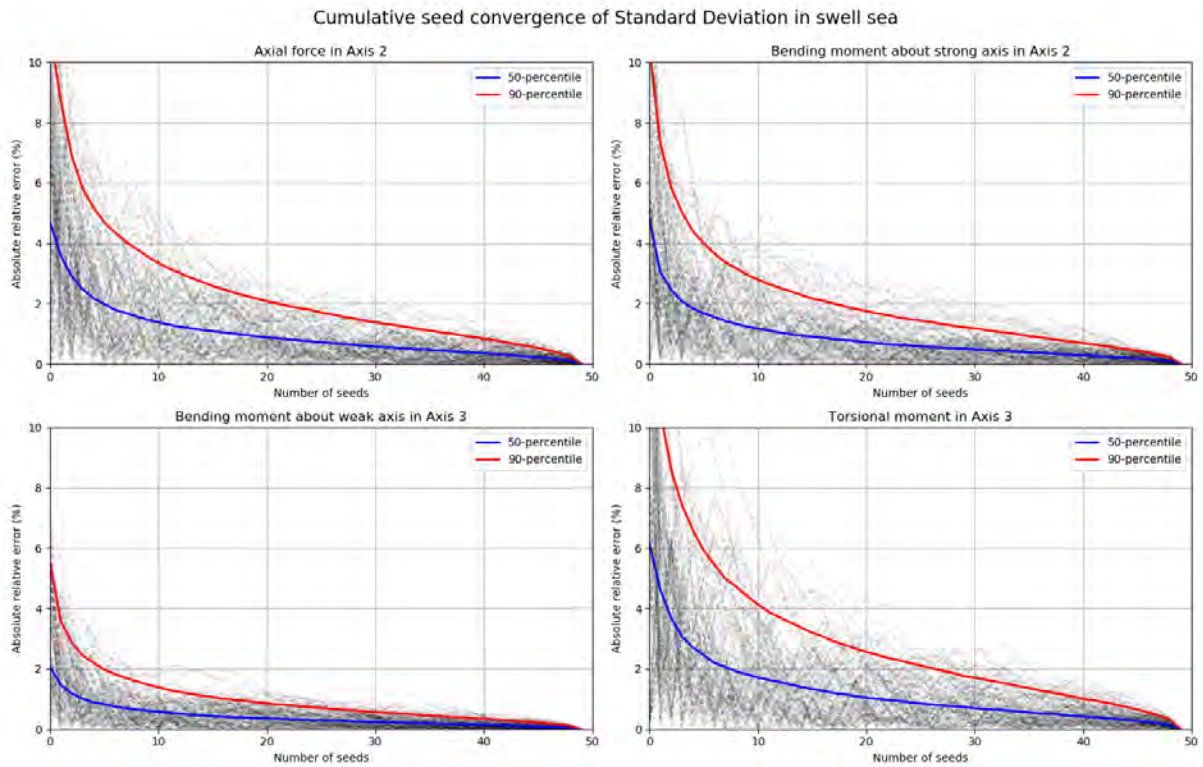


Figure 8-28: Swell sea seed convergence

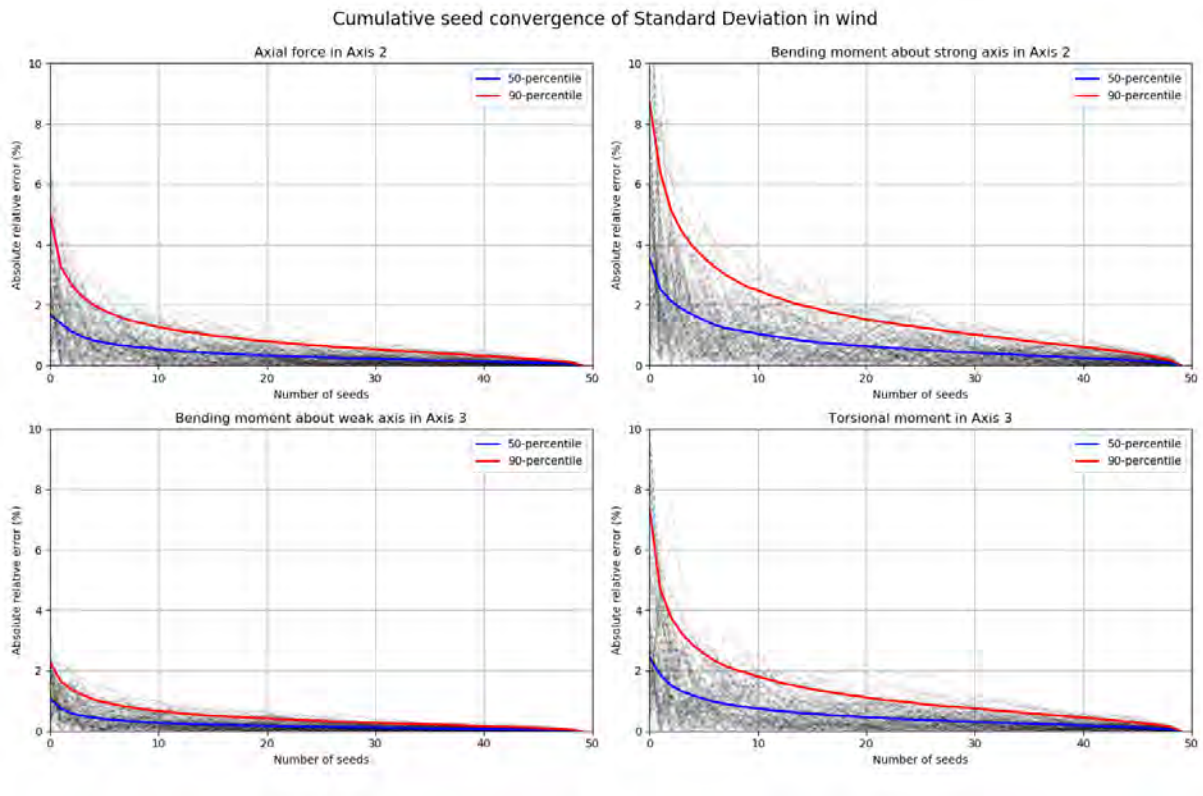


Figure 8-29: Wind seed convergence

8.9 Number of wave components in frequency domain analysis

The number of wave components needed to converge the frequency domain analysis is investigated by simulating a wind sea condition using 50, 150, 500, 1000 and 1500 wave components in each direction respectively.

Table 8-13: Environmental parameters in frequency domain component study

Parameter	Wind sea
Wave Type	JONSWAP
Wave Hs	2.1
Wave Tp	5.5
Wave Gamma	2.3
Wave Direction	75
Spreading exponent	8

Table 8-14: Simulation parameters in frequency domain component study

Parameter	Wind sea
Time step	na
Duration	na
Ramping period	na
Number of directions	15
Components per direction	50-1500

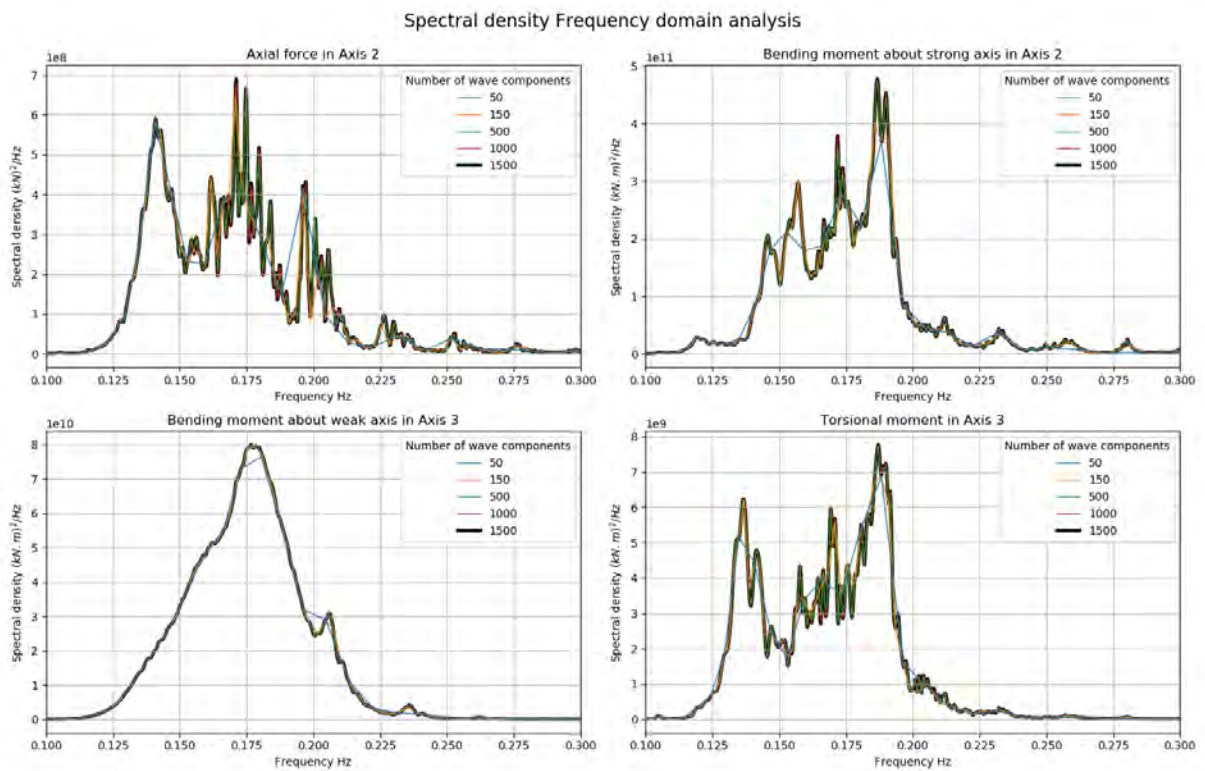


Figure 8-30: Spectral density of varying number of wave components in frequency domain analysis

In Figure 8-31 below the absolute relative error is plotted against the number of wave components used in the frequency domain analysis. The analysis shows that with 500 wave components in each direction the analysis is converged with less than 0.1% relative error (see). The absolute relative error of the standard deviation is defined as

$$err(\sigma) = \text{abs}(1 - \sigma/\sigma_{converged})$$

With 150 wave components the relative error of the standard deviation is less than 1.5%. This is considered to be sufficiently precise and 150 wave components therefore is assumed to be sufficient to predict the response accurately.

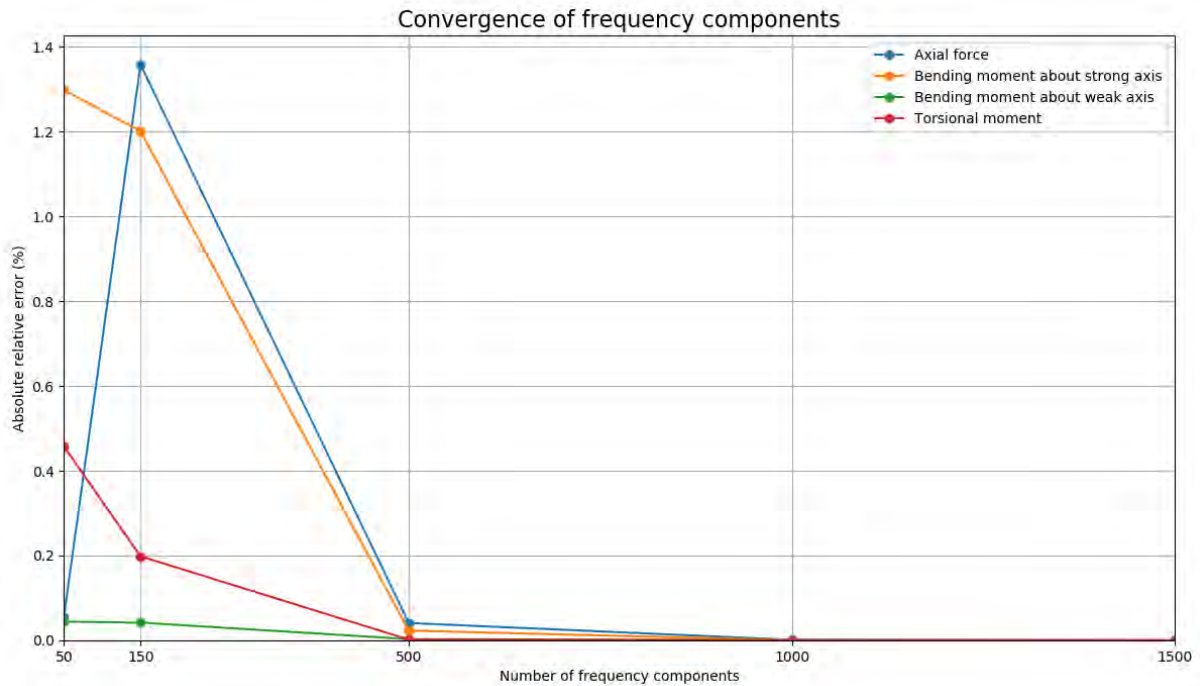


Figure 8-31: Convergence of the standard deviation

8.10 Frequency vs time domain analysis

In the following OrcaFlex frequency domain simulations are compared with OrcaFlex time domain simulations. The two are compared with respect to forces and moments in the bridge girder. 50 seeds of time domain simulations are compared with one frequency domain simulation for one wind sea climate. The results show that for 100 year return period waves the frequency domain calculations match the time domain calculations accurately. 150 components per direction is assumed to be sufficient to give accurate frequency domain results (ref. section 8.9).

Table 8-15: Included effects in the benchmark between frequency domain and time domain

Included effects	Frequency Domain	Time Domain
Wave Load (1 st order)	YES	YES
Wave drift load (2 nd order)	NO	NO
Wave drift damping	NO	NO
Sum frequency load (2 nd order)	NO	NO
Added mass and damping	YES	YES
Quadratic damping	YES	YES

In Table 8-16 the wave climate used in the benchmark between frequency domain and time domain is shown.

Table 8-16: Environmental parameters in frequency domain vs time domain study

Parameter	Frequency domain	Time domain
Wave Type	JONSWAP	JONSWAP
Wave Hs	2.1	2.1
Wave Tp	5.5	5.5
Wave Gamma	2.3	2.3
Wave Direction	75	75
Spreading exponent	8	8

Table 8-17: Simulation parameters in frequency domain vs time domain study

Parameter	Frequency domain	Time domain
Time step	na	0.2
Duration	na	3600
Ramping period	na	300
Number of directions	15	15
Components per direction	150	40
Number of seeds	na	50

The spectral density of representative forces and moments in Axis 2 and 3 is plotted in Figure 8-32. . The spectral density of the time domain results is obtained using FFT.

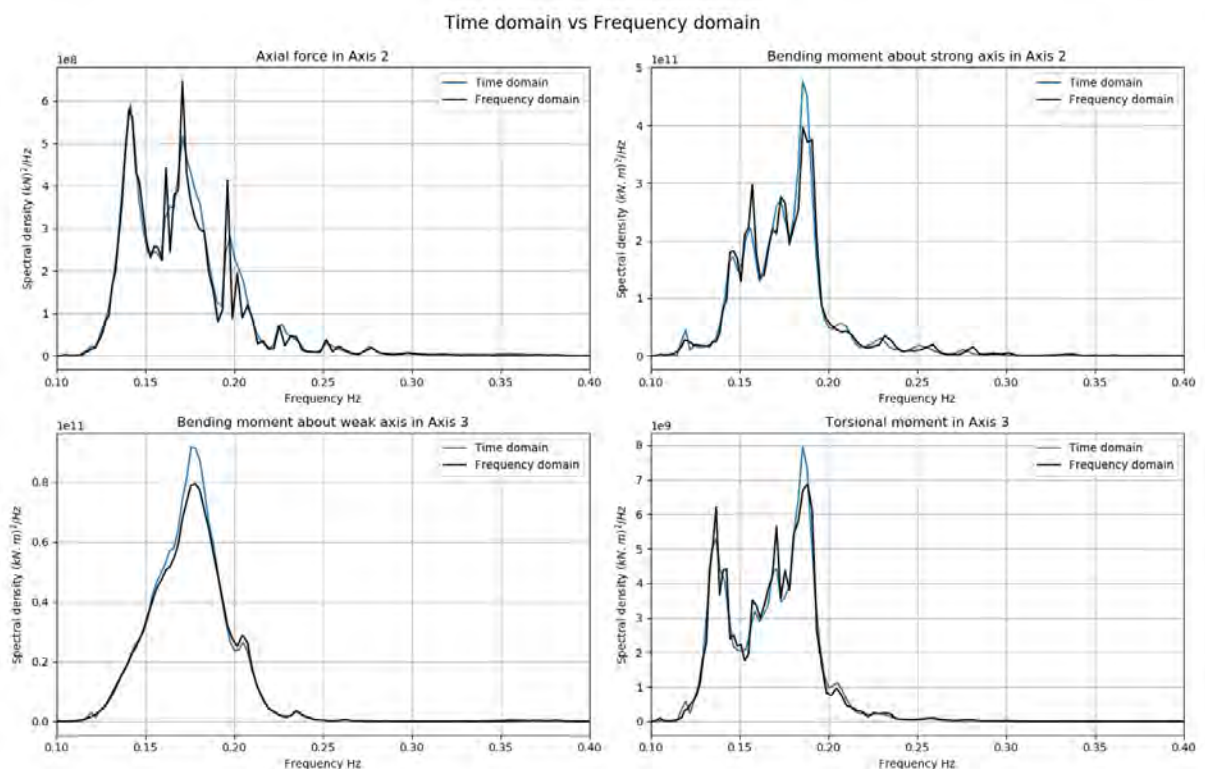


Figure 8-32: Spectral density from time domain and frequency domain

The spectral moments m_0 and m_2 are extracted from the spectral density by integrating over all frequencies.

$$m_i = \int_0^{\infty} f^i S(f) df$$

From the spectral moments, standard deviation σ , zero up crossing period T_Z and the 1-hour most probable maximum (MPM) estimate can be calculated as following.

$$\sigma = \sqrt{m_0}$$

$$T_Z = \sqrt{\frac{m_0}{m_2}}$$

$$MPM = \sigma \sqrt{2 \ln(3600/T_Z)}$$

Table 8-18: Axial force in Axis 2

	Time domain	Frequency domain
Standard deviation (kN)	5194	5056
Zero up crossing period (s)	5.7	5.8
Most probable 1-hour maximum (kN)	18646	18129

Table 8-19: Bending moment about strong axis in Axis 2

	Time domain	Frequency domain
Standard deviation (kN.m)	122206	121757
Zero up crossing period (s)	5.6	5.6
Most probable 1-hour maximum (kN.m)	439616	438019

Table 8-20: Bending moment about weak axis in Axis 3

	Time domain	Frequency domain
Standard deviation (kN.m)	61355	60012
Zero up crossing period (s)	5.7	5.7
Most probable 1-hour maximum (kN.m)	220485	215659

Table 8-21: Torsional moment in Axis 3

	Time domain	Frequency domain
Standard deviation (kN.m)	17196	17200
Zero up crossing period (s)	5.9	5.9
Most probable 1-hour maximum (kN.m)	61619	61613

9 References

- [1] AMC, "10205546-01-NOT-055 Programvare," 14.02.2019.
- [2] AMC, "SBJ-32-C5-AMC-90-RE-106 : Appendix F: Global Analyses - Modelling and assumptions Rev. 0," 24.05.2019.
- [3] AMC, "SBJ-33-C5-AMC-90-RE-100 : Preferred solution, K12 - main report Rev. 0," 15-08-2019.
- [4] AMC, "SBJ-33-C5-AMC-22-RE-112 : Appendix L: Design of Cable Stayed Bridge and Abutments Rev. 0," 15-08-2019.
- [5] AMC, "SBJ-33-C5-AMC-26-RE-113 : Appendix M: Anchor systems Rev. 0," 15-08-2019.
- [6] AMC, "SBJ-33-C5-AMC-20-RE-105 : Appendix E: Aerodynamics Rev. 0," 15-08-2019.
- [7] AMC, "SBJ-33-C5-AMC-22-RE-111 : Appendix K: Design of Floating Bridge Part Rev. 0," 15-08-2019.
- [8] AMC, "SBJ-32-C5-AMC-90-RE-100 : Concept evaluation - main report Rev. 0," 24.05.2019.
- [9] AMC, "SBJ-33-C5-AMC-05-DR-910 Road alignment K12 rev. 0," 30.06.2019.
- [10] AMC, "SBJ-33-C5-AMC-90-RE-121 : Appendix U: Verification Rev. 0," 15-08-2019.
- [11] AMC, "SBJ-33-C5-AMC-90-RE-119 : Appendix S: Parametric excitation Rev. 0," 15-08-2019.
- [12] Statens Vegvesen, "SBJ-01-C4-SVV-01-BA-001 MetOcean Design basis Rev. 1," 30.11.18.
- [13] AMC, "SBJ-33-C5-AMC-27-RE-110 : Appendix J: Ship collision Rev. 0," 15-08-2019.
- [14] RM, "RM Bridge User Manual. CONNECT Edition (Release 10.3)," 21.11.2017.
- [15] AMC, "SBJ-33-C5-AMC-21-RE-108 : Appendix H: Global Analyses - Special studies Rev. 0," 15-08-2019.
- [16] K. A. Kvåle, R. Sigbjörnsson and Ø. Ole, "Modelling the stochastic dynamic behaviour of a pontoon bridge: A case study," *Computers & Structures*, pp. 123-135, 2016.
- [17] A. Cabboi, F. Magalhães, C. Gentile and Á. Cunha, "Automated modal identification and tracking: Application to an iron arch bridge," *Structural Control and Health Monitoring*, 2016.
- [18] R. S. Pappa, K. B. Elliott and A. Schenk, "Consistent-mode indicator for the eigensystem realization algorithm," *Journal of Guidance, Control, and Dynamics*, pp. 852-858, 1993.
- [19] AMC, "SBJ-33-C5-AMC-90-RE-107 : Appendix G: Global Analyses - Response Rev. 0," 15-08-2019.
- [20] AMC, "SBJ-33-C5-AMC-22-RE-109 : Appendix I: Fatigue analyses Rev. 0," 15-08-2019.

10 Enclosures

- Enclosure 1. Full model description in spread sheet for the K12_07 concept.
- Enclosure 2. AMC, "10205546-11-NOT-095 Analytic mooring line damping", rev.01, 24.05.2019.
- Enclosure 3. AMC, "10205546-01-NOT-055, Programvare", rev. 0. 14.02.2019

Concept development, floating bridge E39 Bjørnafjorden

Appendix F – Enclosure 1

K12_07 Designers format

Concept development, floating bridge E39 Bjørnafjorden

Enclosure 1 – K12_07 Designers format

1 K12_07 Designers format

The “K12_07 Designers format” is presented as a separate Excel-file.

Filename: *Appendix F - Enclosure 1 - K12_07 Designers format.xlsx*

Concept development, floating bridge E39 Bjørnafjorden

Appendix F – Enclosure 2

10205546-11-NOT-095

Analytic mooring line damping

MEMO

PROJECT	Concept development, floating bridge E39 Bjørnafjorden	DOCUMENT CODE	10205546-11-NOT-095
CLIENT	Statens vegvesen	ACCESSIBILITY	Restricted
SUBJECT	Analytic mooring line damping	PROJECT MANAGER	Svein Erik Jakobsen
TO	Statens vegvesen	PREPARED BY	Pål Grøthe Sandnes
COPY TO		RESPONSIBLE UNIT	AMC

SUMMARY

An analytical quadratic damping model has been studied as a tool to achieve a better understanding of the mooring line damping effects, and how to control the damping level by manipulating the mooring spread properties. The model has been developed based on earlier theoretical work which is elaborated the memo. The model has been benchmarked against a full mooring line model to examine its goodness. The model seems to estimate the damping level with high precision for low natural frequencies. For increasing natural frequencies, the model is slightly conservative as it predicts less damping than the full model. This is probably due to the quasi-static assumption on which the model is based and how this affects the local geometry of the line.

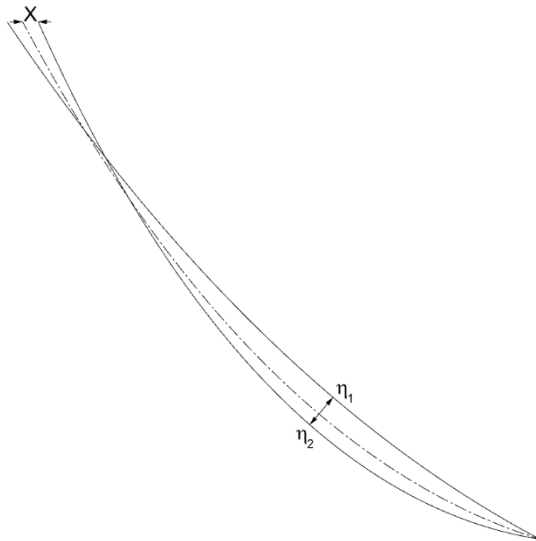
1	24.05.2019	Final issue	PGS	R. M. Larssen	Svein Erik Jakobsen
0	29.03.2019	Status 2 issue	PGS / MS	R. M. Larssen	Svein Erik Jakobsen
REV.	DATE	DESCRIPTION	PREPARED BY	CHECKED BY	APPROVED BY

1 Background

The damping induced by mooring lines has been studied for several decades. With physical insight in the mechanism, we can estimate the damping level which is an advantage in the design of the mooring system.

In Huse's work¹, a quastistic analytical model was developed to estimate the mooring line damping. The damping is estimated based on the total dissipated energy during one full cycle. Huse's analytical damping model has been experimentally verified by later studies² where it was shown that the dissipated energy is quadratically proportional to the angular frequency.

Shortcomings in Huse's model was revisited by Liu and Bergdahl³. While Huse considered the dissipated energy through one full cycle, Liu and Bergdahl considered two half cycles. The reason for this is that the mooring line profile at the extreme offsets are generally not symmetric about the mean position, and the velocity in each half cycle is therefore different. The model was verified by time domain simulations.



Bauduin and Naciri⁴ have also improved Huse's model further by considering transverse mooring line displacements in addition to the vertical displacement.

Webster⁵ has been investigating the effect of mooring line damping in a parametric time domain study. His findings on damping vs pretension is consistent with the findings in this memo.

¹Huse, E., 1986, "Influence of Mooring Line Damping Upon Rig Motions," Proc., 18th OTC Conference.

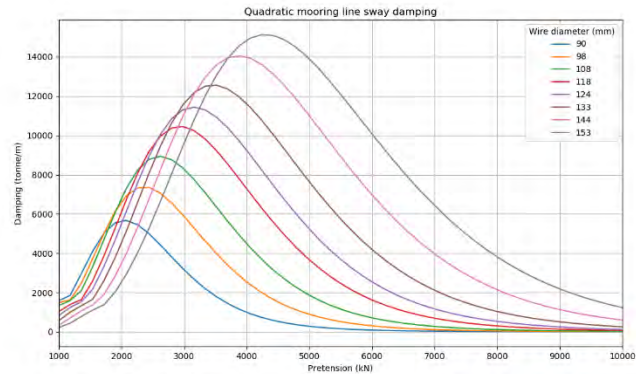
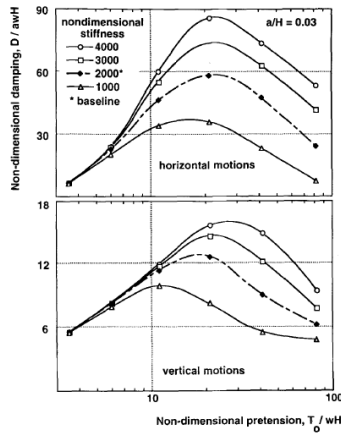
² Raaijmakers, R. M., and Battjes, J. A., 1997, "An Experimental Verification of Huse's Model on the Calculation of Mooring Line Damping," Proceedings, 11th BOSS Conference.

³Liu, Y., and Bergdahl, L., 1998, "Improvement on Huse's Model for Estimating Mooring Cable Induced Damping," Proc., 17th OMAE Conference.

⁴ Bauduin, C., and Naciri, M., 2000, "A Contribution on Quasi-Static Mooring Line Damping," Journal of Offshore Mechanics and Arctic Engineering

⁵ Webster, W. C., 1995, "Mooring-Induced Damping," Ocean Engineering, 22, No. 6, pp. 571-591.

Analytic mooring line damping



The figure to the left is given in Webster’s paper, and the figure to the right is produced with the developed model described in the memo. Webster’s figure is non-dimensional, but the tendency is clear and consistent. Mooring line damping increases with line pretension up to a certain level before the damping decreases with further line tensioning.

2 Theory

The drag force for an infinitesimally short line segment can be expressed as a function of the drag coefficient C_D , the characteristic length D and the crossflow velocity u .

$$dF_D = \frac{1}{2} \rho C_D D u |u| ds$$

The harmonic crossflow velocity is a function of the mooring line normal displacement η , and the angular frequency ω .

$$u = \eta \omega \cos \omega t$$

The total drag force integrated along the line is

$$F_D = \frac{1}{2} \rho C_D D \omega^2 \cos \omega t |\cos \omega t| \int_0^L \eta^2 ds$$

Dissipated energy during one harmonic oscillation

$$\Delta E = \int_0^T F_D u dt = 2 \rho C_D D \omega^3 \int_0^L \eta^3 ds \int_0^{T/4} \cos^3 \omega t dt^6$$

Due to the quasi-static consideration, the crossflow velocity along the mooring line is a function of the top offset only. The energy dissipated due to the mooring line drag force is therefore equal to

$$\Delta E = \int_0^T B_2 \dot{x} |\dot{x}| dt$$

B_2 is the quadratic damping coefficient, and x is the harmonic offset at the top point (X is the offset amplitude).

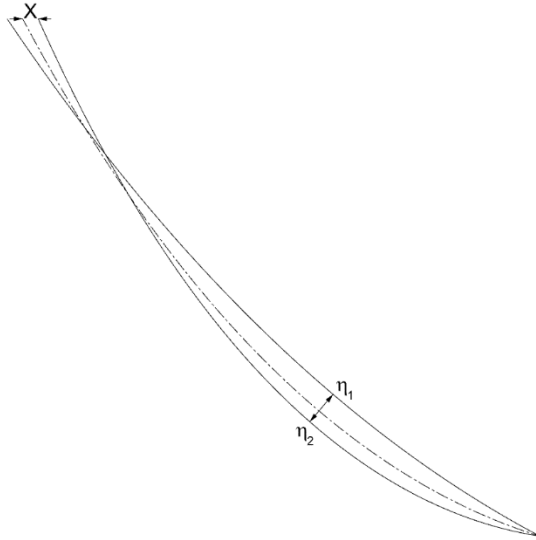
$$\dot{x} = X \omega \cos \omega t$$

⁶ $\int_0^T \cos^2 \omega t |\cos \omega t| dt = 4 \int_0^{T/4} \cos^3 \omega t dt = \frac{8}{3\omega}$

Analytic mooring line damping

$$4B_2X^3\omega^3 \int_0^{T/4} \cos^3 \omega t dt = 2\rho C_D D \omega^3 \int_0^L \eta^3 ds \int_0^{T/4} \cos^3 \omega t dt$$

The mooring line normal displacement η at maximum and minimum offset x is not necessarily symmetric about the zero-offset position. This is especially the case if the mooring line is semi-taut.



$$4B_2X^3\omega^3 \int_0^{T/4} \cos^3 \omega t dt = \frac{1}{2}\rho C_D D \omega^3 \left[2 \int_0^L \eta_1^3 + \eta_2^3 ds \int_0^{T/4} \cos^3 \omega t dt \right]$$

$$B_2 = \frac{1}{4X^3} \rho C_D D \int_0^L \eta_1^3 + \eta_2^3 ds$$

The complete quadratic damping coefficient for a single mooring line is a function of the top offset amplitude X , the mooring line normal displacement, and the drag force coefficient. In a mooring spread the contribution from each mooring line can be added together to achieve the total quadratic damping coefficient.

A linearized version of the damping coefficient can be found by assuming the dissipated energy at the top point to be

$$\Delta E = \int_0^T B_1 \dot{x} |\dot{x}| dt$$

$$B_1 = \frac{4\omega}{3\pi X^2} \rho C_D D \int_0^L \eta_1^3 + \eta_2^3 ds^7$$

The linearized coefficient is clearly also a function of the angular frequency.

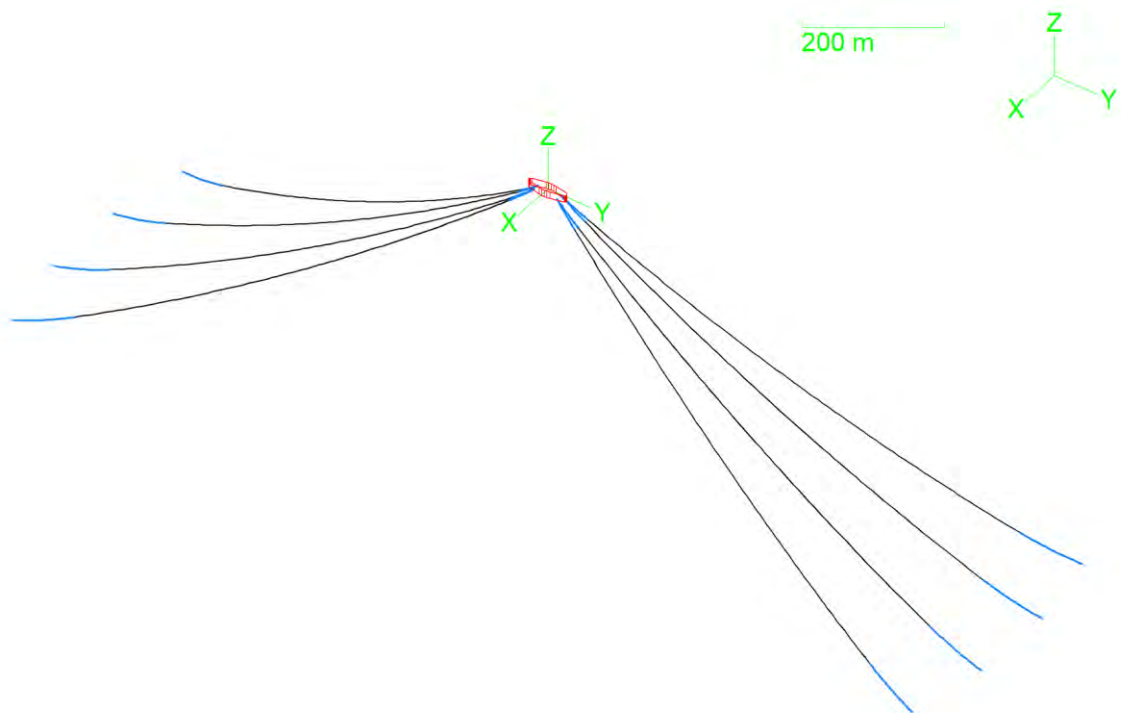
⁷ The linear damping coefficient is shown also in reference 4.

3 Implementation and benchmark

The theory above has been implemented in a computer code in which OrcaFlex is used to calculate the quasi-static mooring line configurations. The benchmark case consists of an idealized mooring line spread with 8 lines in 450 m water depth, with the following mooring line properties

Section	Length	Type
Bottom	100	147mm steel chain
Mid	750	124 mm steel wire rope
Top	50	147mm steel chain

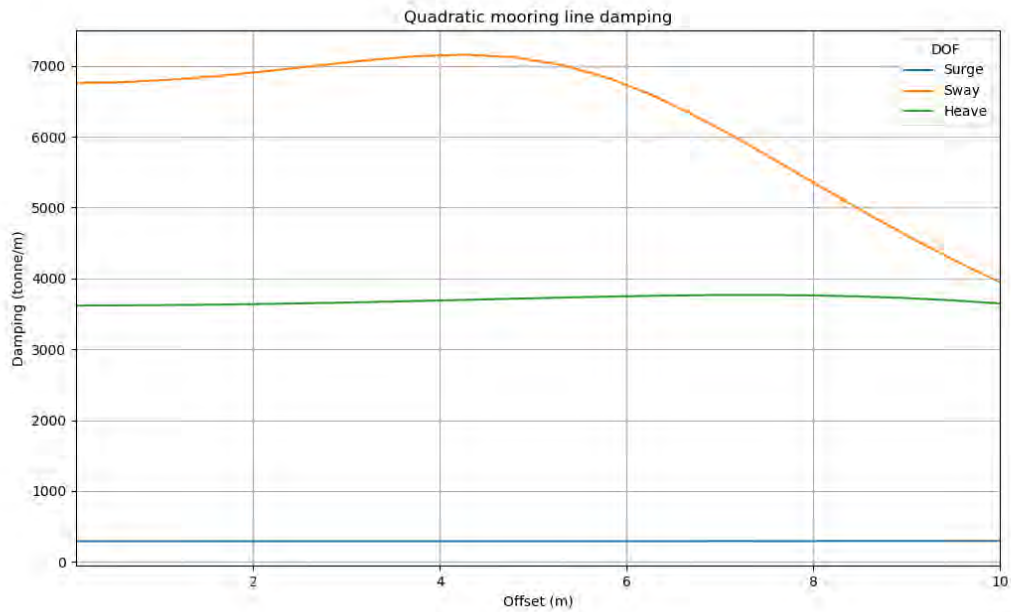
The pretension is 2160 kN in all mooring lines. In the quadratic damping model, the mooring system is replaced with a non-linear spring and a quadratic damping coefficient.



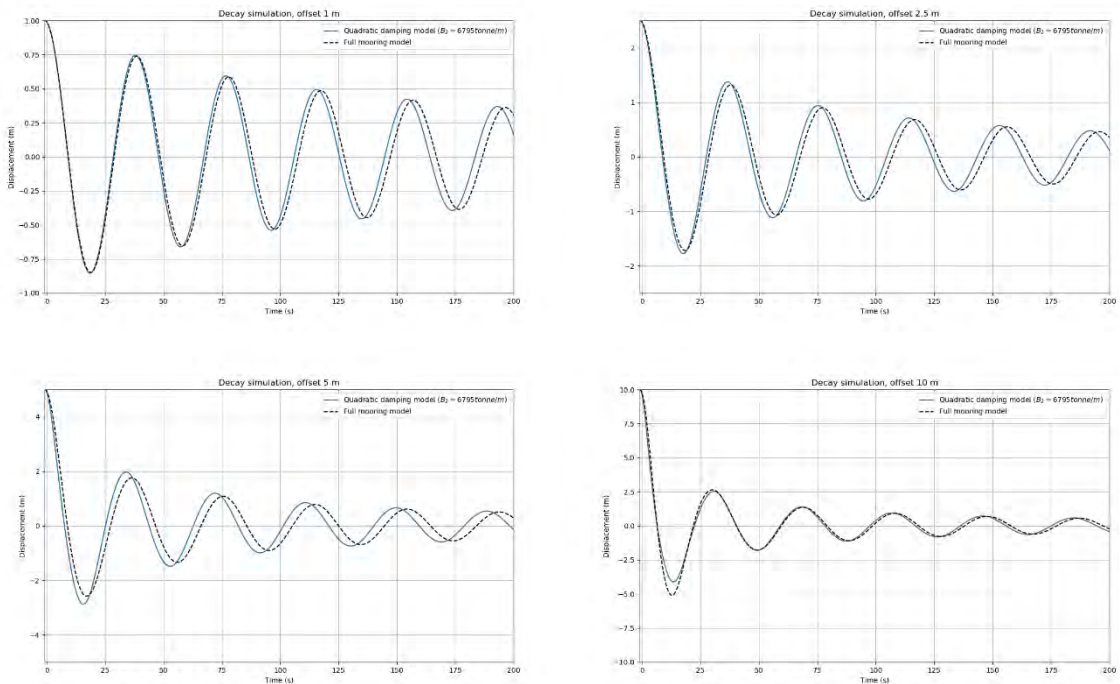
3.1 Damping vs. offset

The quadratic damping coefficients in surge, sway and heave has been calculated for various offsets. The analysis shows that the quadratic coefficient is approximately constant up to about 5 meters offset, after which a decrease is observed.

Analytic mooring line damping



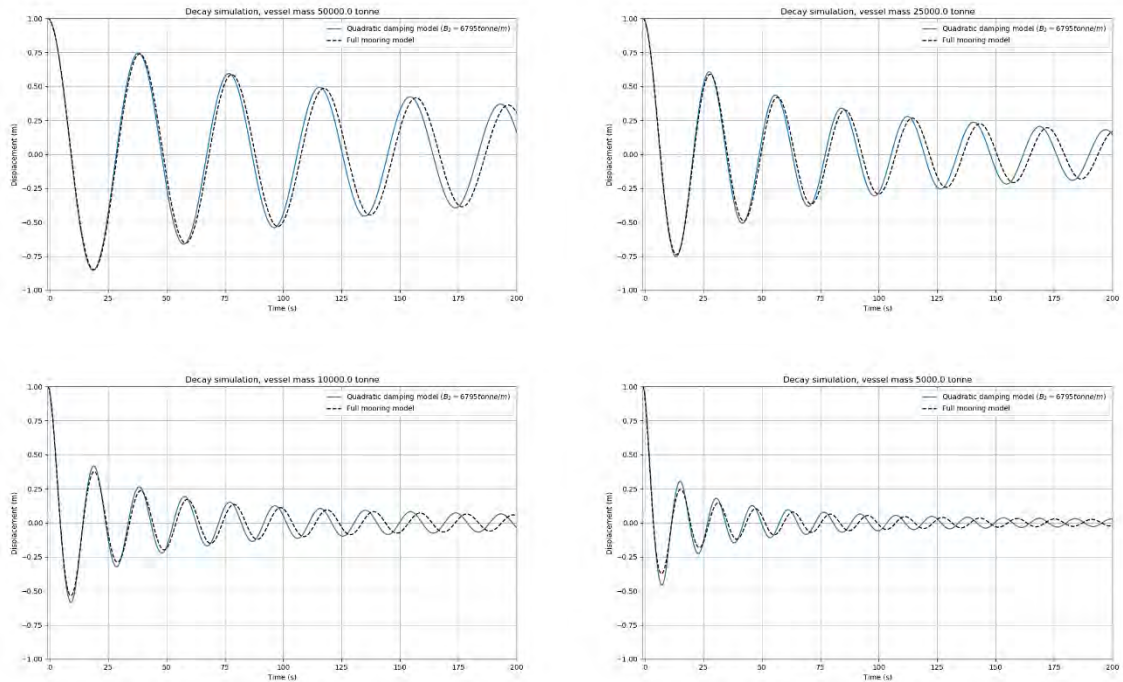
To evaluate the quadratic mooring line damping model decay simulations were run for the full mooring line configuration and the quadratic model and compared. The simulations show that the quadratic damping coefficient is a good approximation to the full mooring system for offsets up to 5 meters but too high at 10 meters, similar to the findings in the above figure.



3.2 Damping vs angular frequency

With the quasi-static assumption, the quadratic damping coefficient is independent on the oscillation frequency. To verify that the assumption holds, decay simulations has been performed for decreasing natural periods as shown in the following.

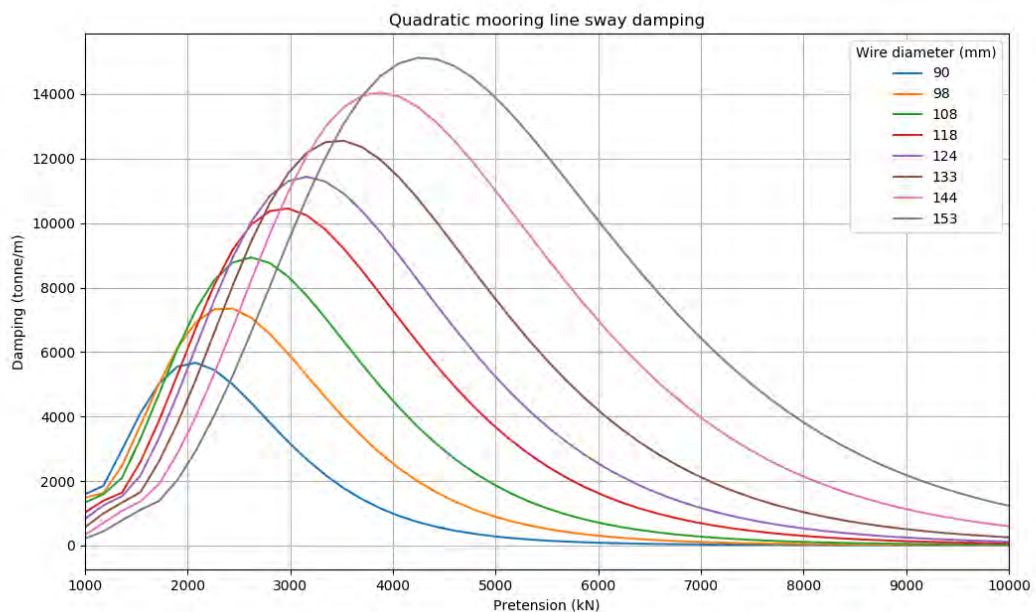
Analytic mooring line damping



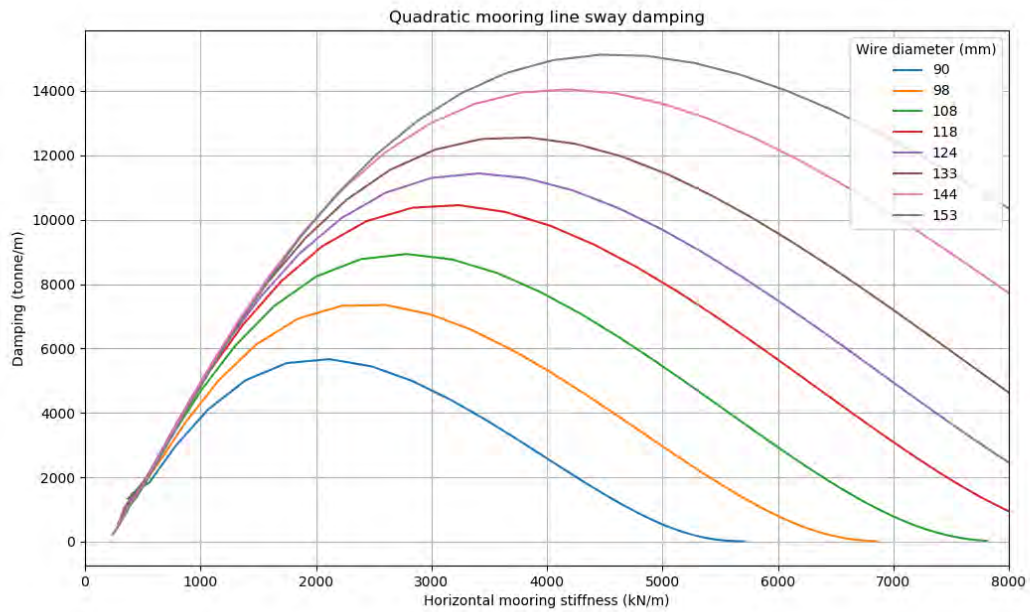
The quadratic damping tends to be underestimated for decreasing natural periods. This is probably due to increasing importance of local dynamic effects on the mooring lines that are only captured in the full mooring model, causing a higher mooring line normal displacement η in parts of the line and thus more damping.

3.3 Damping vs Pretension

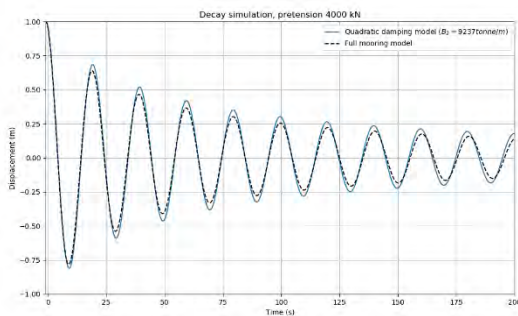
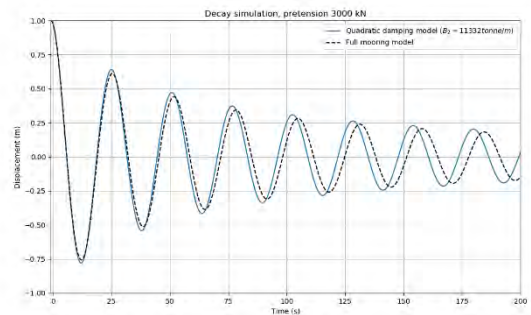
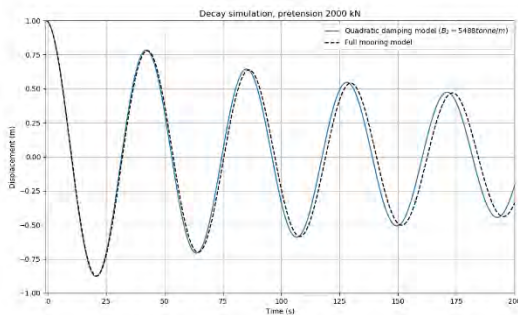
The damping coefficient as a function of pretension has been calculated for several different wire dimensions in the mid segment, shown in the two figures below for line pretension and mooring cluster stiffness respectively. The damping coefficient increases with pretension up to a maximum level. The damping coefficient decreases with further increased pretension.



Analytic mooring line damping



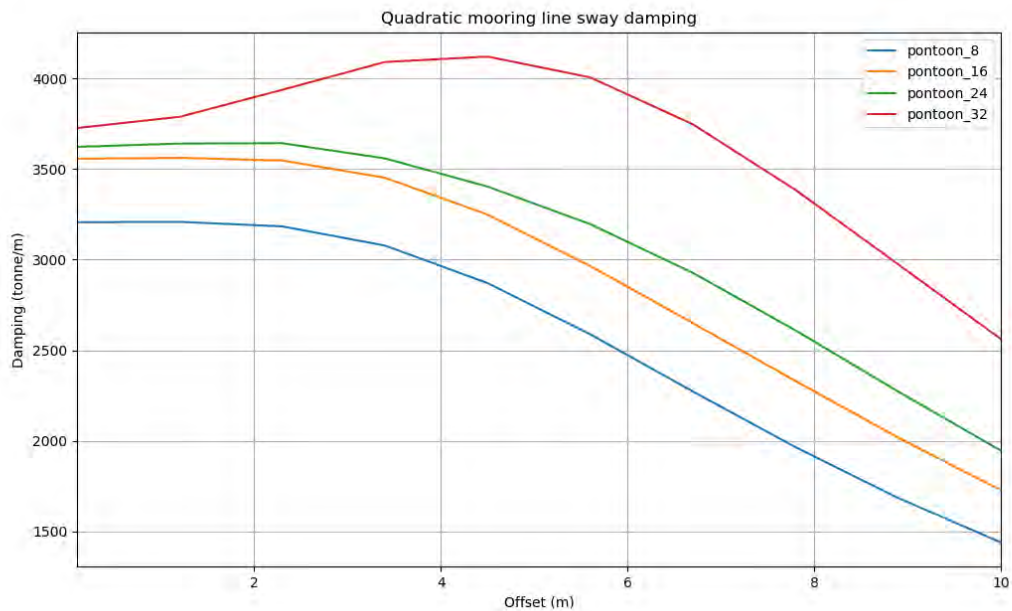
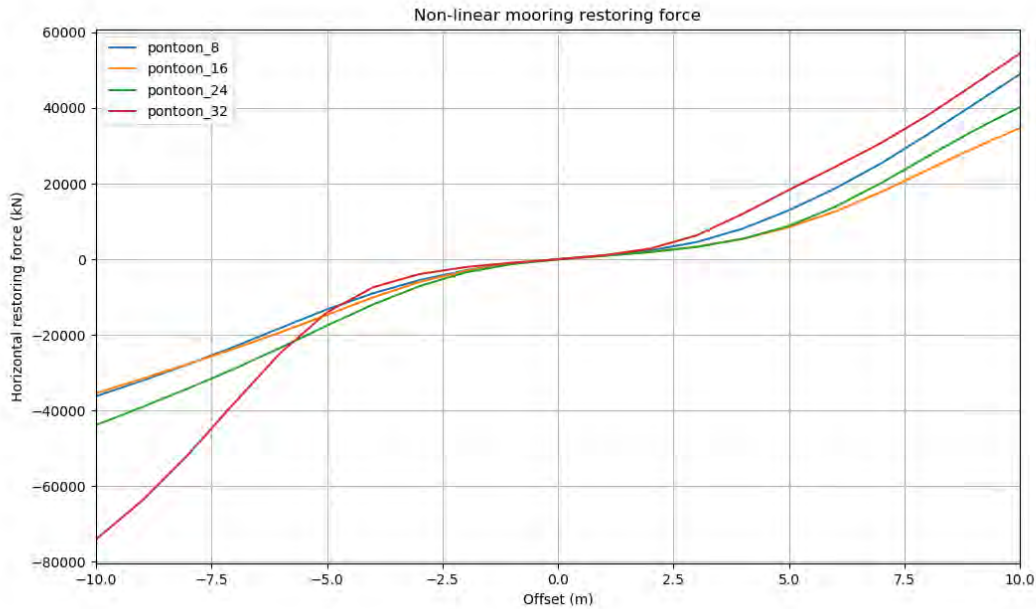
The only way pretension can affect the damping coefficient is through the quasi-static mooring line normal displacement. Decay simulations has been performed for the 124 mm wire with pretension 2000kN, 3000kN and 4000kN. According to the above figure, 3000kN should yield maximum damping coefficient.



As predicted, 3000kN pretension give higher damping coefficient than both 2000kN and 4000kN. However, as the pretension increases the natural period decreases and dynamic effects become more important. Therefore, the precision of the analytical model will decrease with increasing pretension.

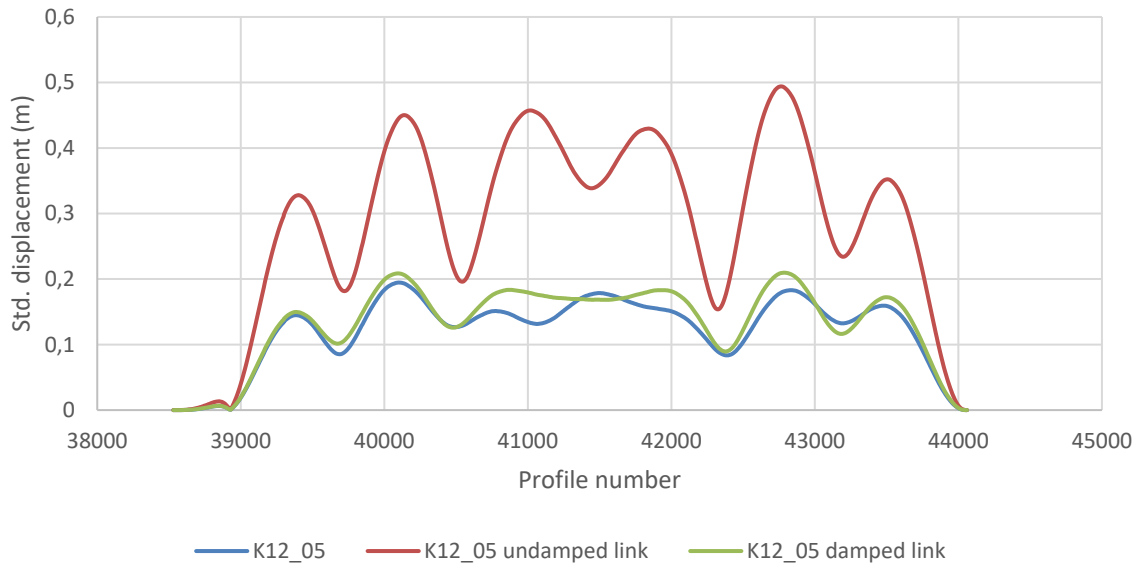
3.4 Full bridge model

The analytical mooring damping model has been implemented in the full bridge model by replacing the mooring line system with non-linear springs and quadratic damping. The non-linear mooring system restoring force and quadratic damping extracted from the full mooring model is shown below.

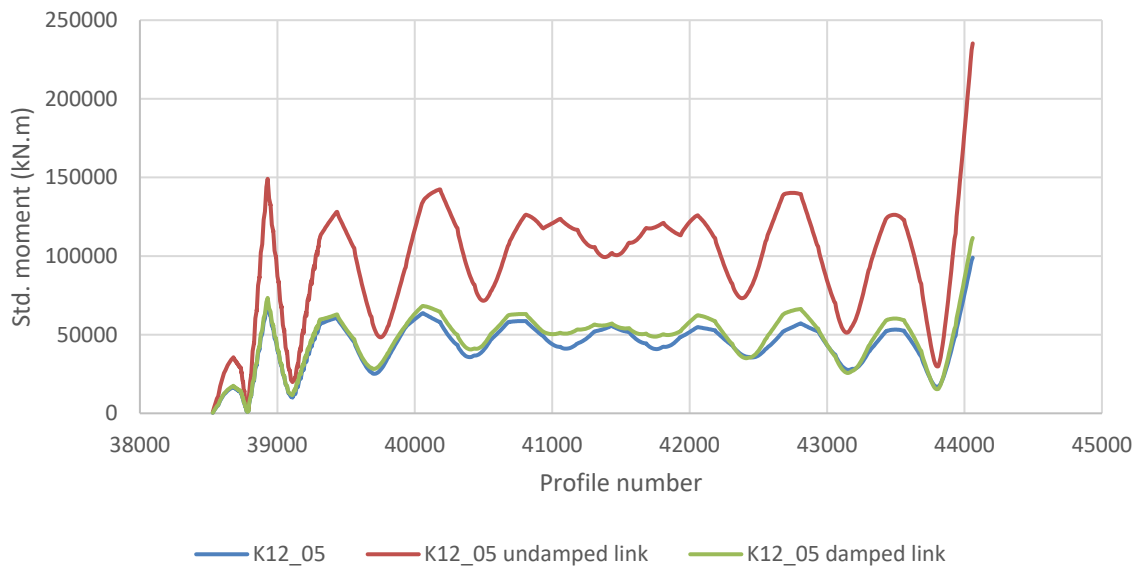


Frequency domain analysis with 0.34m significant wave height and 14s spectral peak period has been performed for the full model and the link model with and without quadratic damping. The damping level in the full mooring model and the link model is very similar. Assuming the maximum transverse displacement is about 4 times the standard deviation, the maximum displacement is about 0.8m. This is well within the constant region of the quadratic damping curves in the figure above, and the quadratic damping level can be assumed to be representative. The model should also be benchmarked for low frequency loads, for example with dynamic wind loads.

Transverse displacement



Vertical bending moment





4 Discussion

The proposed quadratic mooring line damping coefficient seems to be a reasonable representation of the mooring line damping as found in the full mooring model if the dynamic sway deflection of the pontoon is less than 2.5 m (K12 concept) relative to the initial configuration but may be nonconservative at higher deflections. For low periods the quadratic damping model is conservative.

Current will cause a static deflection of the pontoon, thereby using some of the margin of 5 m deflection. However, local current will increase the actual drag load on the mooring chain, and the net effect of current is therefor considered as giving an increased damping that will only be captured with the full mooring line model. Hence, the use of the quadratic drag model is conservative also when current loads are considered.

Concept development, floating bridge E39 Bjørnafjorden

Appendix F – Enclosure 3

**10205546-01-NOT-055
Software / Programvare**

**Programvare
Notat**

10205546 Konseptutvikling, flytebru E39 Bjørnafjordent
Kvalitetsledelsessystem

Dokument nr.: 10205546-01-NOT-055
Dato / revisjon: 14.02.2019 / 00
Side: Side 1 av 4

Utarbeidet av: Roar Granheim
Kontrollert av: Petter Sundquist
Godkjent av: Svein Erik Jakobsen

1 Formål og omfang

I kontraktens kapittel D1 er det beskrevet at:

«Rådgiver må disponere programvare som fullt ut er egnet til den bruken som oppdraget krever. Rådgivers erfaring med bruk av disse programmene skal dokumenteres.»

Formålet med dette dokumentet er å lage en oversikt over programvaren som benyttes i oppdraget og av hvem. Det skal også angis hovedversjon av programvaren til informasjon til eventuelt andre brukere av programvarens filer.

Kompetanse vedrørende bruk av programvaren er beskrevet i kontraktens CV'er.

2 Definisjoner og forkortelser

3 Beskrivelse

Type program	Funksjon / mål	Hovedversjon av Programvare	Utførende firma	
	Globalanalysene			
OrcaFlex	Globalanalyse av dynamikk (vind, bølge, etc.)	10.3	Entail Aas-Jakobsen	

Konseptutvikling, flytebru, E39 Bjørnafjorden

NOT – Programvare

RM Bridge	Globalanalyse av statisk oppførsel (egenvekt, trafikk, temperatur etc.), verifikasjon av miljølastene i form av dynamisk koblede vind-/bølge-analyser i tidsplanet	v.11	COWI Johs Holt Aas-Jakobsen	
NovaFrame	Globalanalyse av vind i frekvensplanet		Aas-Jakobsen	
Phyton	Anaconda-distribusjon, brukes til pre- og postprosessering samt analysestyring	3.6	Entail	
Tailor	Web-interface mot skyregning for Orcaflex og NovaFrame, samt postprosessering av RM-bridge	NA	Entail	
	Spesialstudier			
Wamit	Hydrodynamisk respons av pongtonger, interaksjonseffekter etc.	7.2	Entail, Multiconsult	
AQWA	Eventuelt alternativ til Wamit		COWI	
OrcaFlex	Dynamisk stabilitet, skipsstøt		Entail Aas-Jakobsen	
OrcaFlex	Global analyse skipsstøt	10.3	Multiconsult, Entail	
RM Bridge	Skråstagbru (utbygging), tester dynamisk stabilitet Parameterstudie på «rett» bru		COWI Johs Holt	
LS-DYNA	Skipsstøt (globale og lokale analyser)	9.1 SMP S	Entail, Moss Maritime	
Rhino	3D-modellering for analyse	6	Entail	
Sesam Genie	3D-modellering for lokal strukturanalyse	7.9.04	Entail	

Konseptutvikling, flytebru, E39 Bjørnafjorden

NOT – Programvare

			Aas-Jakobsen	
Sesam Sestra64	Lineær elementmetode	10.4	Entail Aas-Jakobsen	
Ansys	Lokale analyser		Multiconsult Aas-Jakobsen	
Plaxis 2D	Beregning av skråningsstabilitet (FE program)	2016	NGI	
HVMCAP 3.0	Beregning av udrenert holdekapasitet av suganker penetrert i leire (FE program)	2006	NGI	
ChainConfig 1.01b	Beregning av kjettingkonfigurasjon fra mudline til ankerets "padeye»	2006	NGI	
AnchorPen 2.01	Beregning av penetrasjonsmotstand av suganker penetrert i leire, sand eller lagdelt jord	2008	NGI	
Quiver	1D dynamisk skråningsstabilitet	2017	NGI	

4 Dokumentasjon og arkivering

5 Referanser

6 Maler / skjema

7 Endringer fra forrige utgave

Første utgave av dokumentet

8 Flytskjema

Ikke utarbeidet